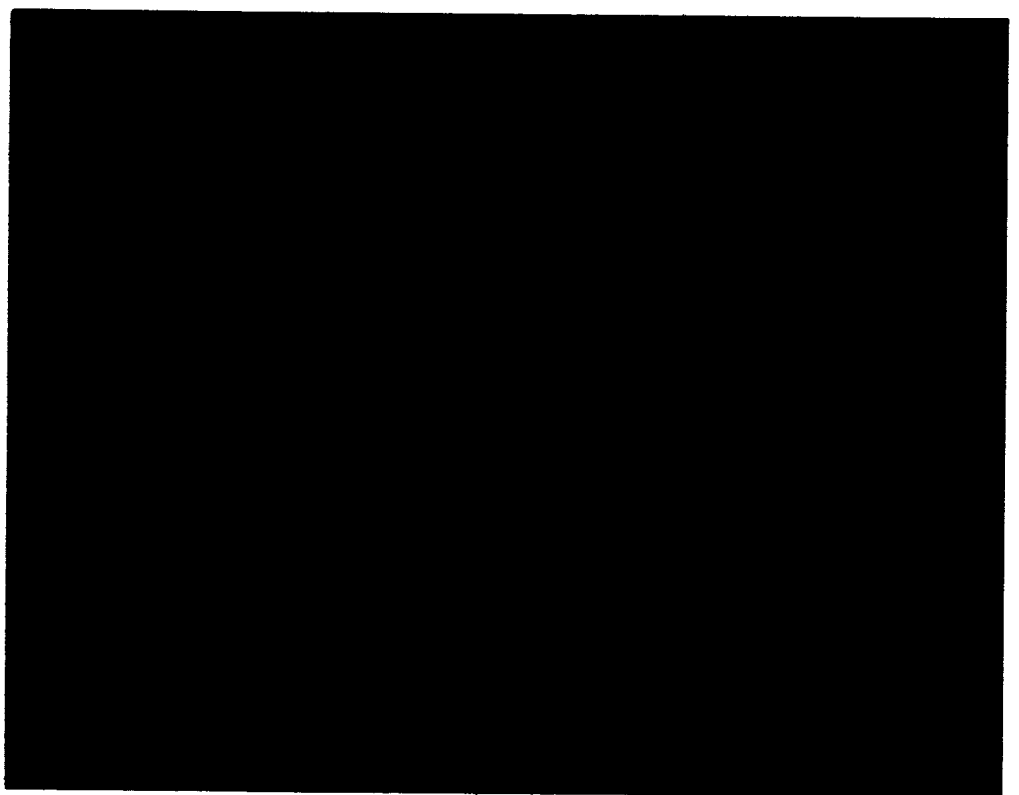


111 p.

*af*  
N 63 22586

CODE-1  
NASA CR 51567

JUNE 1963



HUGHES

HUGHES AIRCRAFT COMPANY  
SPACE SYSTEMS DIVISION

FINAL REPORT

OTS PRICE

XEROX \$ 9.60 ph  
MICROFILM \$ 3.53 mf.

SOLAR ELECTRIC PROPELLED SPACECRAFT,  
CAPABILITIES STUDY NASW-560

4185005

HUGHES

HUGHES AIRCRAFT COMPANY  
SPACE SYSTEMS DIVISION

Culver City, Calif.

(NASA contract NASW-560)

(NASA CR-51567) OTS: \$ 9.60 ph,  
\$ 3.53 mf

auth. JUNE 1963  
Emil. Ceps.

FINAL REPORT

11 p  
21 refs

## CONTENTS

	Page
1. INTRODUCTION	1-1
2. SUMMARY	2-1
3. SCOPE OF INVESTIGATION	
Launch Vehicle Considerations	3-1
Electric Engine Selections	3-1
Trajectory Considerations	3-3
4. SPACECRAFT PERFORMANCE	
Computer Program	4-1
Polar Orbit Transfer Performance	4-2
Equatorial Orbit Performance	4-6
5. SPACECRAFT SYSTEM DESIGN	
Solar-Electric Propulsion Systems	5-1
Mission Selection	5-25
Mission Payload	5-42
General Arrangements	5-45
6. REFERENCES	6-1
APPENDIX. EQUATIONS USED IN TRAJECTORY COMPUTATIONS	A-1

## 1. INTRODUCTION

The purpose of this study is to establish the payload capabilities of solar-electric propulsion systems (using currently programmed NASA launch vehicles) in performing earth satellite scientific missions. Particular emphasis is given to the determination of realistic power plant weights which required a detailed evaluation of power-conditioning requirements and careful assessment of solar cell efficiencies including the effects of degradation due to radiation, solar storm, micrometeorites, etc., as a function of required lifetime. A digital computer program was derived for the study and includes the perturbations due to the earth's oblateness, gravitational effects of sun and moon, atmospheric drag, and solar radiation pressure. This program was used to derive the parametric performance data for a family of solar-electric-propelled spacecraft. These performance capabilities were then compared with the requirements of the NASA planned earth satellite missions, and two systems (one utilizing an electrothermal engine and one an electrostatic engine) were selected for system design analysis. Conceptual designs of these spacecraft, each capable of performing the Polar Orbiting Geophysical Observatory (POGO) scientific mission, were derived and are presented here.

## 2. SUMMARY

22586 *mr*

This report presents preliminary system designs of two solar-electric-propelled spacecraft, one utilizing an electrostatic engine (ion), Figure 2-1, and the other utilizing an electrothermal engine (resisto-jet), Figure 2-2, both of which are capable of accomplishing the Polar Orbiting Geophysical Observatory (POGO) scientific mission. Maximum payload and maximum altitude capabilities of both systems actually exceed the POGO requirements.

The systems presented used the Thor-Agena B launch vehicle, utilize solar cells for primary power, and have three-axis cold gas attitude control systems for the spacecraft proper and independent power gimbal drive attitude control systems for the scientific packages. An on-board high-density magnetic tape storage system is provided with a data storage capacity in excess of 11,000,000 bits.

The parametric performance of a family of spacecraft of both types is depicted in Figure 5-24 in Section 5. The figure shows that for equal power levels, the electrothermal engine spacecraft is superior to the electrostatic engine spacecraft from both an orbit transfer time and maximum altitude standpoint. Because of the long orbit transfer times required for the electrostatic engine spacecraft, and because of the spatial dynamics of the orbit plane, the satellite passes through the earth's shadow before it can reach an altitude sufficient to remain clear of the shadow. As a result, the ion engine systems shown (Configurations III and IV, Figures 5-24a and 5-24b) are altitude limited.

It is apparent from the illustrated solar-electric-propelled spacecraft performance that all of the electric engine spacecraft types investigated are capable of performing any of the scientific earth satellite missions up through the POGO class. However, the scientific mission capability attainable, pertaining to altitude and payload, is significantly affected by choice of engine type. The general arrangement is also greatly affected by engine type (see Figures 2-1 and 2-2) which in turn has

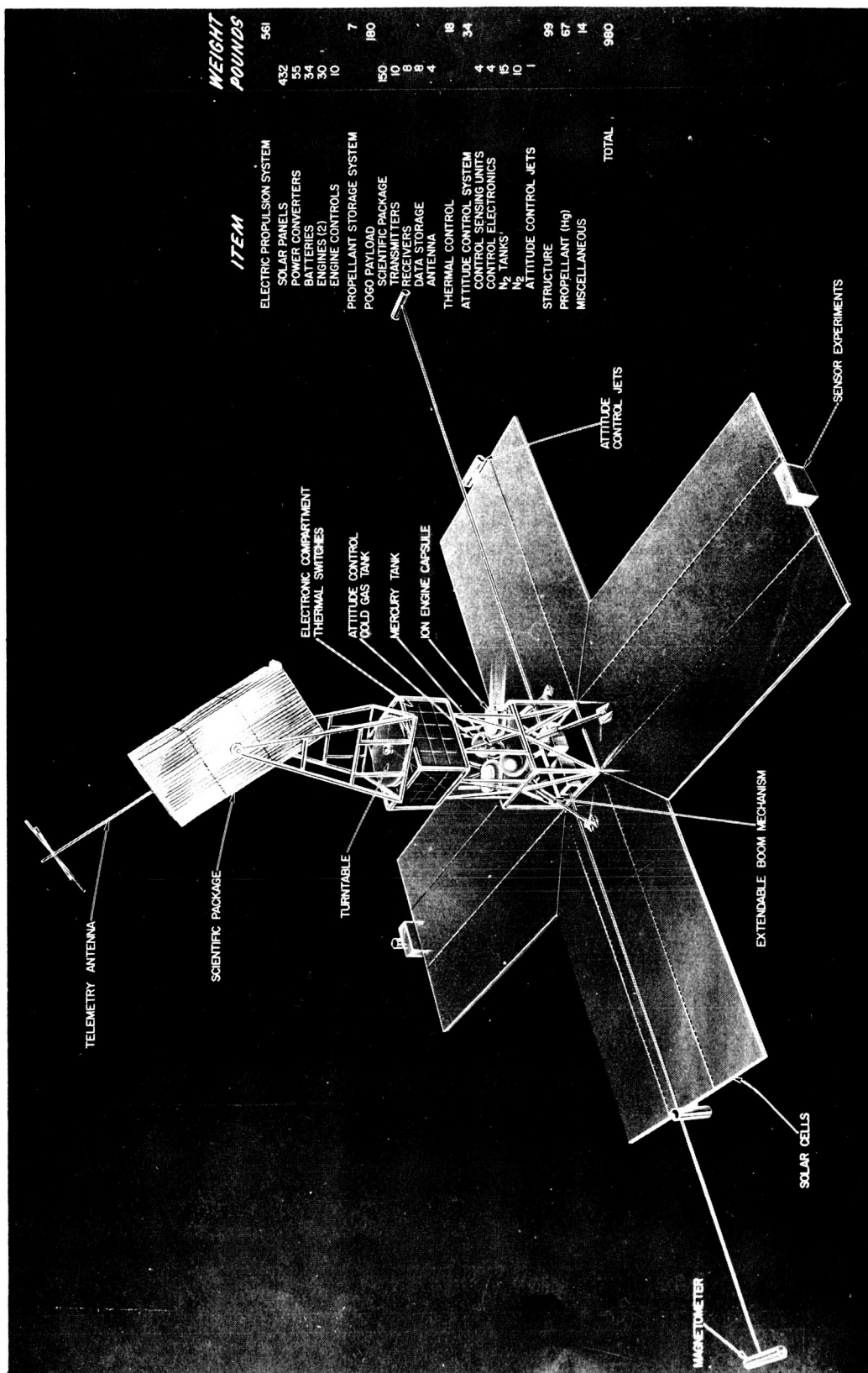


Figure 2-1. Ion Engine Spacecraft Perspective View

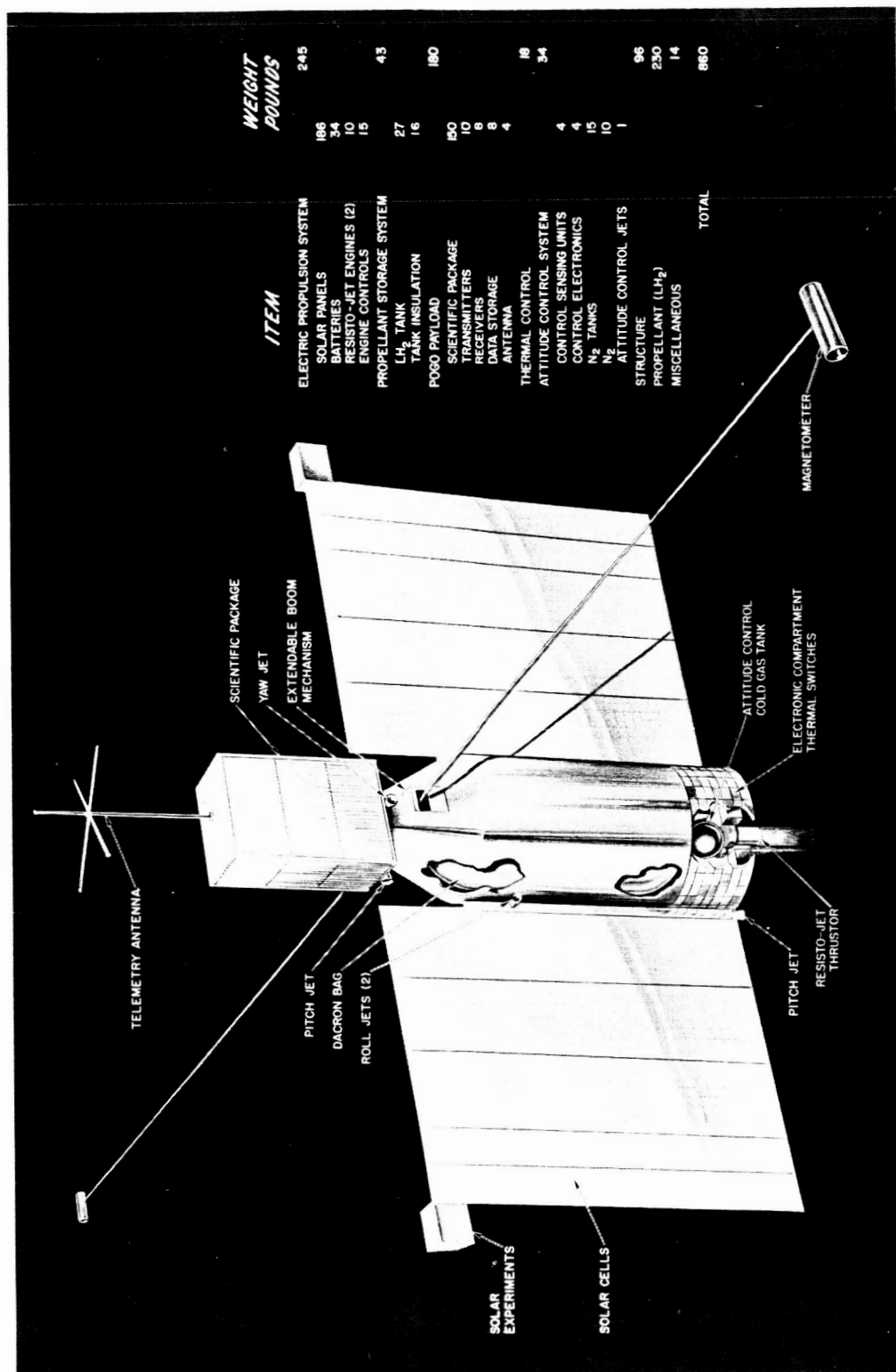


Figure 2-2. Single-Tank Resisto-Jet Engine Spacecraft Perspective View

22586

a predominant effect on solar panel deployment method and payload orientation control. It appears, therefore, that a system design analysis is required to determine the proper engine type for optimum scientific mission capability.

AUTHOR



### 3. SCOPE OF INVESTIGATION

This analysis covers the performance capabilities of solar-electric-propelled earth satellites that would be operational in the post-1964 period. Parametric performance data are derived for a family of spacecraft, specific designs evolved for one electrothermal type and one electrostatic type, and their capabilities in performing earth satellite scientific missions investigated.

#### LAUNCH VEHICLE CONSIDERATIONS

Since the spacecraft under consideration is power limited by the volume of solar panel that can be effectively contained within the particular nose shroud, the analysis has been restricted to systems using only the Thor-Agena B and Atlas-Agena B launch vehicles. A previous Hughes study indicated that the Thor-Delta would be limited to a maximum of about 600 to 700 watts, which is impractical for reasonable orbit transfer times. The Agena nose shroud, however, can conveniently house enough solar panel volume to produce up to 4000 watts of power.

#### ELECTRIC ENGINE SELECTIONS

Discussions were held with personnel from the Lewis Research Center, Hughes Research Laboratories, and Plasmadyne Corporation to establish the projected capabilities of the electron bombardment ion engines, the cesium contact ion engines, and the arc-jet engines, respectively. Also, since recent laboratory experiments by both the Lewis Research Center and Plasmadyne have indicated much higher potential efficiencies for resisto-jet engines than are projected for arc-jet engines, the present analysis was expanded to include resisto-jet engine systems. The power-to-thrust ratios predicted for these engine systems for the post-1964 era (and those used in developing the spacecraft performance data) are presented in Figure 3-1.

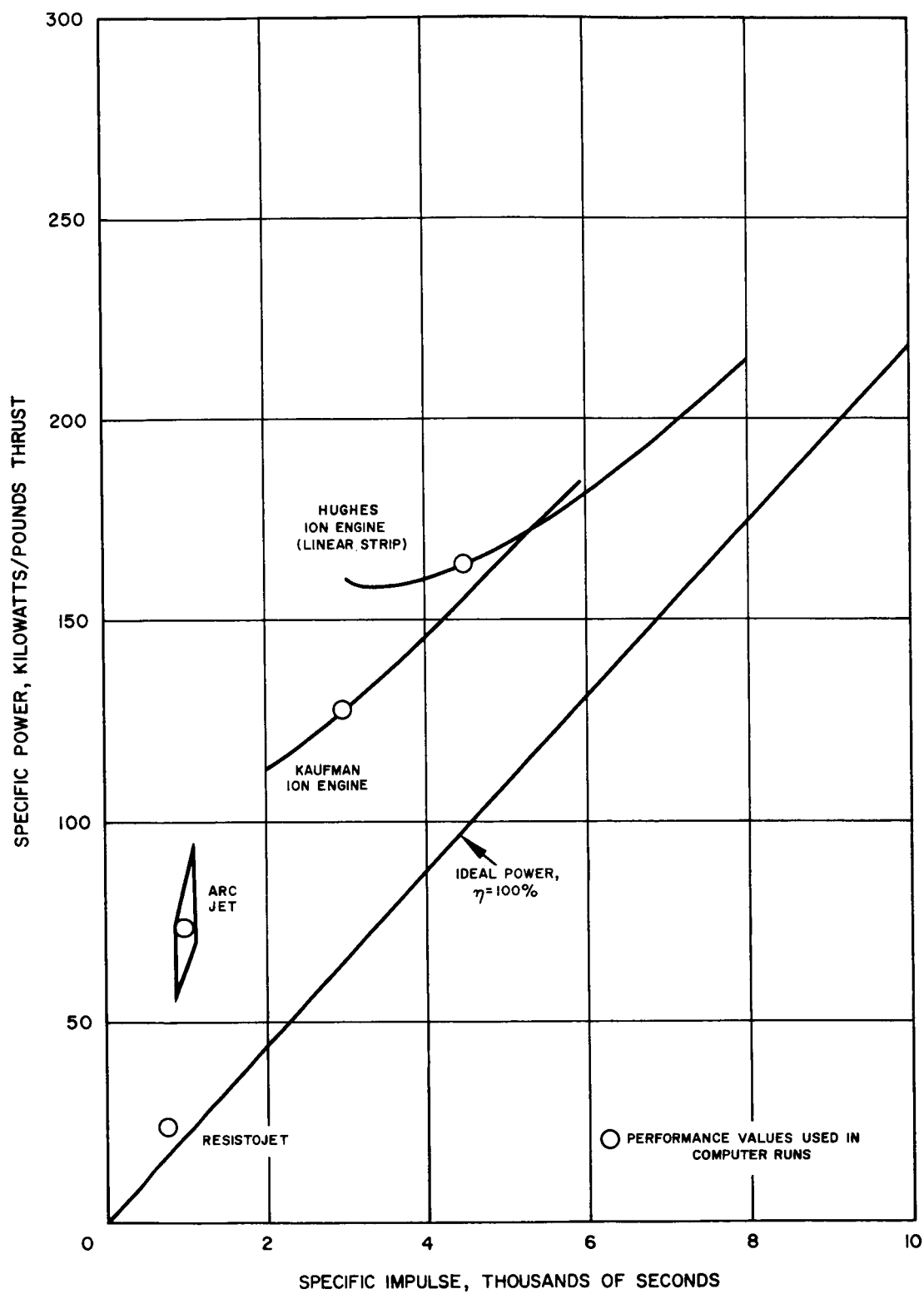


Figure 3-1. Power-to-Thrust Ratio Variation with Specific Impulse

## TRAJECTORY CONSIDERATIONS

Both near-polar orbit and near-equatorial orbit transfer missions are considered in this study. The polar orbit trajectories assume constant continuous thrust, while the equatorial orbit trajectories assume constant thrust parallel to the sunline while in view of the sun whenever the angle between thrust and vehicle velocity vectors is within a fixed range, and coast while in the earth's shadow.

The digital computer program derived for this study includes the perturbations due to the earth's oblateness, gravitational effects of sun and moon, atmospheric drag, and solar radiation pressure. Details of the computer program are given in Section 4.

Since the types of spacecraft to be analyzed in the study are power limited, the performance criterion used is the maximum payload for a given trip time within the power levels available. The optimum specific impulse for any trip time is the one that yields the greatest payload. To accomplish the optimization for a given mission, hand calculations were made of the variation of payload weight with specific impulse for specified values of trip time. In this manner, the optimum specific impulse for each electric-engine system was determined, and all computer runs were made at that specific impulse (see Figure 3-1).

#### 4. SPACECRAFT PERFORMANCE

##### COMPUTER PROGRAM

The equation of motion for a vehicle moving in the vicinity of the earth may be written:

$$\frac{d\bar{P}}{d\psi} = \bar{f}(\bar{P}, \psi) \quad (4-1)$$

where  $\bar{P}$  is the orbital elements vector and  $\psi_1$  the argument of latitude. The forcing function  $\bar{f}$  is of the order of the acceleration in excess of the inverse square central force field. Since  $\bar{P}$  changes very slowly, the increment over one revolution

$$\Delta P_n = \bar{P}_{n+1} - \bar{P}_n = \int_0^{2\pi} \bar{f}(\bar{P}_1, \psi) d\psi \quad (4-2)$$

is very nearly alike for neighboring revolutions. This suggests the possibility of calculating  $\bar{P}$  for widely spaced revolutions by an extrapolation process. More precisely, a solution,  $P_n$ , to the difference equation (Equation 4-2) is sought, for  $n = N, 2N, 3N, \dots, N \gg 1$ . An algorithm for solving such systems of differential-difference equations has been developed by Taratynova\* to determine the long-term effects of natural perturbations on near earth satellites. This technique, which consists alternately of solving Equation 4-1 for one revolution and Equation 4-2 for  $N$  revolutions, is applied here to the integration of microthrust orbits.

---

\*"Numerical Solution of Equations of Finite Differences and Their Application to the Calculation of Artificial Earth Satellites,"  
ARS Journal, July 1961.

Three programs have been developed for the investigation of various low-thrust missions. Program I is general in nature; it includes all the pertinent perturbations and, moreover, can accommodate a variety of steering functions. Programs II and III are written for specific steering functions and are aimed at computation speed. Program II runs at least ten times faster than Program I. Details of the three programs are discussed in the following paragraphs and summarized in Table 4-1.

#### Program I

Equation 4-1 is integrated numerically by use of the Runge Kutta method. The  $J$ ,  $J_3$ ,  $D$  terms of the earth's potential gravitational attraction of sun and moon, drag, and solar radiation pressure are included in the perturbations. The thrust acceleration vector is directed along  $\bar{r}_{EP} \times \bar{r}_{SP}$  ( $\bar{r}_{EP}$  = earth-satellite vector,  $\bar{r}_{SP}$  = sun-satellite vector), but this may be replaced by other steering functions. The orbit parameters chosen are free from singularity at zero eccentricity.

#### Program II

Thrust acceleration is directed along  $\bar{r}_{EP} \times \bar{r}_{SP}$ . Equation 4-1 is integrated analytically, holding  $\bar{P}$  constant in  $\bar{f}(\bar{P}, \psi)$ . Eccentricity is assumed to be zero. Drag and oblateness effects of the first order are included. The program has a shadow test, which terminates the run whenever any part of the trajectory falls within the earth's shadow.

#### Program III

Thrust acceleration is directed along  $\bar{r}_{PS}$  or  $-\bar{r}_{PS}$ , whichever points in the direction of motion. Thrusting is limited to portions of the trajectory in which the angle between velocity vector and thrust acceleration vector is less than a preset value. No thrusting occurs while the vehicle is in the shadow of the earth. Equation 4-1 is integrated analytically. First-order oblateness perturbations are included. The option to remove orbit eccentricity at various ranges of the semimajor axis is also provided.

### POLAR ORBIT TRANSFER PERFORMANCE

A number of low-thrust trajectories were computed in which vehicle thrust is applied normal to both the sunline and local vertical and where the earth's shadow is avoided. These thrust limitations correspond to the use of continuous thrust with a fixed vehicle geometry where the solar panel plane is kept normal to the sunline. Figures 4-1a through 4-1d show the payload and time involved in orbit transfer missions using the Thor-Agena B launch vehicle. Spacecraft injection, at 1000 pounds gross weight, into

TABLE 4-1. COMPUTER PROGRAMS

Steering Functions

- A. Thrust vector in orbit plane normal to radius vector
- B. Thrust vector normal to both sun and earth radius vectors
- C. Thrust vector parallel to sunline

Mechanization

I. General Program (running time, 6 minutes)

- 1) Accommodates variety of steering functions
- 2) Utilizes numerical integration and extrapolation
- 3) Includes perturbation of drag, solar radiation, second-order earth oblateness, first-order sun and moon gravity

\*II. Polar Orbit Program (running time, 30 seconds)

- 1) Assumes circular orbit – steering A or B
- 2) Utilizes analytical integration and extrapolation
- 3) Includes perturbations of drag and earth oblateness
- 4) Uses shadow test to terminate mission

\*III. Equatorial Orbit Program (running time, 15 minutes)

- 1) Assumes elliptical orbit – steering C
- 2) Utilizes analytical integration of each orbit
- 3) Uses shadow test to determine thrust limits
- 4) Includes perturbations of earth oblateness
- 5) Includes option to remove orbit eccentricity

\*Programs II and III are entirely adequate for preliminary design purposes. Propellant consumption and mission times agree to four places or better with results of Program I.

a 300-n.mi. parking orbit is assumed. A 10-percent weight allowance was made for structure and 100 pounds allowed for the attitude control system, batteries, transmitters, receivers, antenna, and data storage equipment. Payload is defined as that weight remaining after solar panel, power conversion, engine and controls, propellant, and tankage weights are also deducted from the injection weight. Solar panel weights were calculated based on radiation damage data given in the section describing spacecraft system design. Thruster, power conversion, and communication system weights are described elsewhere in this report.

Figure 4-1e shows the relative performance of the four types of electric thrusters considered. The resisto-jet thruster appears to be best suited for this type of mission.

The effect on payload capability of change in parking orbit altitude is depicted in Figure 4-1f. For this comparison the orbit capability of the Thor-Agena B launch vehicle was assumed to be 925 pounds in a 500-n.mi. orbit and 600 pounds in a 1000-n.mi. orbit. A specific power plant weight including power conversion equipment of 200 lb/kw was assumed. Except for the shortest mission times, little payload capability is gained from an increase in initial orbital altitude. However, higher altitudes may be advantageous from a launch window standpoint, and such a tradeoff should be examined for specific cases.

Except for Figure 4-1f, the payload capabilities depicted assumed solar panel weights derived from solar cell degradation calculations as described in the section entitled spacecraft system design. If future data show a reduction in the intensity of the radiation belts surrounding the earth or a decrease in solar cell radiation damage, substantial payload increases can be expected. Figure 4-1g shows the effects of power plant specific weight (solar panel plus power conversion equipment) on payload capability for an ion-engine-powered vehicle. Figures 4-2a through 4-2c show the polar orbit transfer performance for missions using the Atlas-Agena B launch vehicle. Ion, arc-jet, and resisto-jet thrusters are considered and payload is as defined previously. Solar panel weights were calculated from data as presented in the section describing spacecraft system design. The resisto-jet is shown to be best suited to this mission.

Figure 4-3 shows the reduction in mission time that can be achieved by thrusting in the orbit plane rather than normal to the sunline. This small reduction in mission time does not seem to warrant the complexity associated with the independent thrust vector and solar panel alignment required to achieve it. In missions with fixed vehicle geometry, the thrust vector swings sinusoidally above and below the orbit plane during each orbit up to a maximum out-of-plane angle equal to the angle between the orbit vector and sunline. Figures 4-4a through 4-4i show the variation in this maximum out-of-plane angle with orbit altitude for missions using the Lewis ion engine and Thor-Agena B launch vehicle. Mission launch times of 5, 6, and 7 a.m. on 21 December of any year are shown at 2-, 3-, and 4-kw ion engine power levels. Each mission is shown for a number of initial orbit inclinations and each run is terminated when the vehicle enters the earth's shadow.

Figure 4-5 shows the maximum altitude achieved under the above limitation, as a function of initial orbit inclination and engine thrust level. The maximum altitude attained is clearly a function of the thrust level used. Only the highest thrust level (corresponding to a 4-kilowatt Lewis ion engine) achieved the 24-hour altitude. The lowest thrust level (corresponding to a 2-kilowatt Lewis ion engine) allows orbit transfer to something over 1.5 earth radii altitude.

Figures 4-6i through 4-6j show the effects of parking orbit inclination on the time to 1, 2, and 4 earth radii altitude for thrust levels corresponding to the ion, arc-jet, and resisto-jet engines considered and for launch on 21 December. The effect of thrust level on launch window and altitude attainable can be obtained by a comparison of these figures at the various thrust levels used. Ion engine power levels of 2, 3, and 4 kilowatts and electrothermal engine power levels of 1, 2, and 3 kilowatts were used. The use of low power level ion engine (2 kilowatt) seems marginal for orbit transfer to even 1 earth radius altitude. The lowest power level resisto-jet (1 kilowatt) has adequate thrust for orbit transfer to 4 earth radii altitude. These figures demonstrate the effect of minimal thrust levels on launch window and attainable vehicle altitude for missions originating from 300 n. mi. parking orbits.

The use of a somewhat higher parking orbit, possibly 500 n. mi., may alleviate this problem and should be examined if thrust levels below 15 millipounds are to be used.

Figure 4-7 shows the variation of launch window with launch date for missions to 1 earth radius altitude for a 2-kilowatt Lewis ion engine (15.4 millipounds). The launch window as shown allows a 6-month interval for morning launches and repeats exactly in the following 6-month period for evening launches. This figure shows a marked reduction in usable parking orbit inclination in late February through early March and in late August through early September.

Figure 4-8 shows the variations in time to 1 earth radius altitude as a function of launch date. Thrust level corresponded to the use of a 2-kilowatt Lewis ion engine and optimum parking orbit inclination was used at each date and launch time. Mission time is shown to vary about 15 days (10 percent) in two consecutive 6-month intervals. For minimum mission time, launch should be made from late September through late December and again from late March through late June.



## EQUATORIAL ORBIT PERFORMANCE

### Near-Equatorial Orbit Transfer

A number of trajectory calculations were made to determine the payload capability and transfer time to 24-hour orbit of a resisto-jet-propelled solar electric spacecraft. An initial orbit altitude of 1000 n. mi. and vehicle weight of 4100 pounds was the assumed capability of the Atlas-Agena B with an OAO nose shroud (10-foot diameter). Thrust is applied parallel to the sunline when thrust vector and vehicle velocity vector are aligned to within a preset value, and the vehicle is in view of the sun. No thrust is applied when the vehicle is in the earth's shadow. The payload capability of such a vehicle as a function of mission time for launch on 21 January of any year is shown in Figure 4-9.

An allowance of 400 pounds is given for vehicle structure and 100 pounds for the attitude control system, batteries, transmitters, receivers, antenna, and data storage equipment. The remaining weight of 3600 pounds is allocated to payload, solar panels, electric thrusters and controls, propellant and tankage. Solar panel weight was calculated from data in the section describing spacecraft system design, assuming that equatorial orbit radiation dose is three times that which would be received in polar orbit between the altitude of 1000 n. mi. and the 24-hour orbit at the same thrust-to-weight ratio. Tankage was assumed to be 20 percent of the propellant weight and 25 pounds were allowed for thruster and controls.

Figure 4-10 shows the effect of initial orbit node (launch time) on time to altitude for 3-kw resisto-jet-propelled vehicles launched on 21 January, 21 March, and 21 May. Launch can take place at any time of day, but significant reduction in mission time is achieved by launching with the orbit node approximately 180 degrees from vernal equinox. This is true for any launch date.

Figure 4-11 shows the effect of launch data on mission time and propellant consumption for a 3-kw resisto-jet-propelled vehicle launched with optimum orbit node. Yearly variation in mission time is about 10 days (5 percent) and propellant consumption about 18 pounds (1 percent). The capability of this type of vehicle is not significantly affected by launch date.

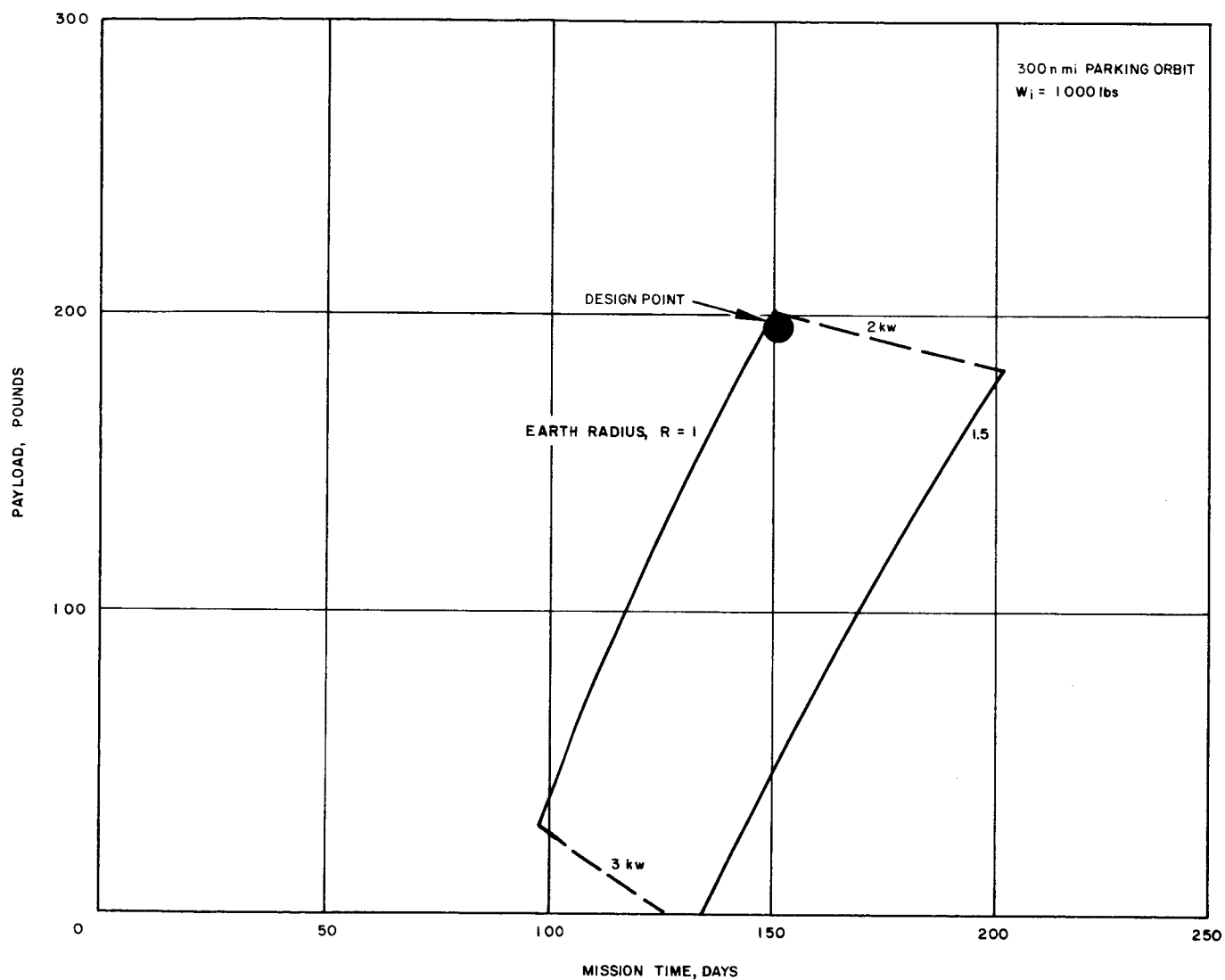


Figure 4-1. Polar Orbit Transfer Performance for Missions Utilizing  
 Thor-Agena B Launch Vehicle  
 a) Lewis Ion Engine Spacecraft

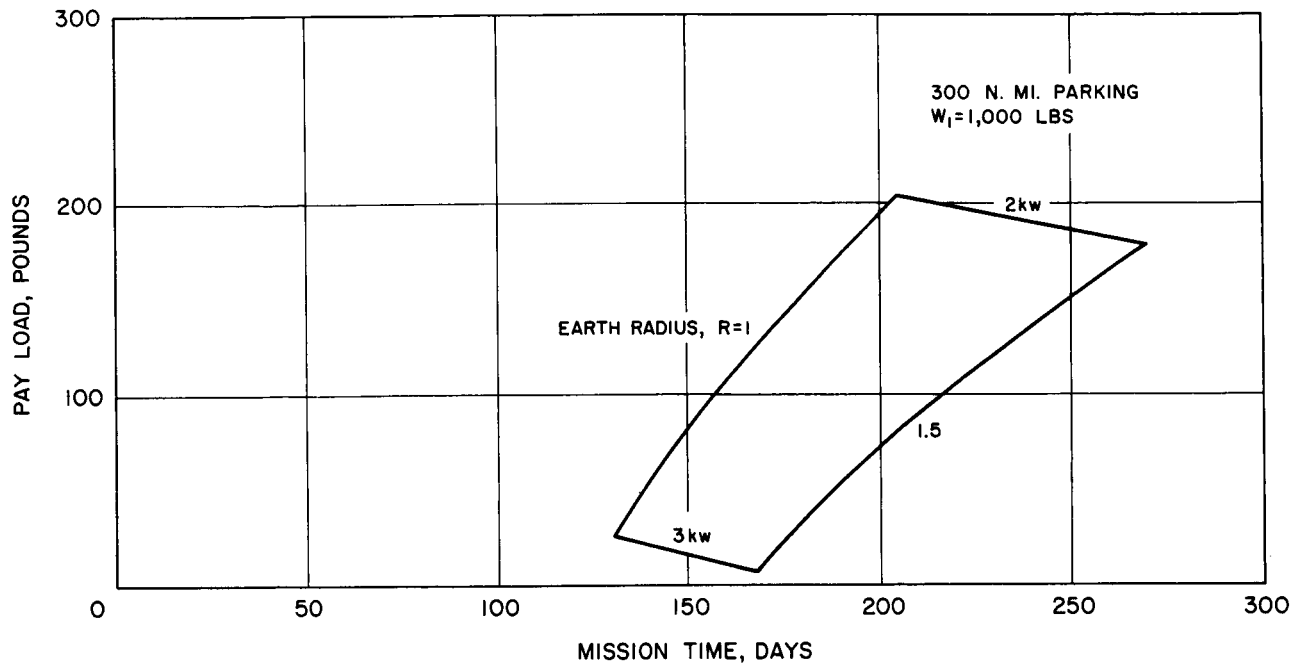


Figure 4-1 (continued).  
b) Hughes Ion Engine Spacecraft

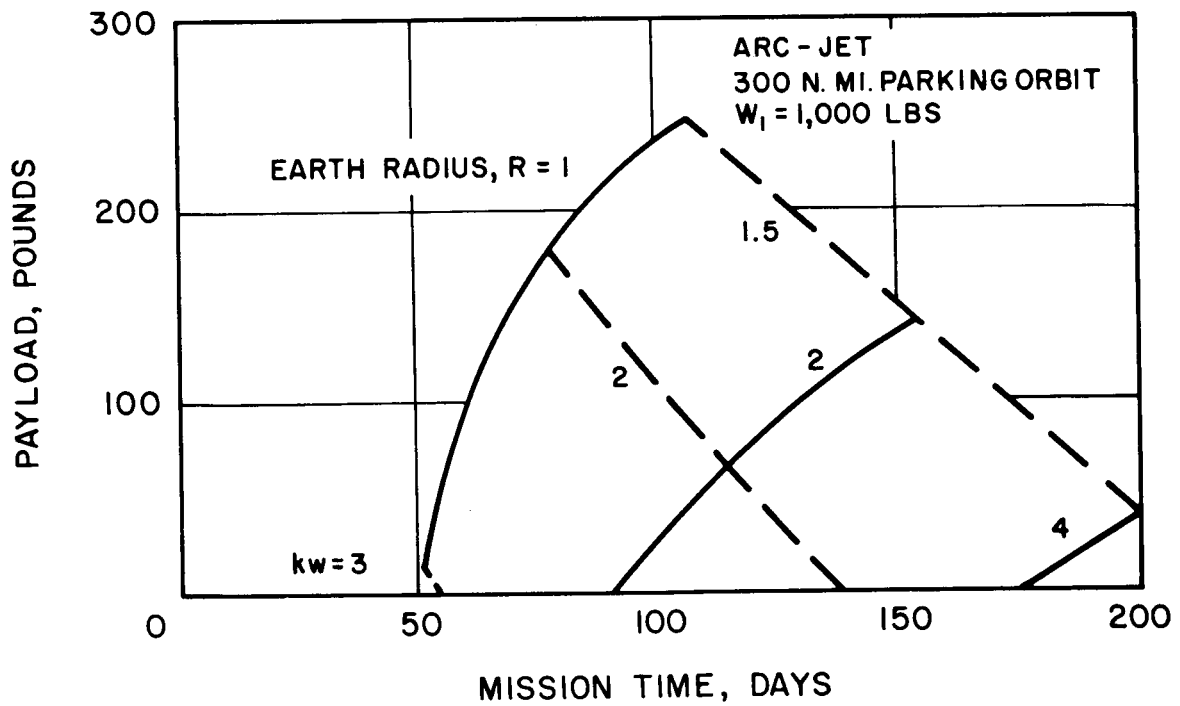


Figure 4-1 (continued).  
c) Plasmadyne Arc-Jet Engine Spacecraft

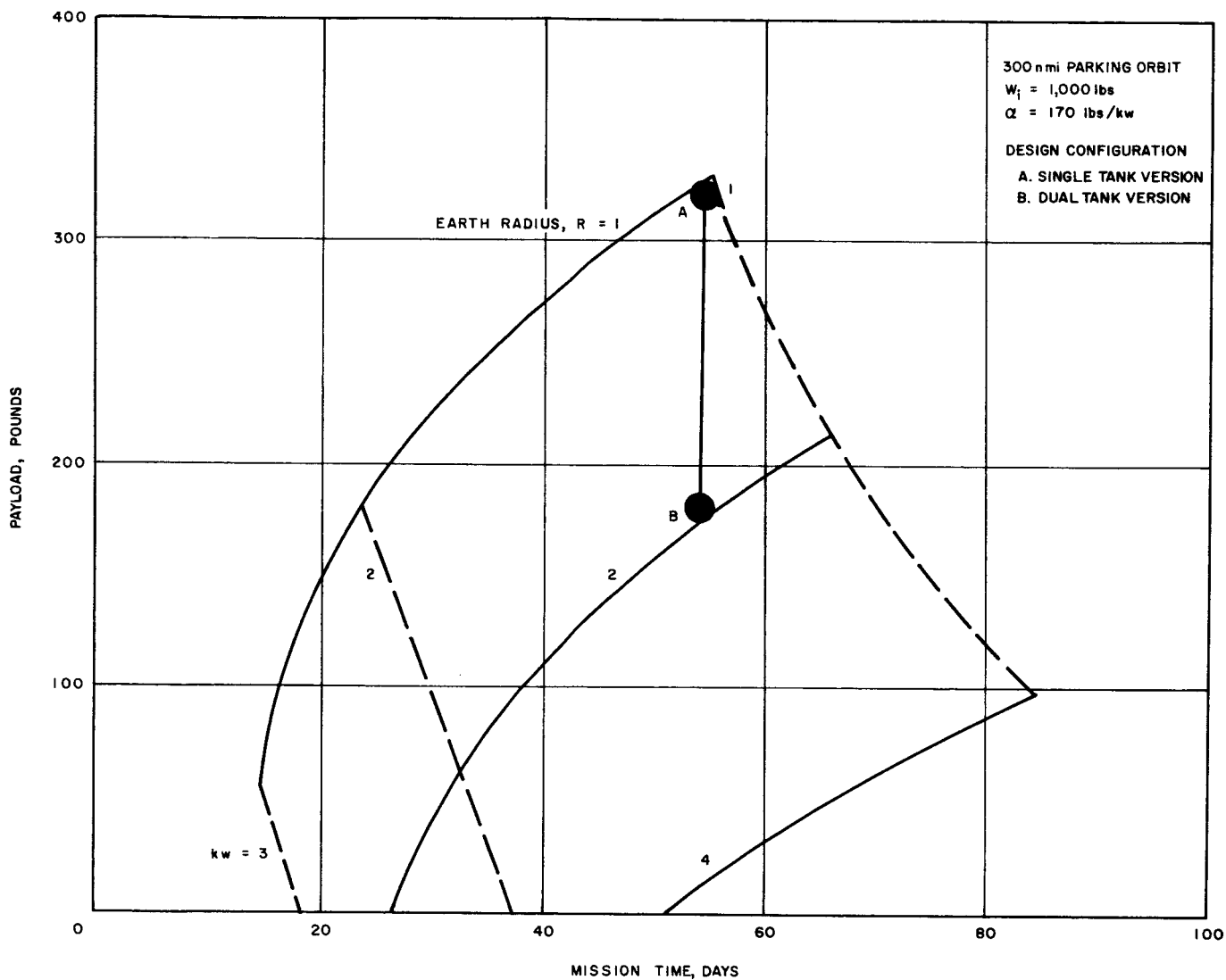


Figure 4-1 (continued).  
 d) Resisto-Jet Engine Spacecraft

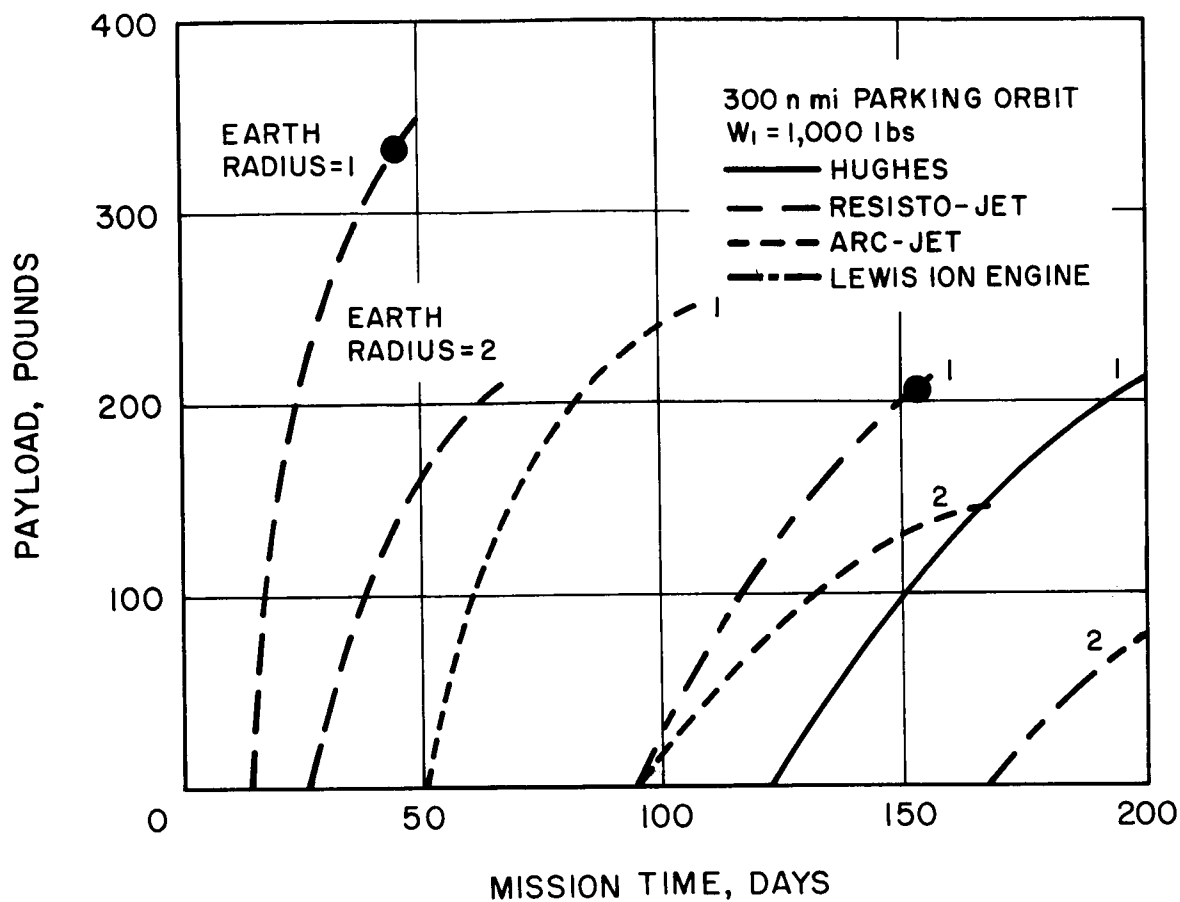


Figure 4-1 (continued).  
 e) Variation in Payload Capability with Engine Type

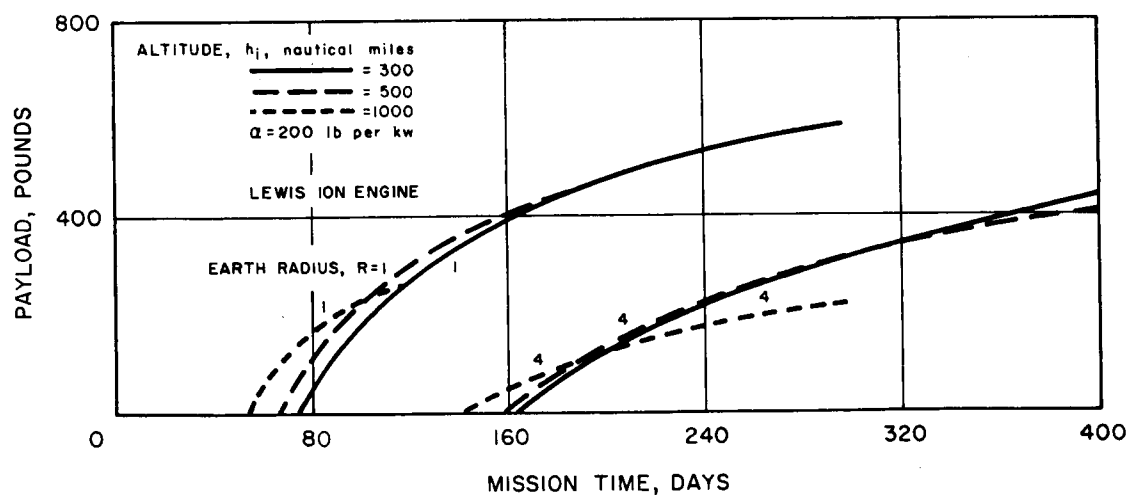


Figure 4-1 (continued).  
 f) Variation in Payload Capability with Parking Orbit Altitude

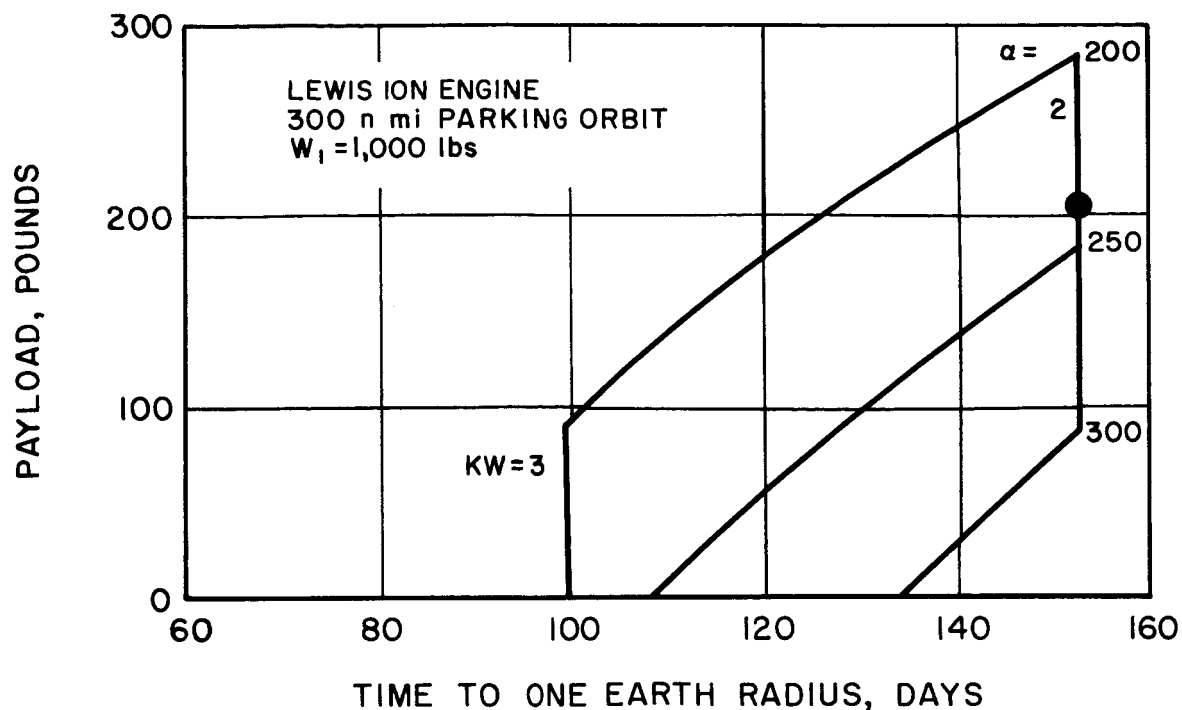


Figure 4-1 (continued).

g) Variation in Payload Capability with Specific Power Plant Weight

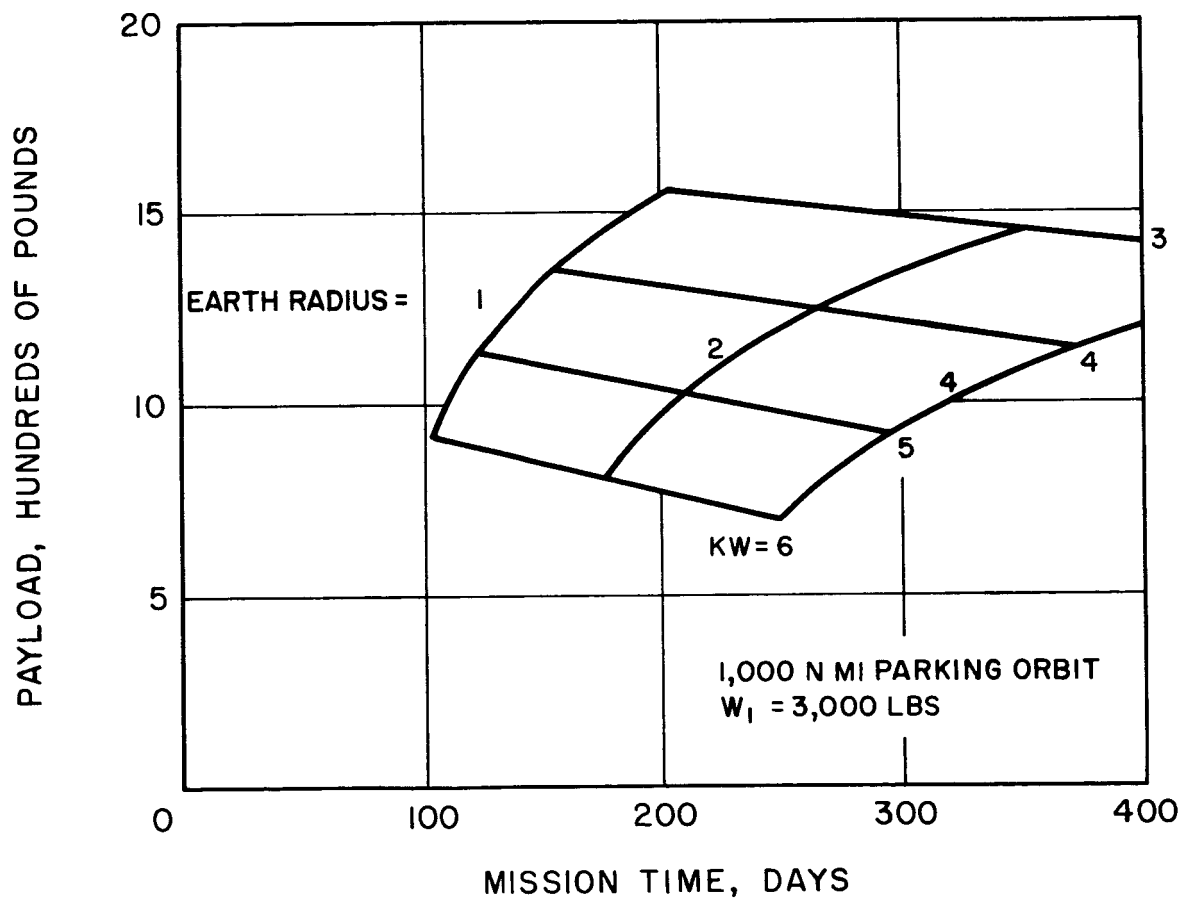
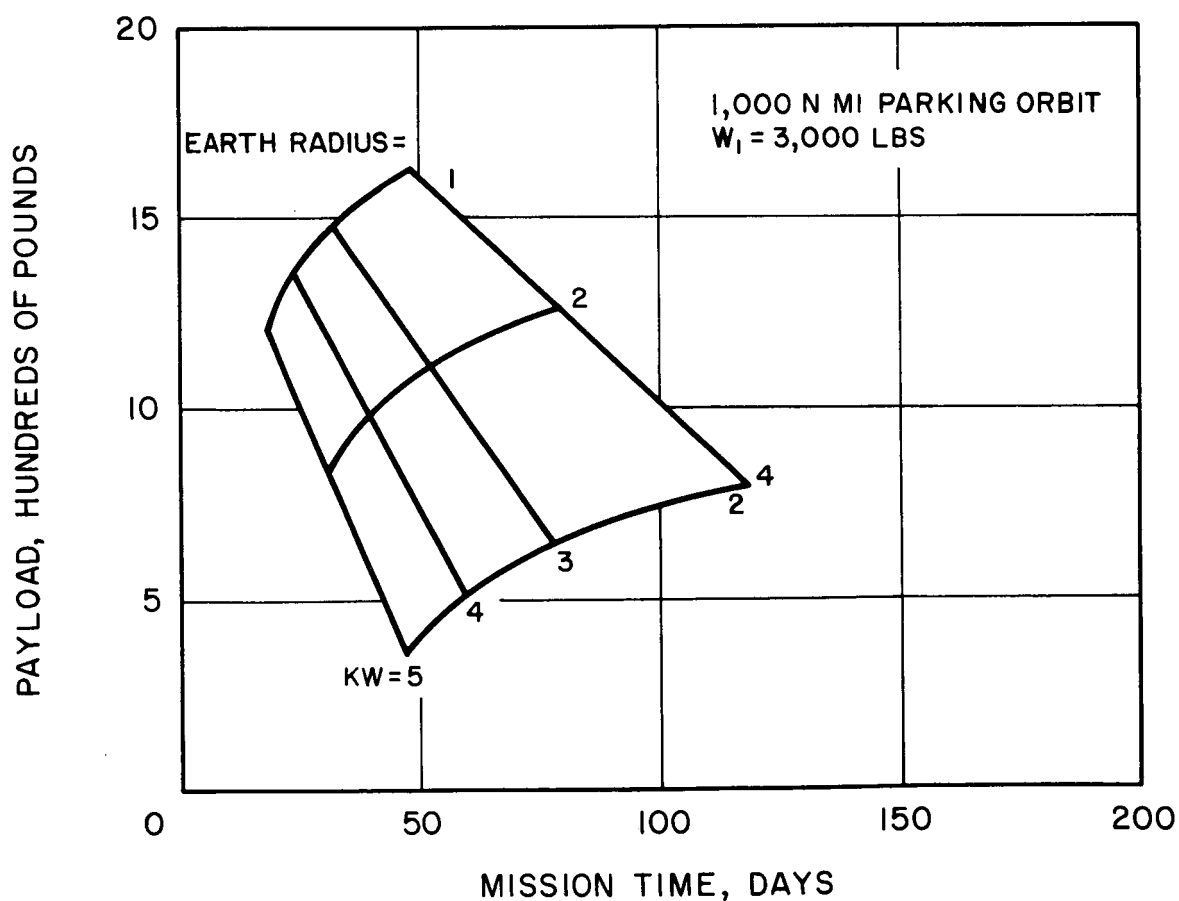
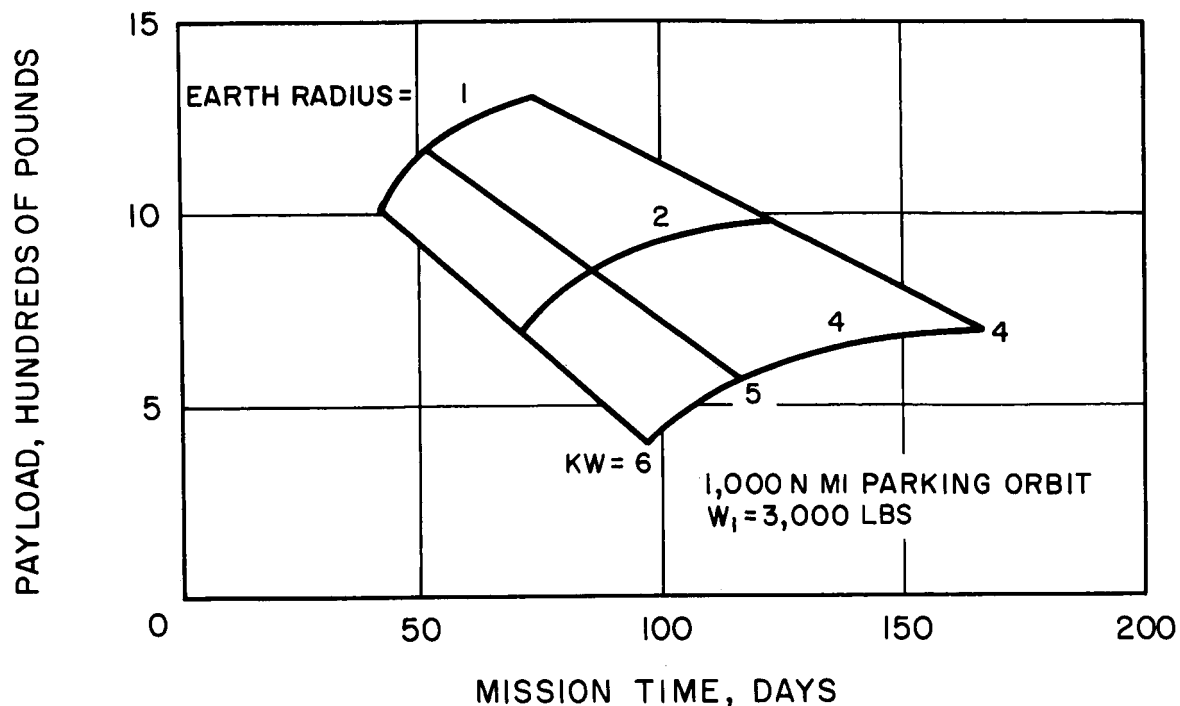


Figure 4-2. Polar Orbit Transfer Performance for Missions Utilizing Atlas-Agena B Launch Vehicle  
a) Lewis Ion Engine Spacecraft



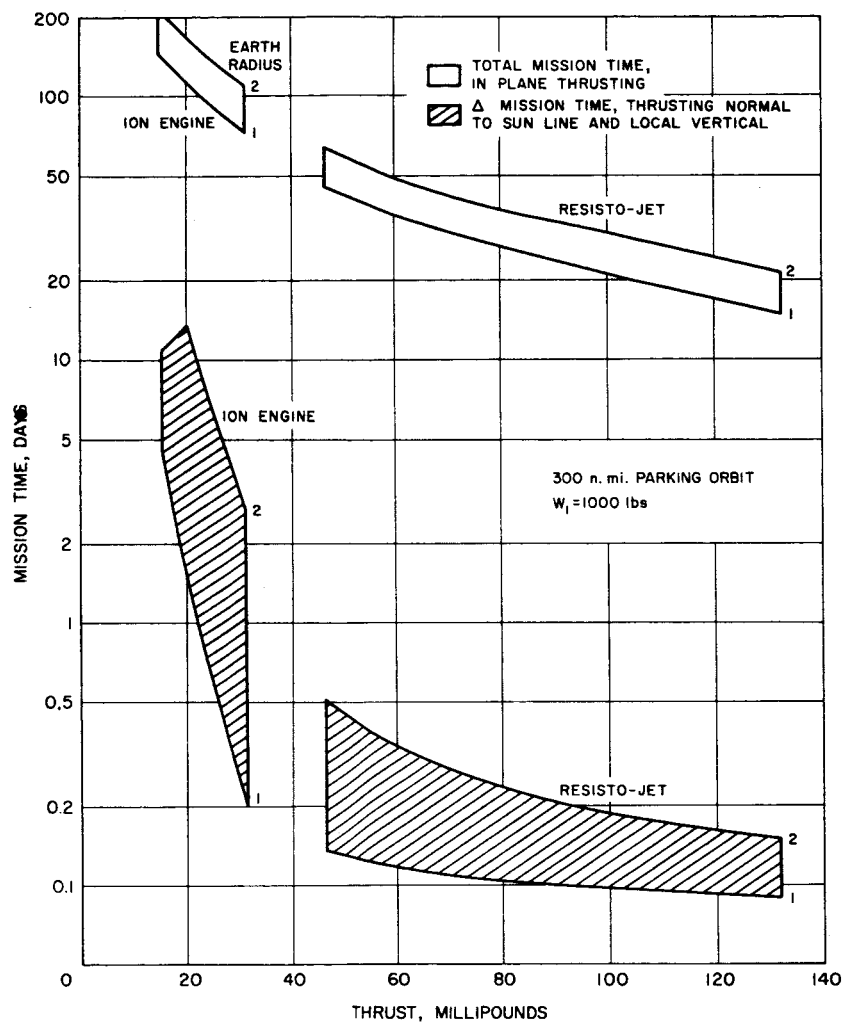


Figure 4-3. Effect of Thrust Vector Control on Polar Orbit Transfer Performance To One and Two Earth Radius Altitude



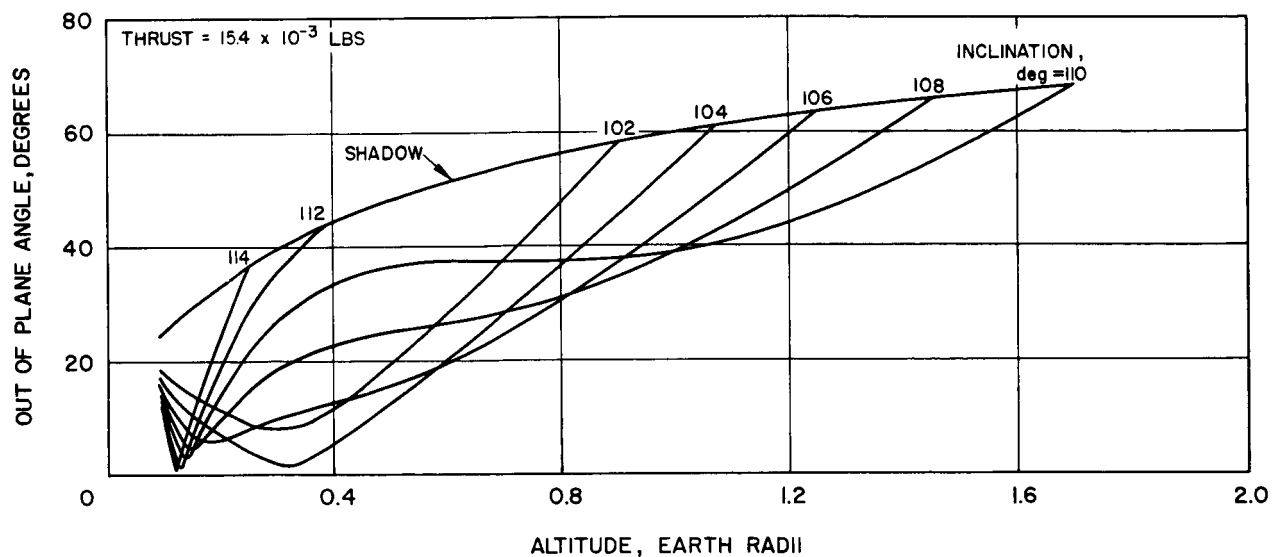


Figure 4-4. Out-of-Plane Thrust Angle Variation with Orbital Altitude  
 a) Lewis 2-kw Ion Engine Spacecraft  
 Launch Time: 5 a.m., December 21

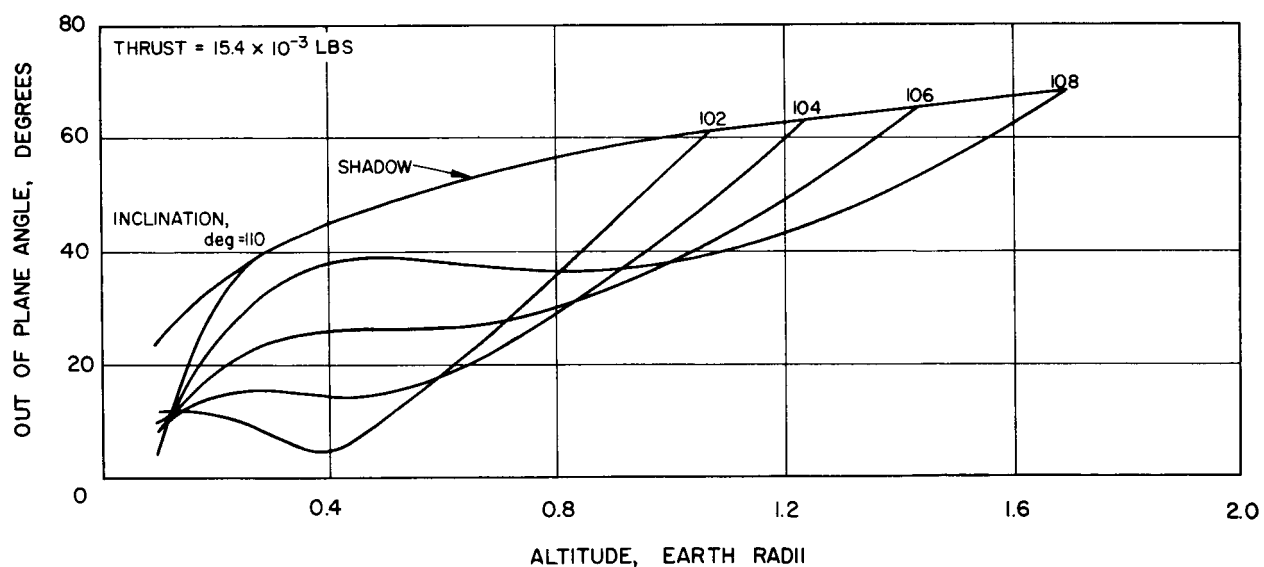


Figure 4-4 (continued).  
 b) Lewis 2-kw Ion Engine Spacecraft  
 Launch Time: 6 a.m., December 21

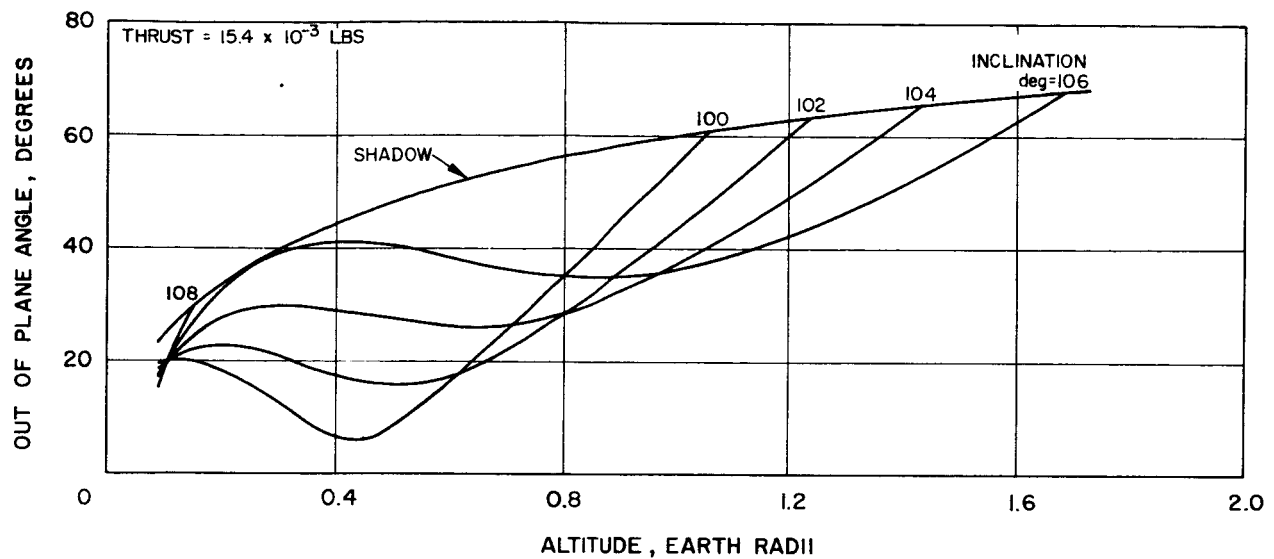


Figure 4-4 (continued).  
 c) Lewis 2-kw Ion Engine Spacecraft  
 Launch Time: 7 a.m., December 21

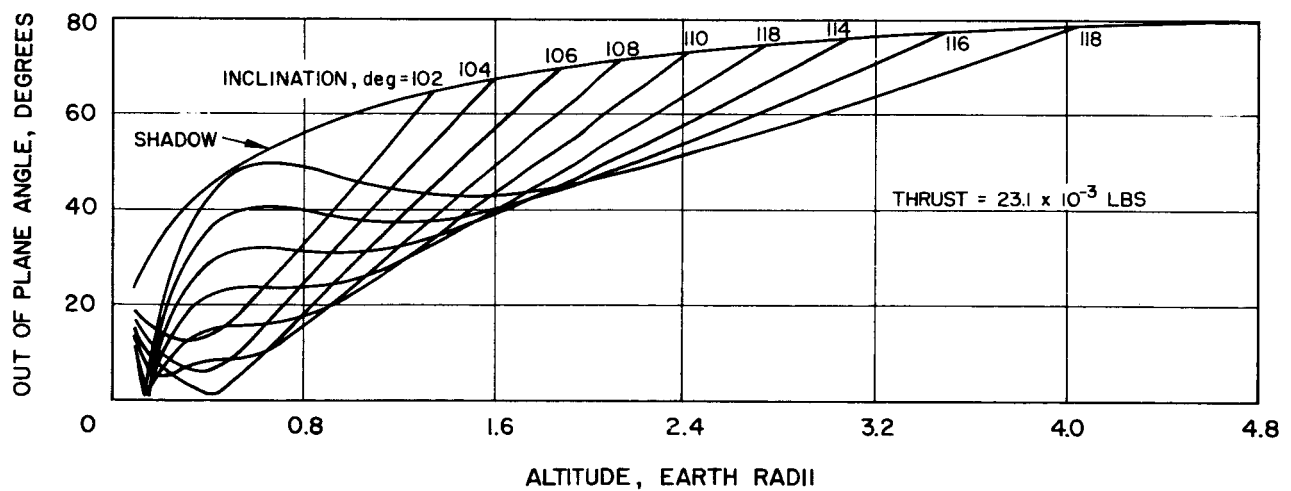


Figure 4-4 (continued).  
 d) Lewis 3-kw Ion Engine Spacecraft  
 Launch Time: 5 a.m., December 21

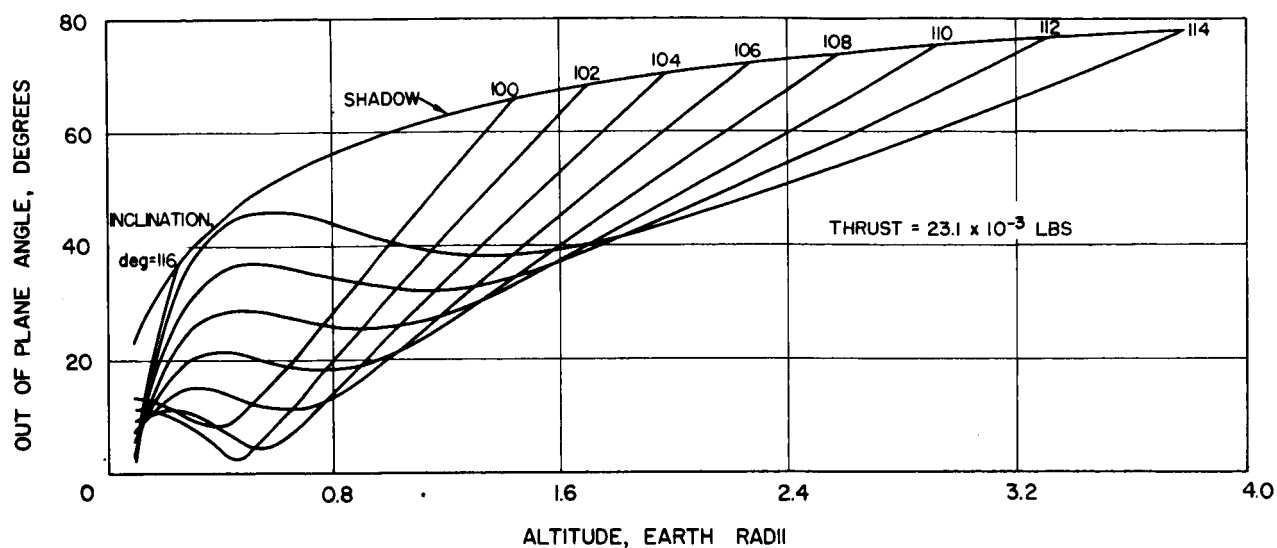


Figure 4-4 (continued).  
 e) Lewis 3-kw Ion Engine Spacecraft  
 Launch Time: 6 a.m., December 21

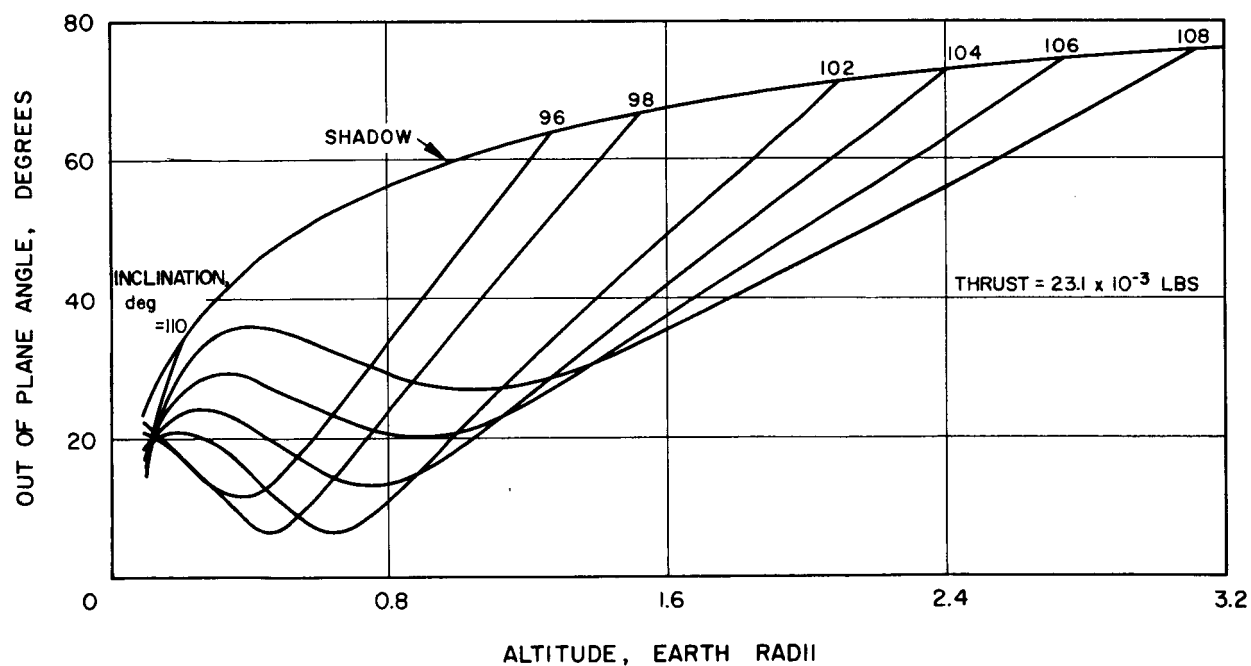


Figure 4-4 (continued).  
 f) Lewis 3-kw Ion Engine Spacecraft  
 Launch Time: 7 a.m., December 21

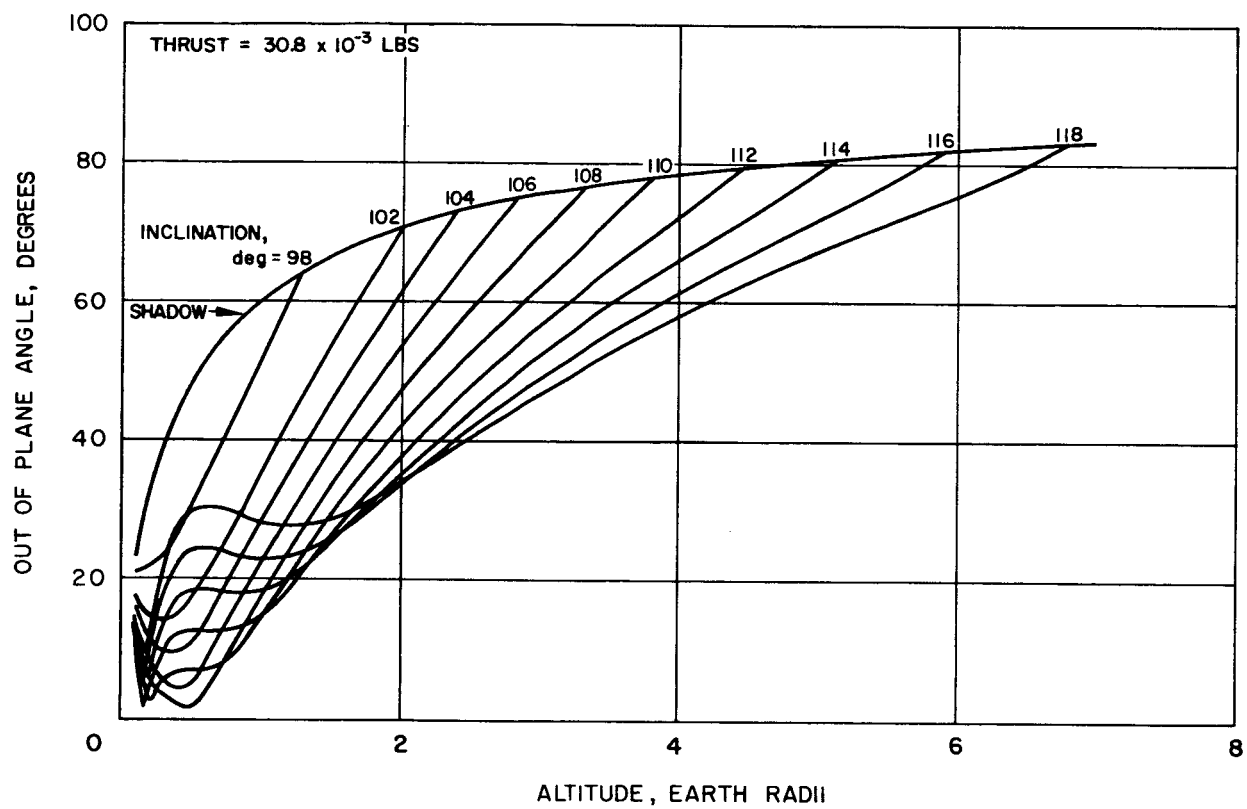


Figure 4-4 (continued).  
 g) Lewis 4-kw Ion Engine Spacecraft  
 Launch Time: 5 a.m., December 21

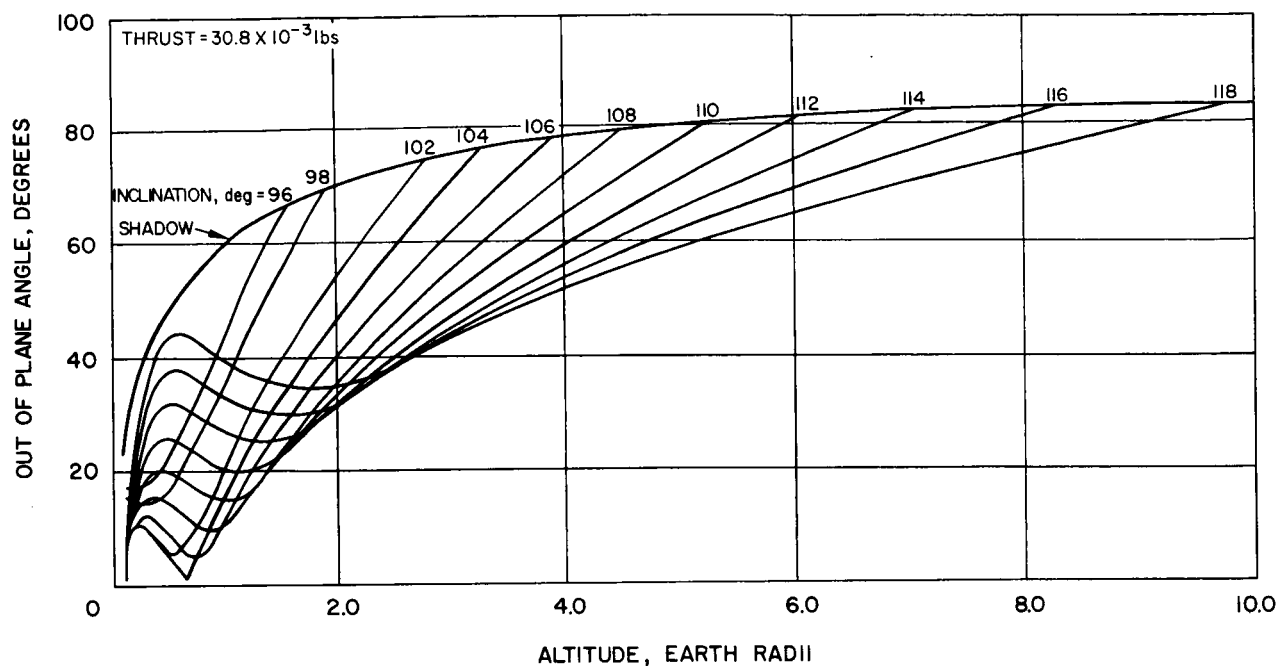


Figure 4-4 (continued).  
h) Lewis 4-kw Ion Engine Spacecraft  
Launch Time: 6 a.m., December 21

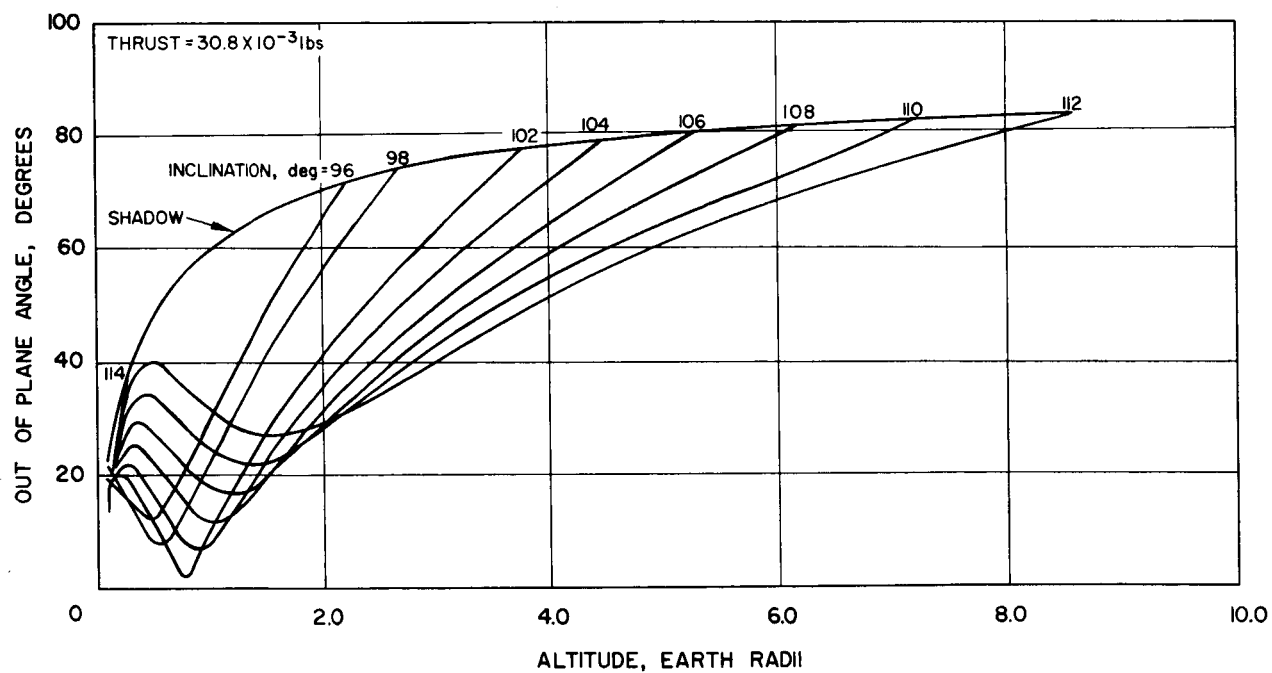


Figure 4-4 (continued).  
i) Lewis 4-kw Ion Engine Spacecraft  
Launch Time: 7 a.m., December 21

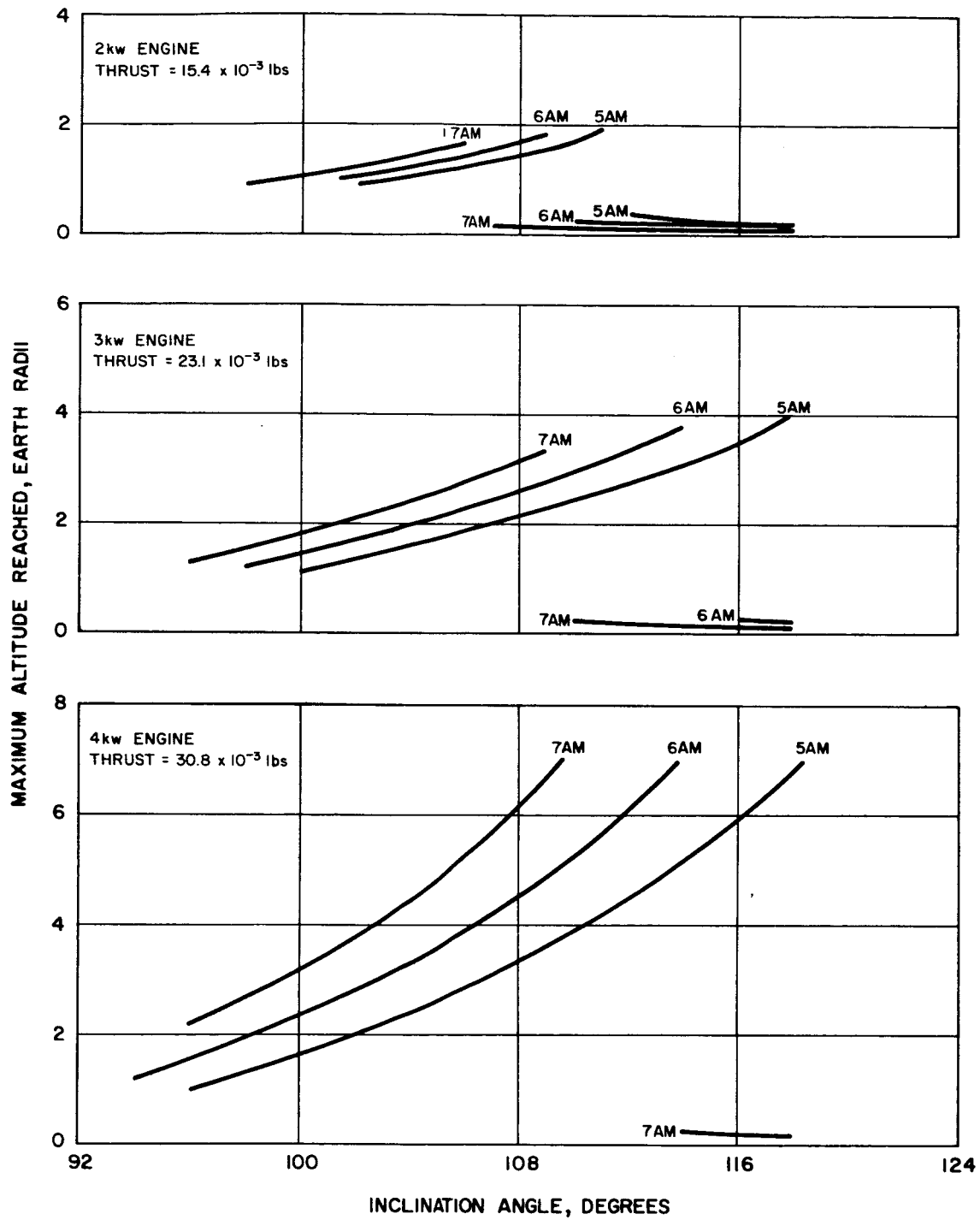


Figure 4-5. Effect of Orbit Inclination on Maximum Altitude Attained, Launch Date December 21

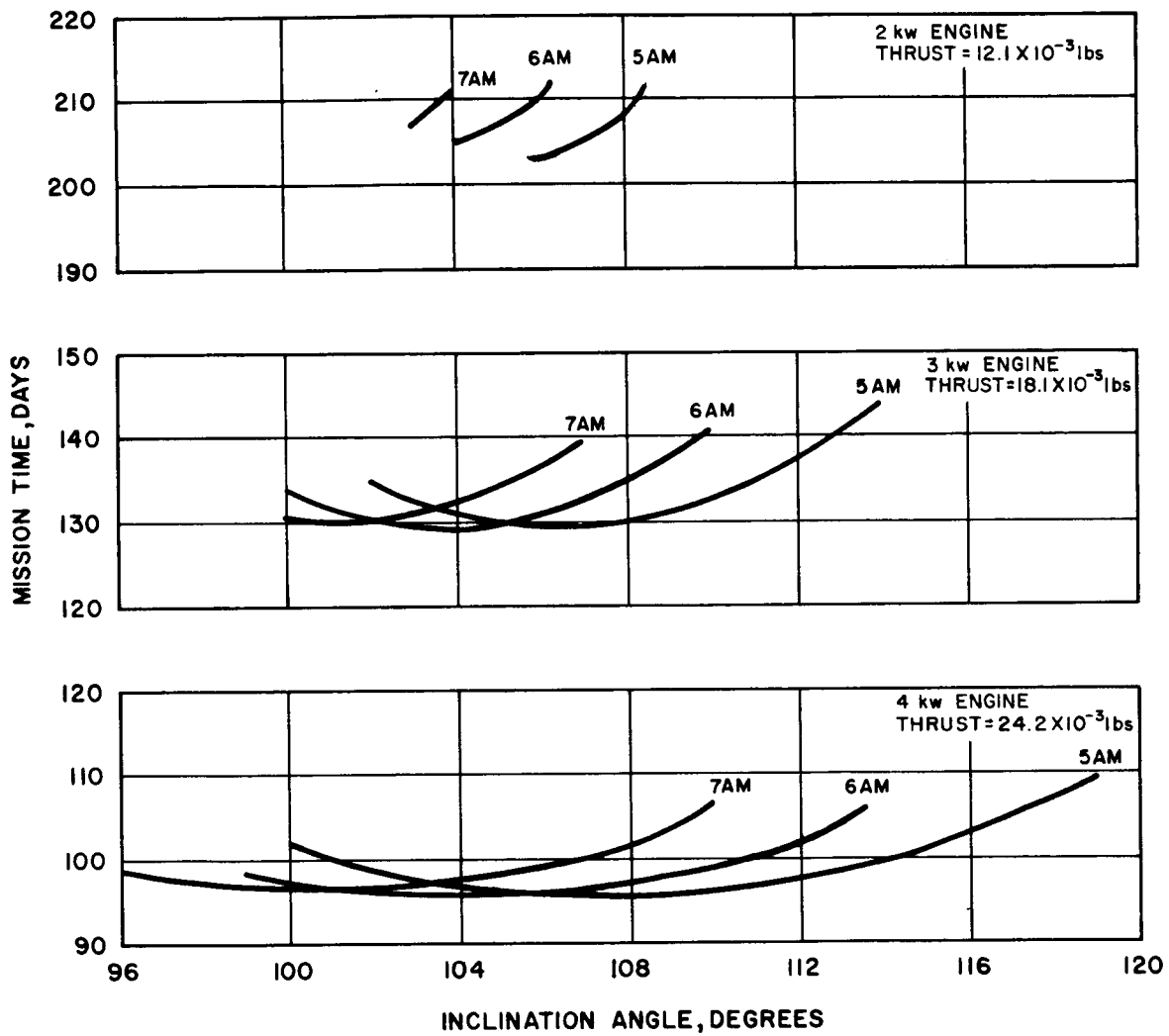


Figure 4-6. Effect of Launch Conditions on Time to Altitude,  
Launch Date December 21

a) Time to One Earth Radius - Hughes Ion Engine Spacecraft

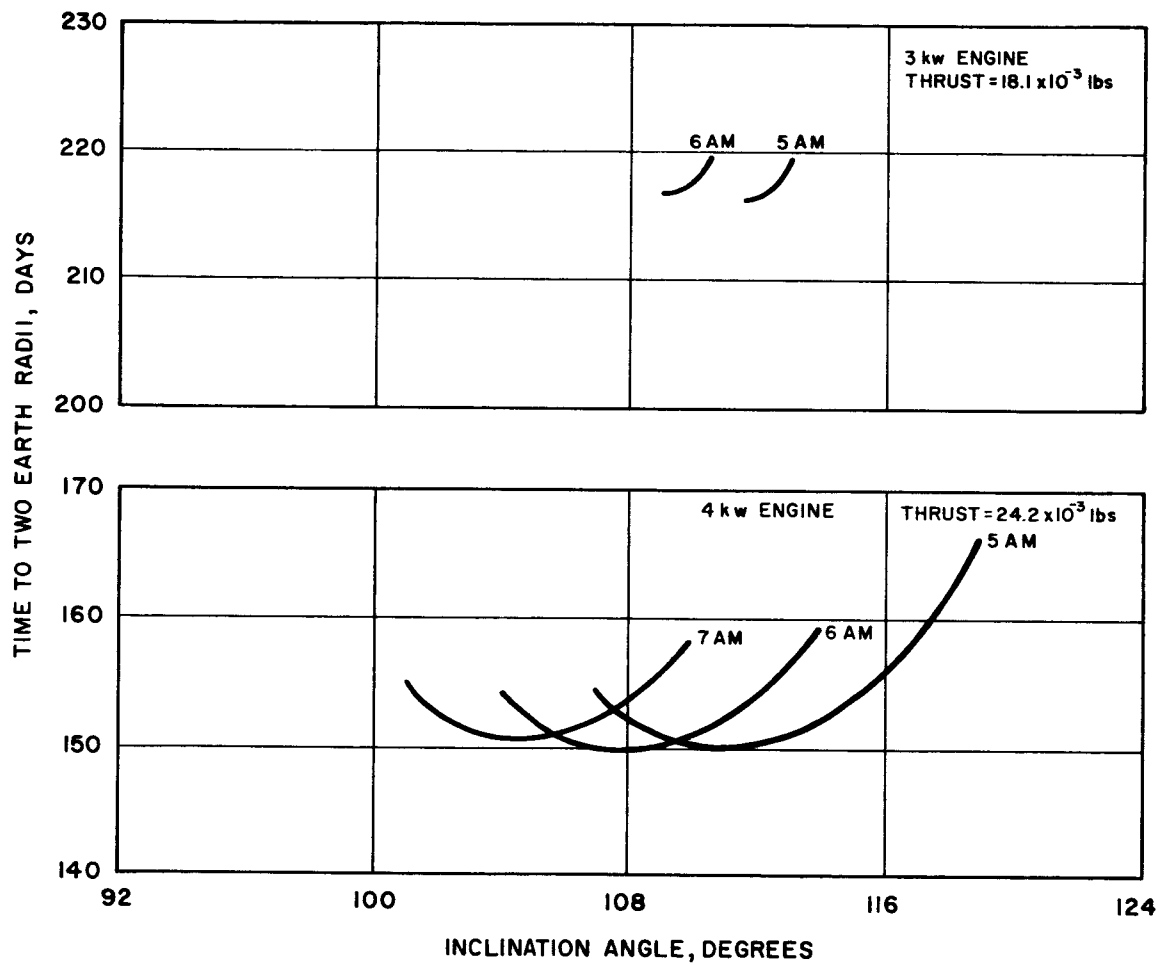


Figure 4-6 (continued).  
 b) Time to Two Earth Radii - Hughes Ion Engine Spacecraft



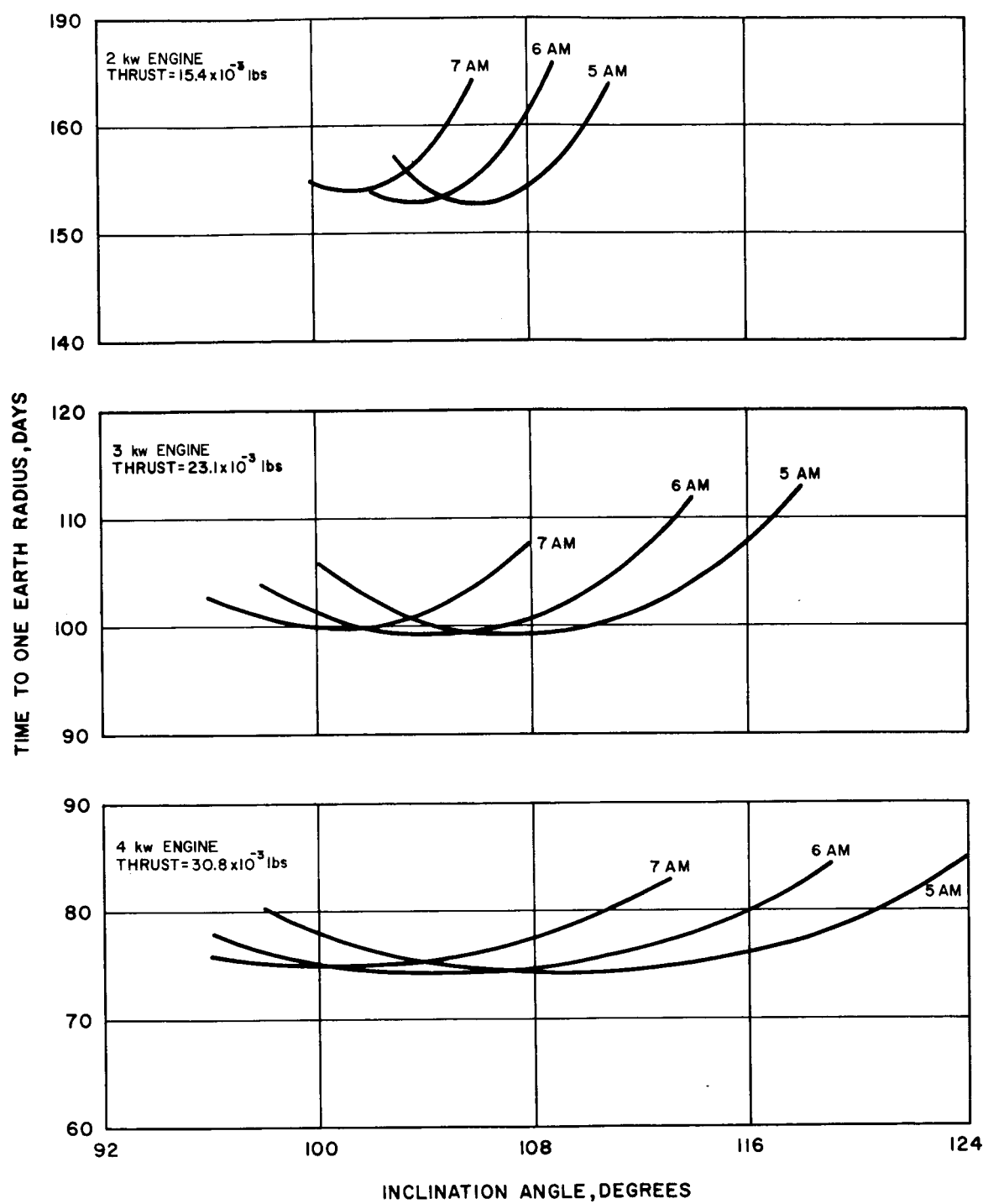


Figure 4-6 (continued).  
 c) Time to One Earth Radius - Lewis Ion Engine Spacecraft

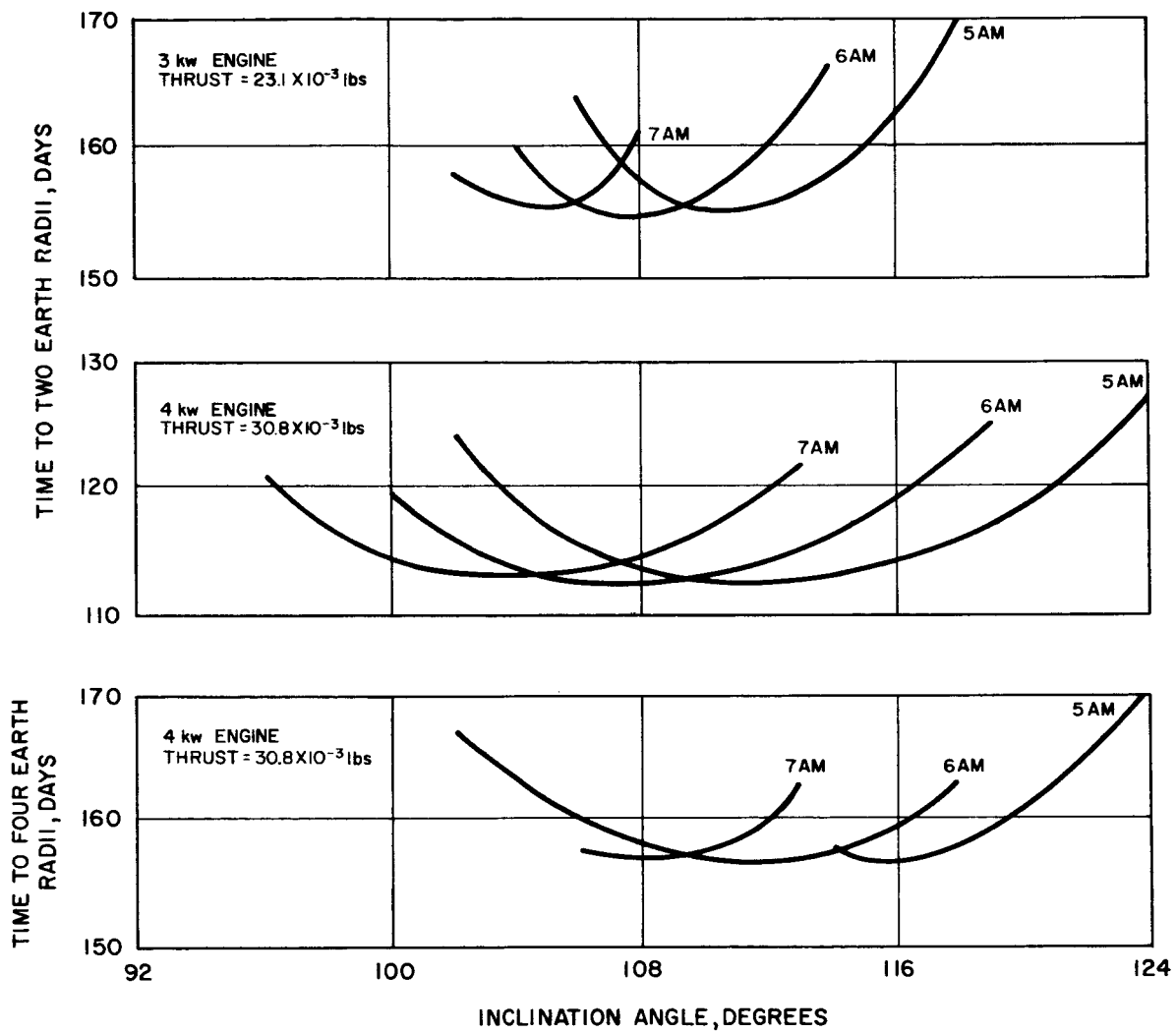


Figure 4-6 (continued).  
 d) Time to Two and Four Earth Radii - Lewis Ion Engine Spacecraft

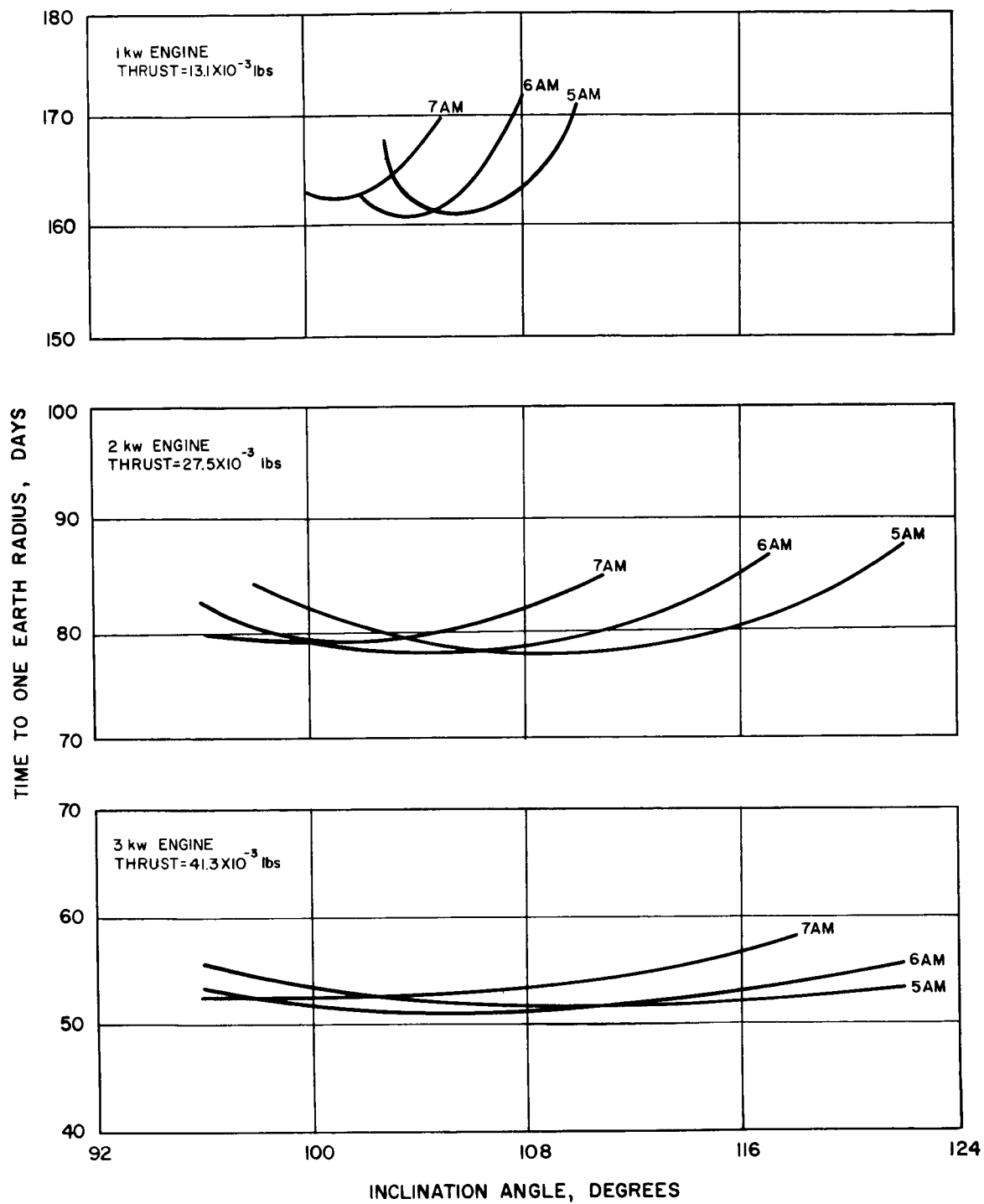


Figure 4-6 (continued).  
e) Time to One Earth Radius - Plasmadyne Arc-Jet Engine Spacecraft

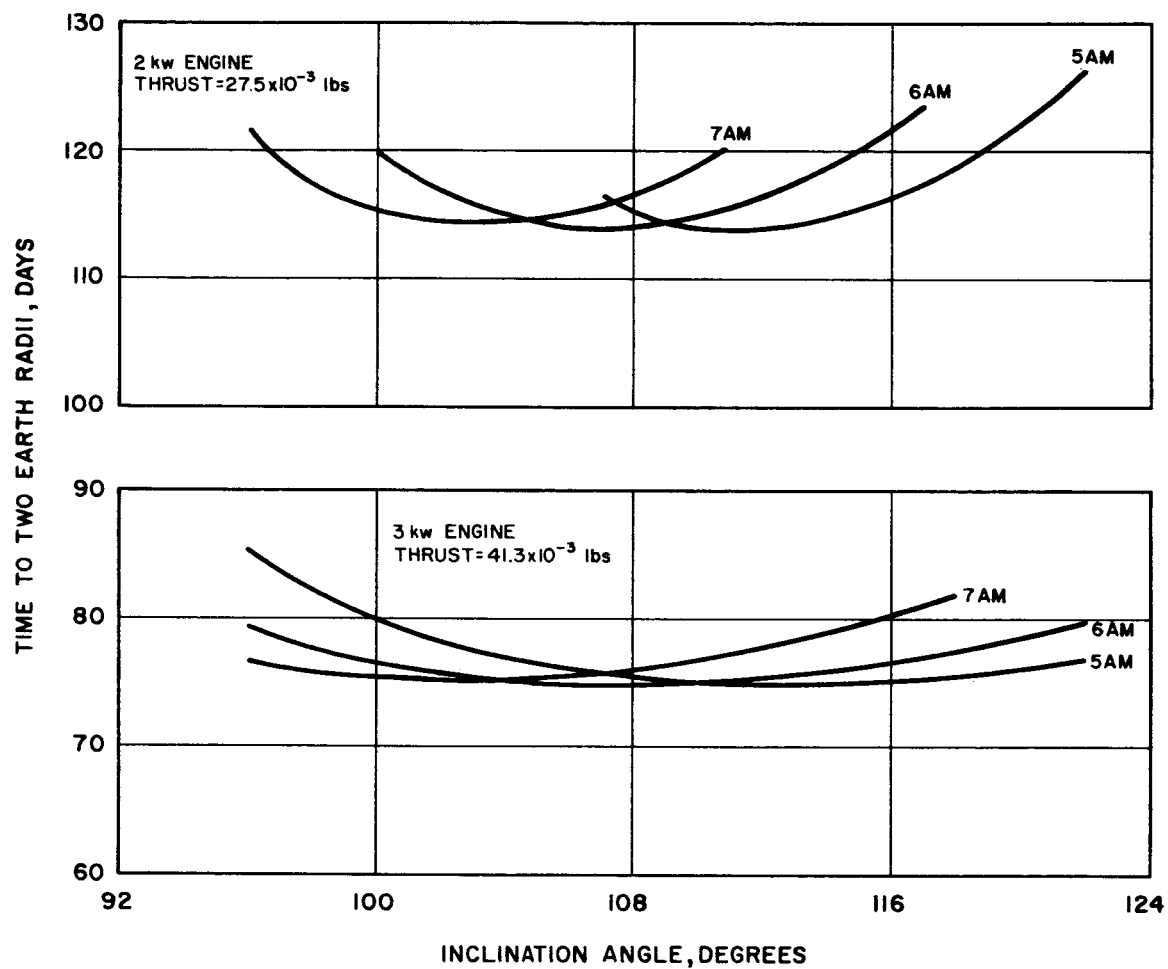


Figure 4-6 (continued).  
f) Time to Two Earth Radii - Plasmadyne Arc-Jet Engine Spacecraft

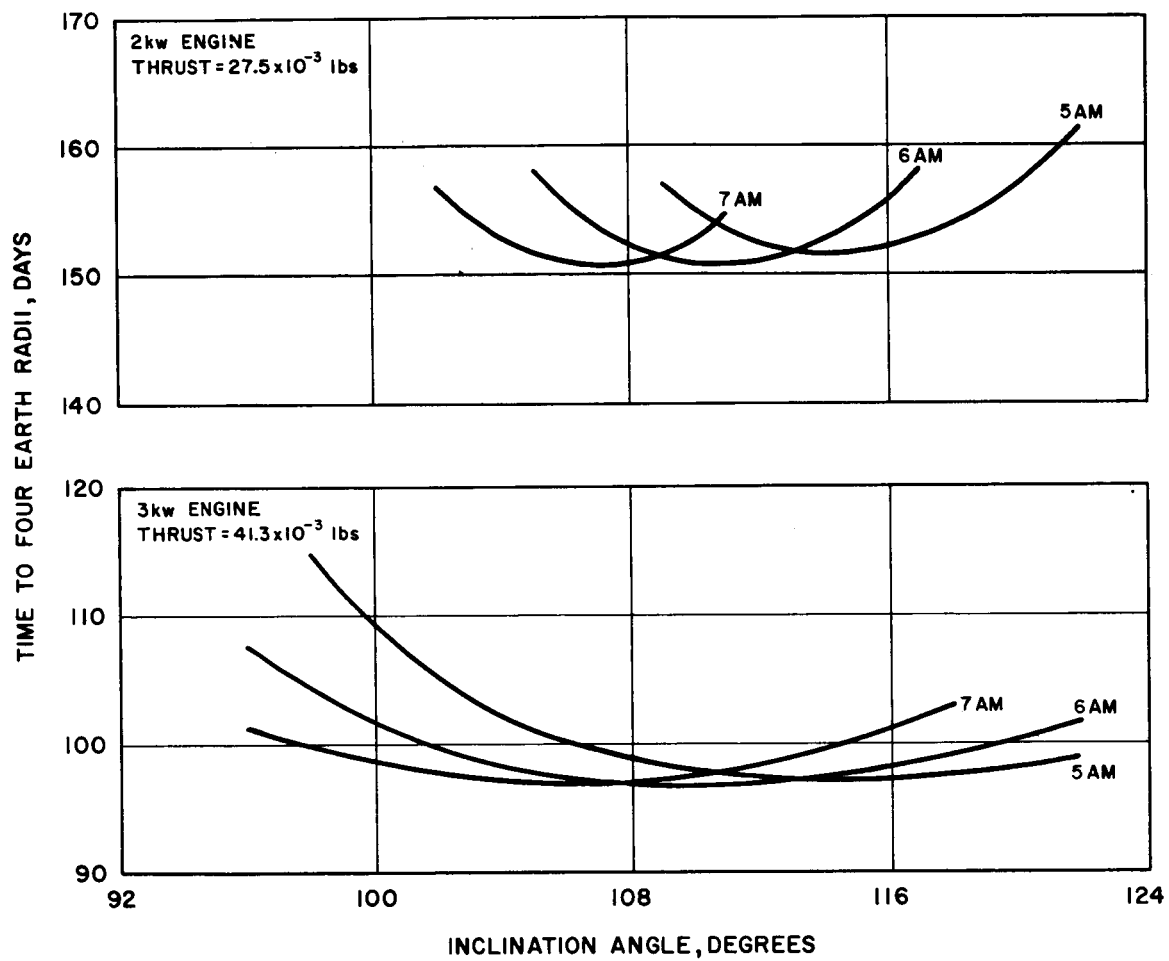


Figure 4-6 (continued).  
g) Time to Four Earth Radii - Plasmadyne Arc-Jet Engine Spacecraft

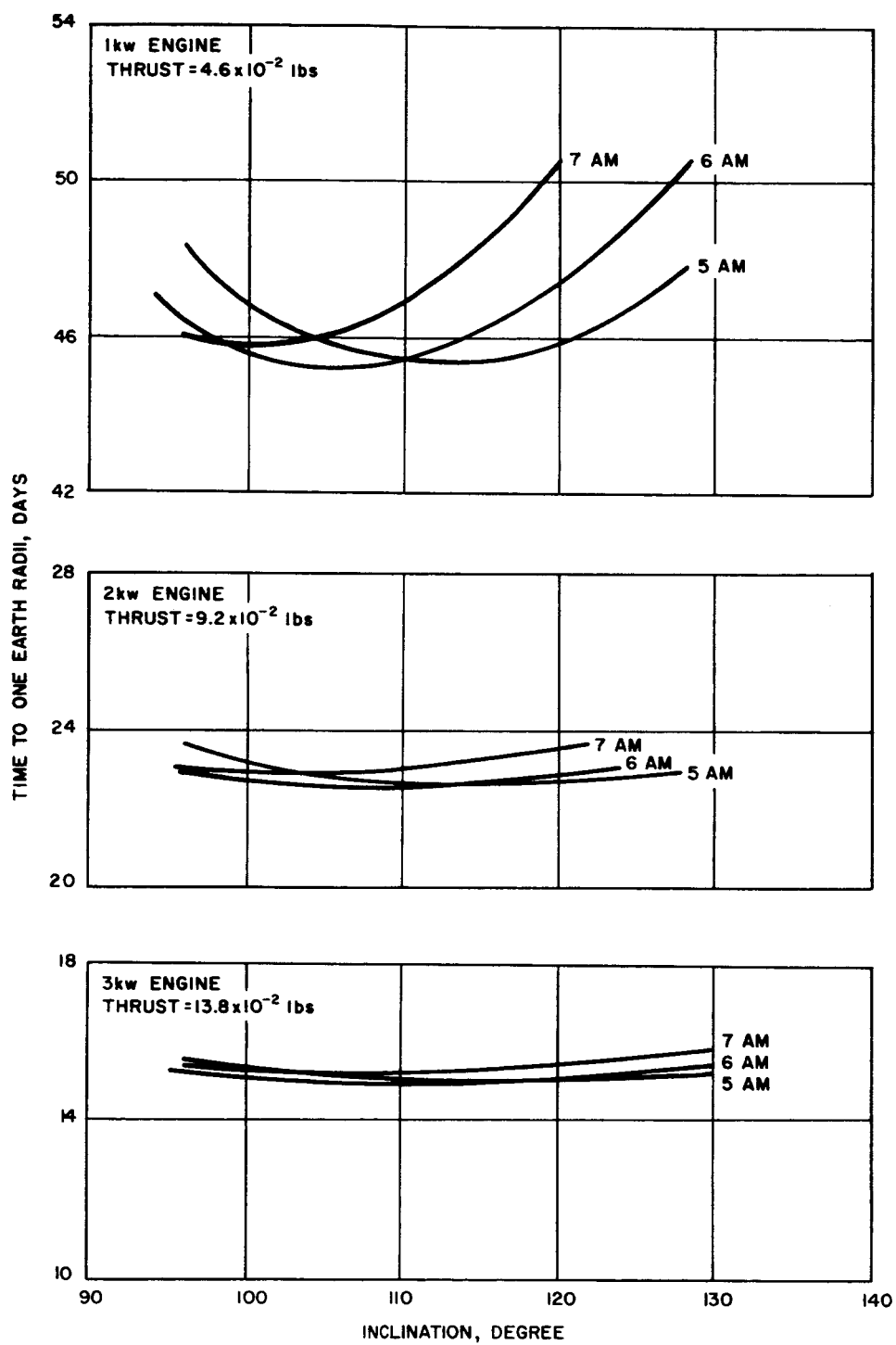


Figure 4-6 (continued).  
h) Time to One Earth Radius - Resisto-Jet Engine Spacecraft

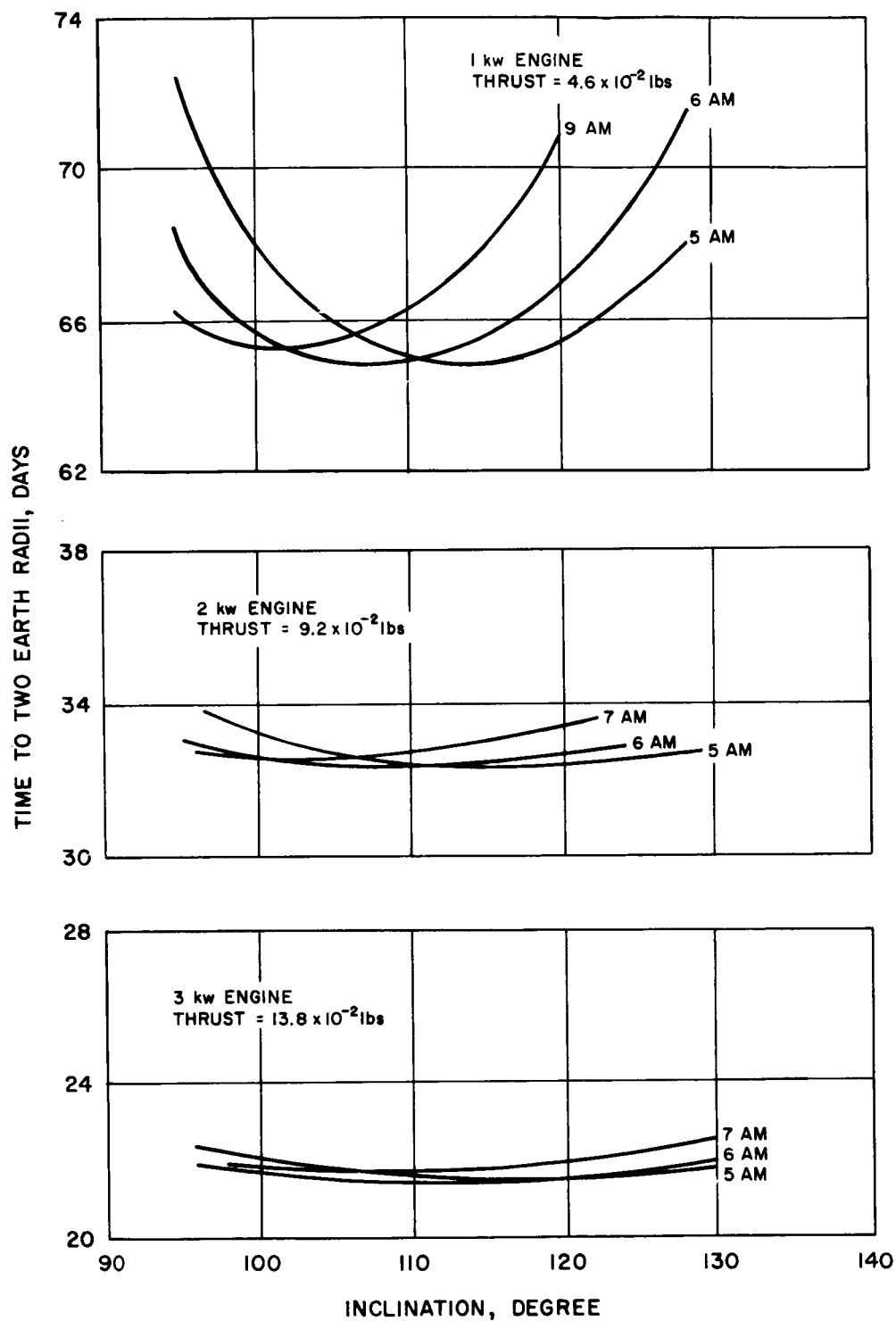


Figure 4-6 (continued).  
i) Time to Two Earth Radii - Resisto-Jet Engine Spacecraft

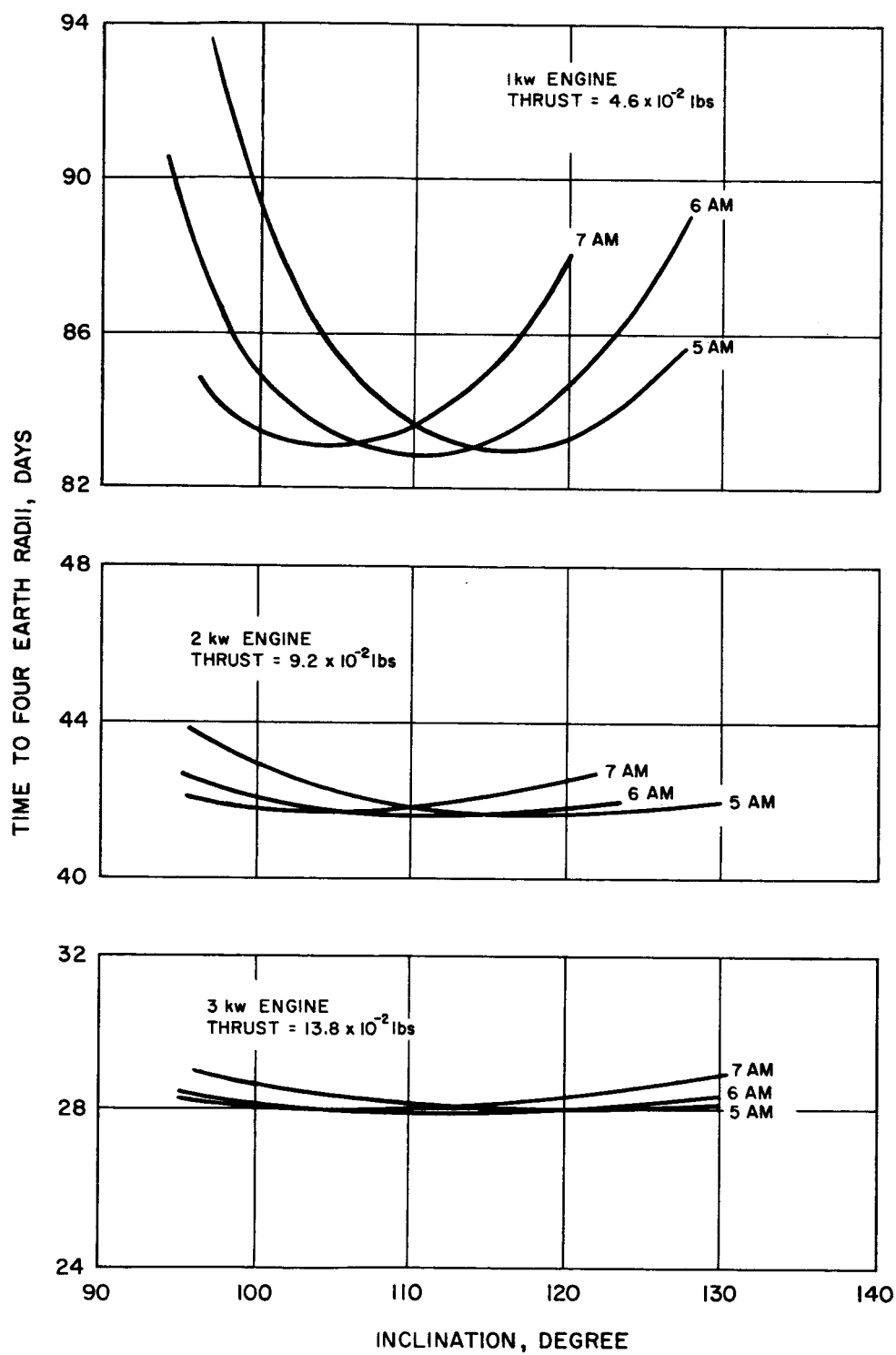


Figure 4-6 (continued).  
j) Time to Four Earth Radii - Resisto-Jet Engine Spacecraft



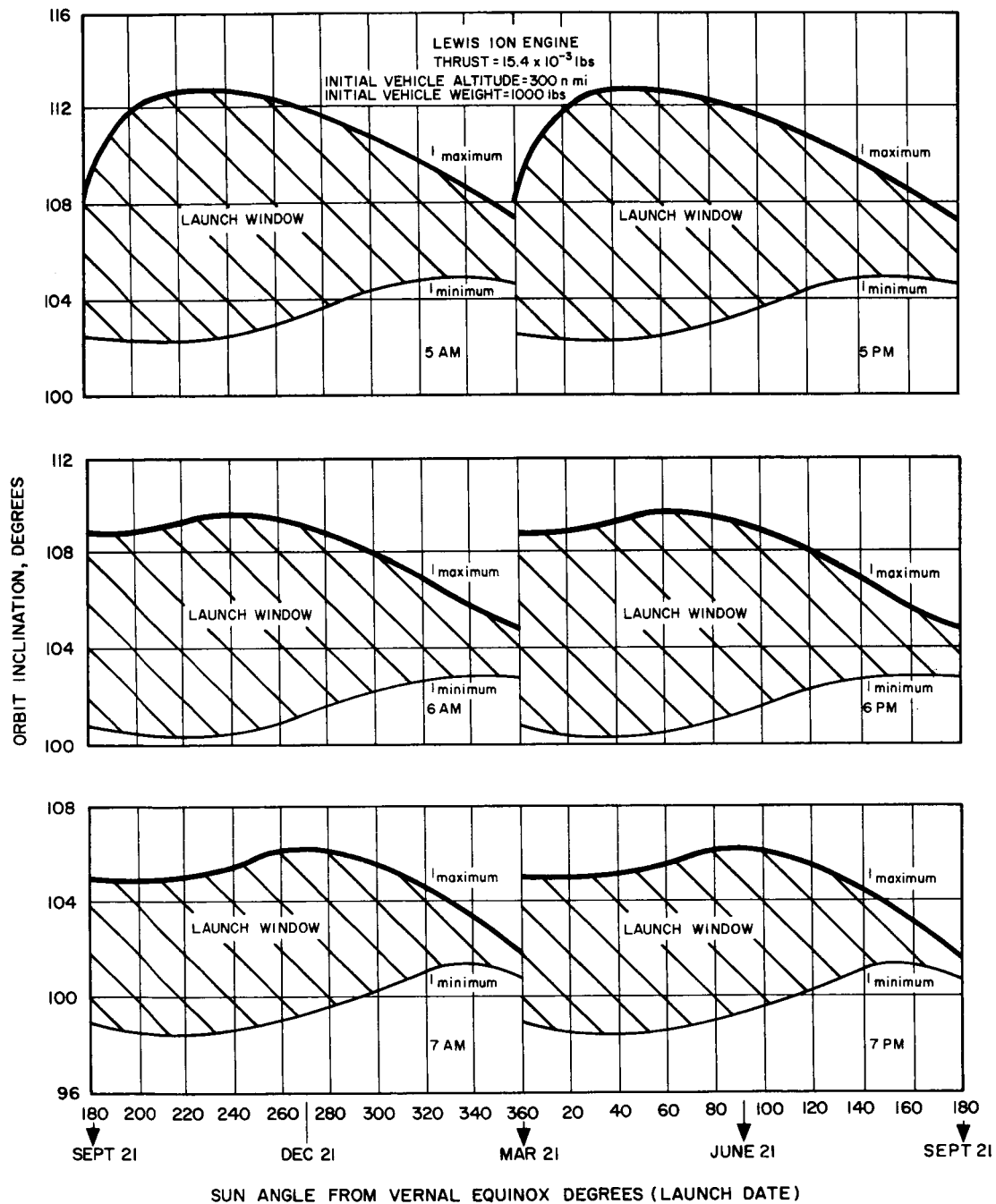


Figure 4-7. Variation of Launch Window with Time of Year for Polar Orbit Transfer Missions

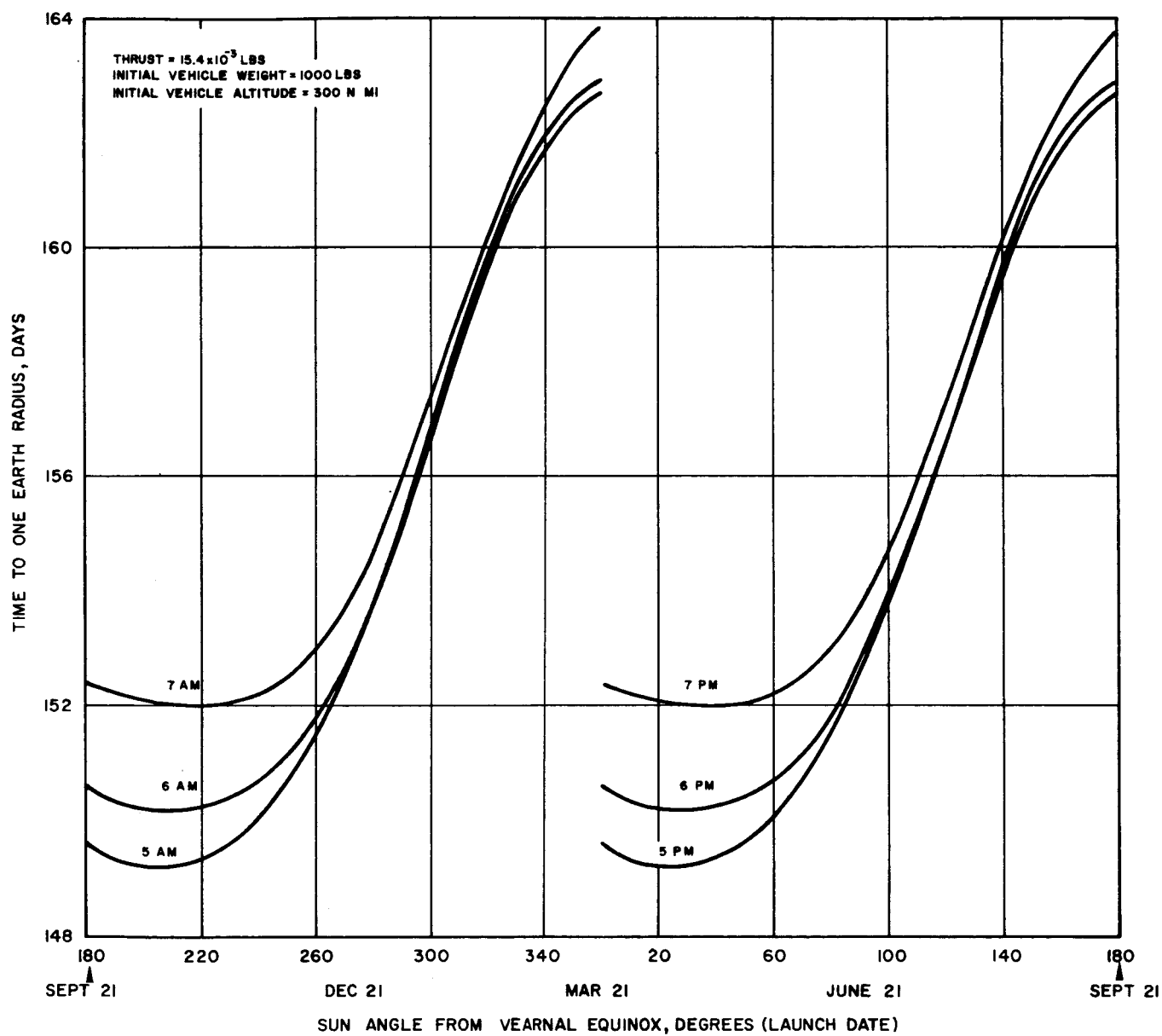


Figure 4-8. Variation of Time to Altitude with Time of Year for Polar Orbit Transfer Missions

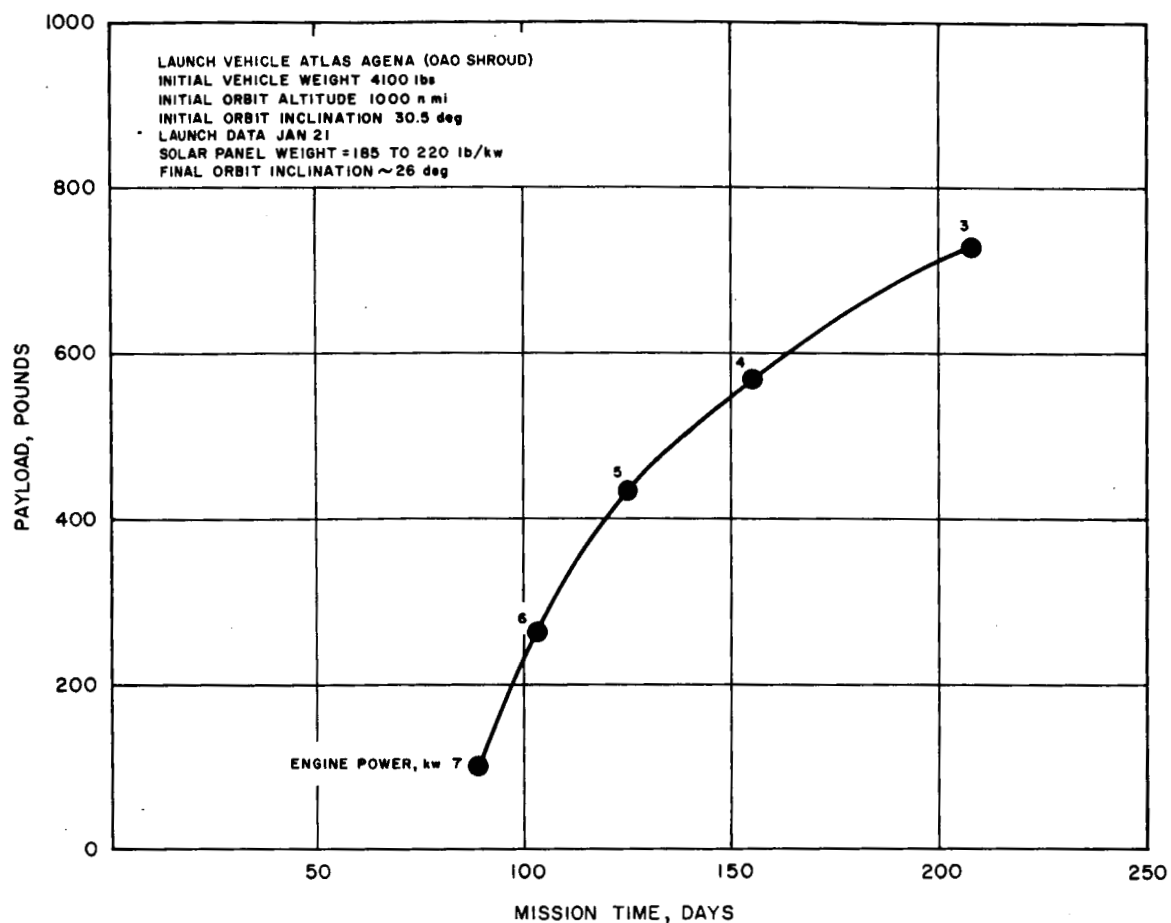


Figure 4-9. Equatorial 24-hour Orbit Transfer Performance for a Resisto-Jet Engine Spacecraft Atlas Agena B Launch Vehicle

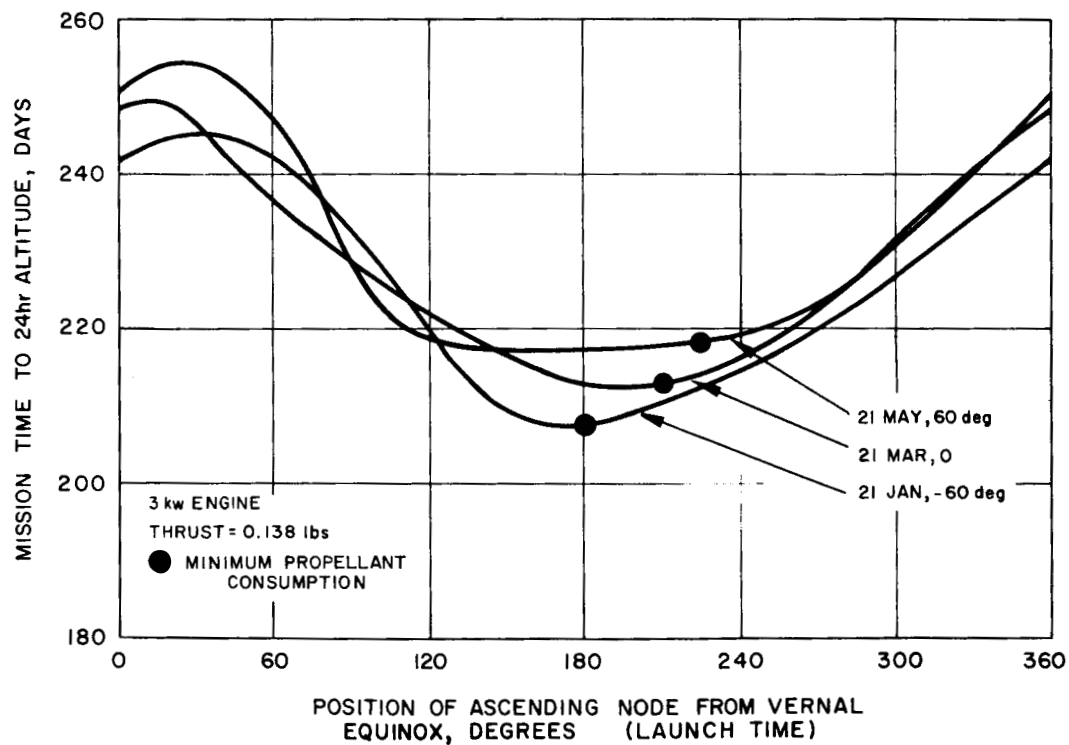


Figure 4-10. Effect of Daily Launch Time on Mission Time for a Resisto-Jet Engine Spacecraft Atlas-Agena B Launch Vehicle

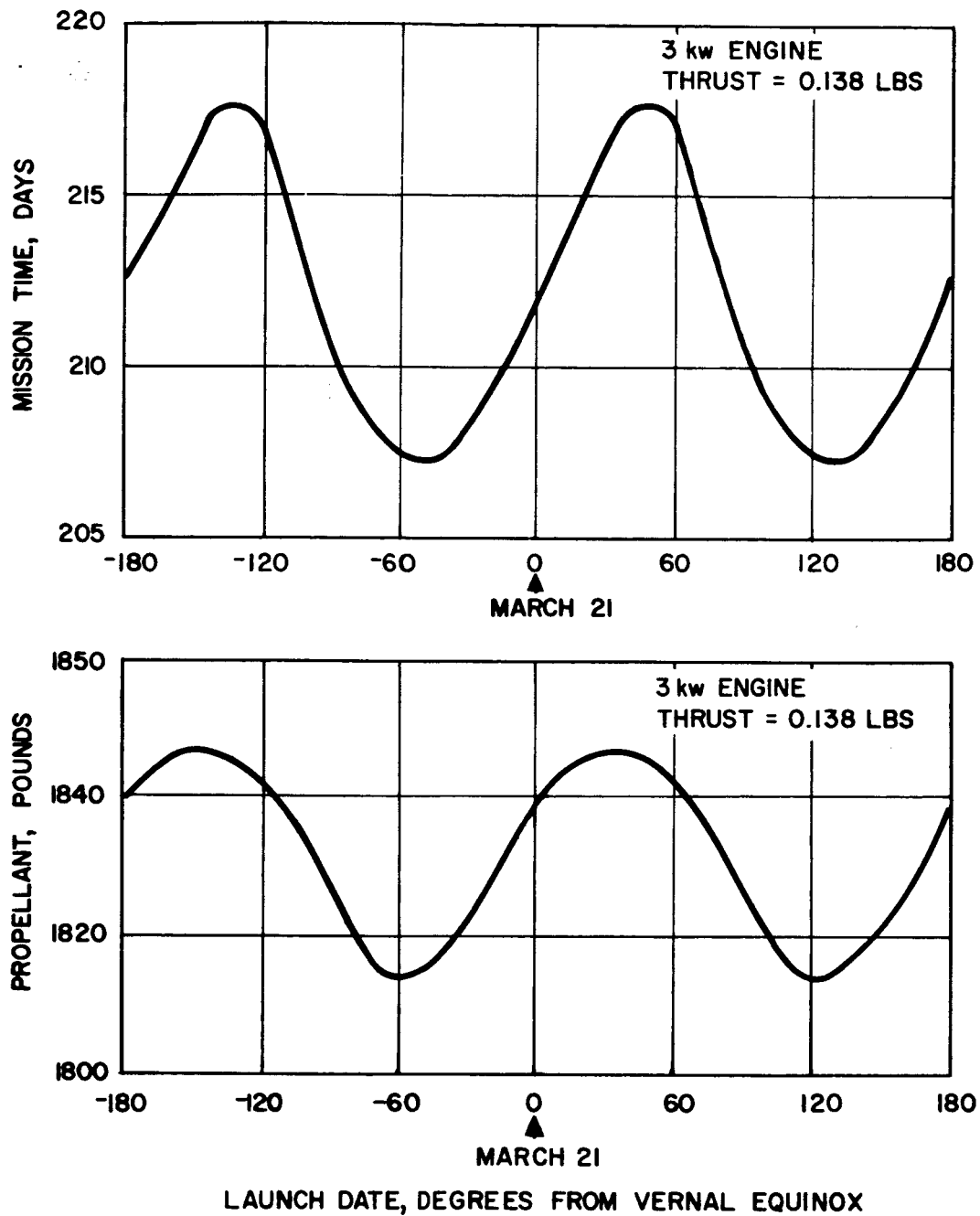


Figure 4-11. Effect of Launch Data on Mission Time for a Resisto-Jet Engine Spacecraft  
Atlas-Agena B Launch Vehicle

## 5. SPACECRAFT SYSTEM DESIGN

### SOLAR-ELECTRIC PROPULSION SYSTEMS

#### Solar Cell Power System Design

##### Radiation Damage

Space Environment. The radiation spectrum of the geocentric radiation zone used for this analysis is shown as Figure 5-1 for protons and Figure 5-2 for the electrons. These have been determined from References 1 through 9. The data shown are considered as omnidirectional fluxes. They are subject to uncertainties of an order of magnitude, particularly for the distribution of particles with energies less than 10 mev. Little is known of the proton spectrum in the region of the inner radiation zone for energies less than 10 mev.

Mission Considerations. Four missions have been selected to cover the time spectrum spiraling to a specific altitude at a slow rate and at a high rate. The missions used are shown in Figure 5-3. Two thrust levels of ion engines and two thrust levels of the resisto-jet were selected to cover the spectrum. The missions are covered in Section 3 of this report.

Solar Cell Degradation. Solar cells are affected by high-energy corpuscular radiations either by changes in carrier lifetimes or by changes in energy levels in the material. The carrier lifetime is the most sensitive parameter affected by radiation in silicon solar cells; the lifetime is decreased by radiation which correspondingly decreases the short-circuit current available from the cell. A comprehensive discussion of the theory concerning radiation damage to solar cells can be found in References 10 through 15.

A knowledge of the integrated flux and the type of cell to be used, which determines the critical flux value,  $\phi_c$ , can be used to determine the percentage degradation caused by the particle irradiation. Reference 16 was used to obtain the equation for calculating degradations:

$$\frac{Q}{100} = \left[ \frac{7}{9} \left( \frac{\phi}{\phi_c} \right)^{1/2} + 1 \right]^{-1/2}$$

where

$Q$  = percent of initial output of solar cell

$\phi$  = total integrated particle flux taken from Figure 5-1 that strikes solar cell

$\phi_c$  = integrated flux necessary to reduce short-circuit current by 25 percent

There are two uncertainties in using this expression. First, there exist uncertainties in the integrated flux parameter  $\phi_c$ . The variation of  $\phi_c$  with particle energy is shown in Figures 5-4 and 5-5 for proton and electron fluxes respectively.

The representative values of  $\phi_c$  used in the computation are as follows:

$\phi_c$  (protons)  $5.8 \times 10^{10}$  particles  $\text{cm}^{-2} \text{sec}^{-1}$

$\phi_c$  (electrons)  $1.0 \times 10^{15}$  particles  $\text{cm}^{-2} \text{sec}^{-1}$

Upper and lower limits to account for uncertainties are as follows:

$\phi_c$  (protons)

Upper:  $1.9 \times 10^{11}$  protons  $\text{cm}^{-2} \text{sec}^{-1}$

Lower:  $1.9 \times 10^{10}$  protons  $\text{cm}^{-2} \text{sec}^{-1}$

$\phi$  (electrons)

Upper:  $1.5 \times 10^{15}$  electrons  $\text{cm}^{-2} \text{sec}^{-1}$

Lower:  $1.5 \times 10^{14}$  electrons  $\text{cm}^{-2} \text{sec}^{-1}$

These values constitute the possible variation within the makeup of the solar cell and uncertainty in the measurement of  $\phi_c$ .

Second, the total external dose impinging on the solar cell panels is uncertain because of lack of knowledge in the following areas:

- 1) Actual flux rates and energy spectra.
- 2) Percentage of total flux actually affecting the solar cells.

The main concern is the amount of flux over an experimentally established flux rate that affects the solar cells.

The solar cells are to be shielded with 30-mil sapphire or 45-mil quartz, which will so reduce the incident flux that only protons and electrons with energies greater than 10 mev and 500 kev, respectively, will penetrate to the solar cell. Using the 10-mev contour in Figure 5-1 and the 500-kev contour in Figure 5-2 and dividing by three (assuming equatorial flux is approximately equal to three times polar flux), the flux rate versus altitude for protons and electrons in a polar orbit was obtained.

Using thinner shielding (such as 6-mil sapphire) for weight reduction (to be discussed later) the omnidirectional flux for 4-mev protons and 200-kev electrons would be reduced by a factor of 2. The structural backing remains the same, shielding  $E_p < 20$  mev, and only the solar cell side will "see" the  $E_p > 4$  mev.

The results presented in this report are based on the assumption that the flux is nearly omnidirectional. This assumption is considered in light of the following reasons:

- 1) The structural panels on which solar cell modules are mounted are thin honeycomb that receives radiation from all directions.
- 2) Secondary radiation, 40 percent of which are neutrons, is present from the supporting structure due to high-energy impacts ( $E_p > 400$  mev).
- 3) Outside neutron flux and gamma rays have not been accounted for in the computation of the solar cell degradation, in addition to the optical darkening of the shield due to soft particles.

This assumption may introduce a degree of pessimism into the degradation results.

Further consideration of the structural environment of the mounted solar cells producing possible differences in shielding capability indicates pessimistic results. The support structure (honeycomb) constitutes a shielding capability of  $0.45 \text{ gm-cm}^{-2}$  which for the honeycomb material absorbs protons  $E < 19$  mev as compared to the sapphire coating on solar cells that absorbs protons  $E < 10$  mev. The difference in flux due to this is a factor of 2.5.

In addition, the radiation dose to "edge-on" with respect to solar cells is not effective. The reduction due to this is about a factor of  $1/8$ . This makes the final flux two-thirds of the assumed value or about 30 percent less. Even with as large a discrepancy as this, the difference in the

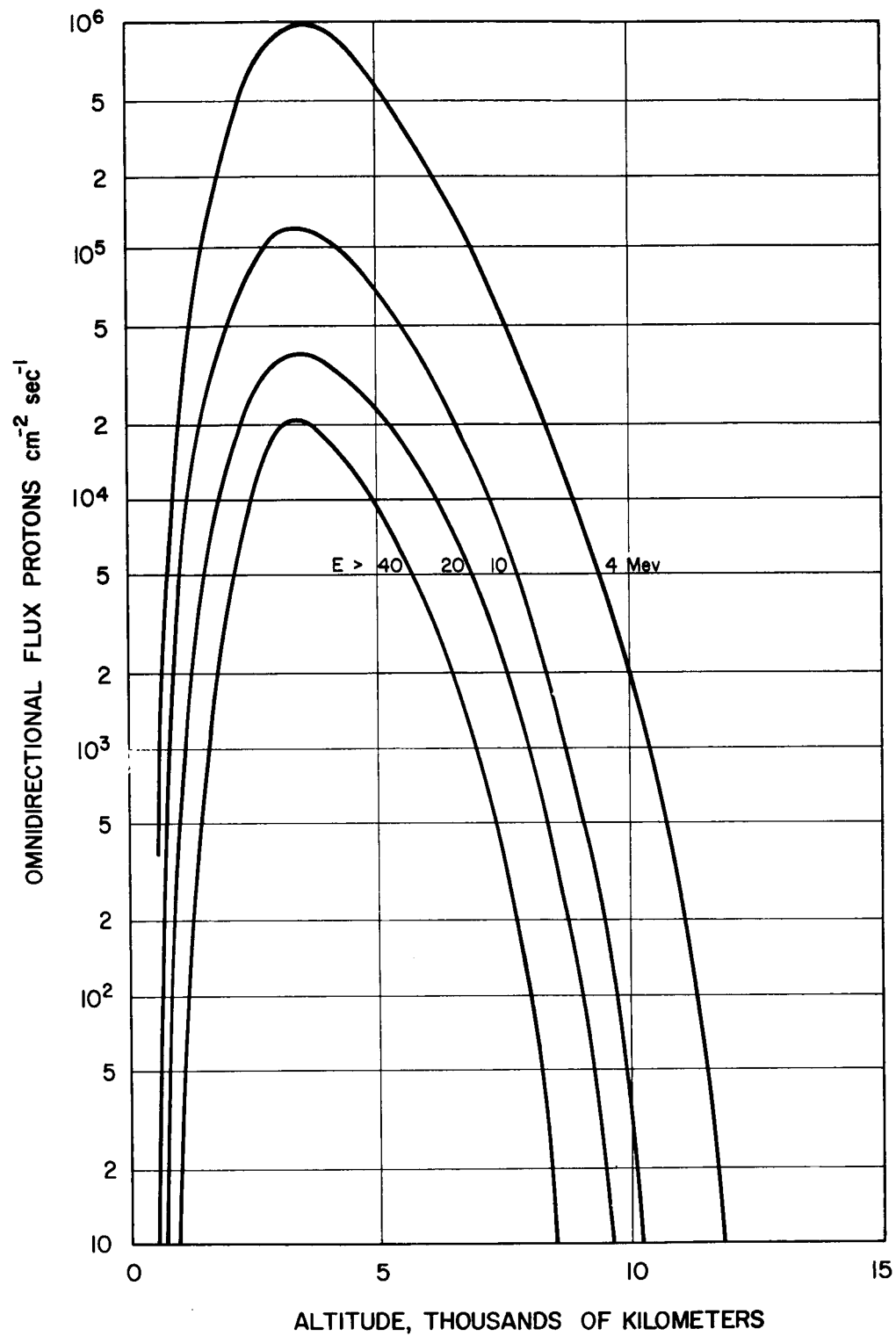


Figure 5-1. Proton Flux Spectrum of Radiation Belt



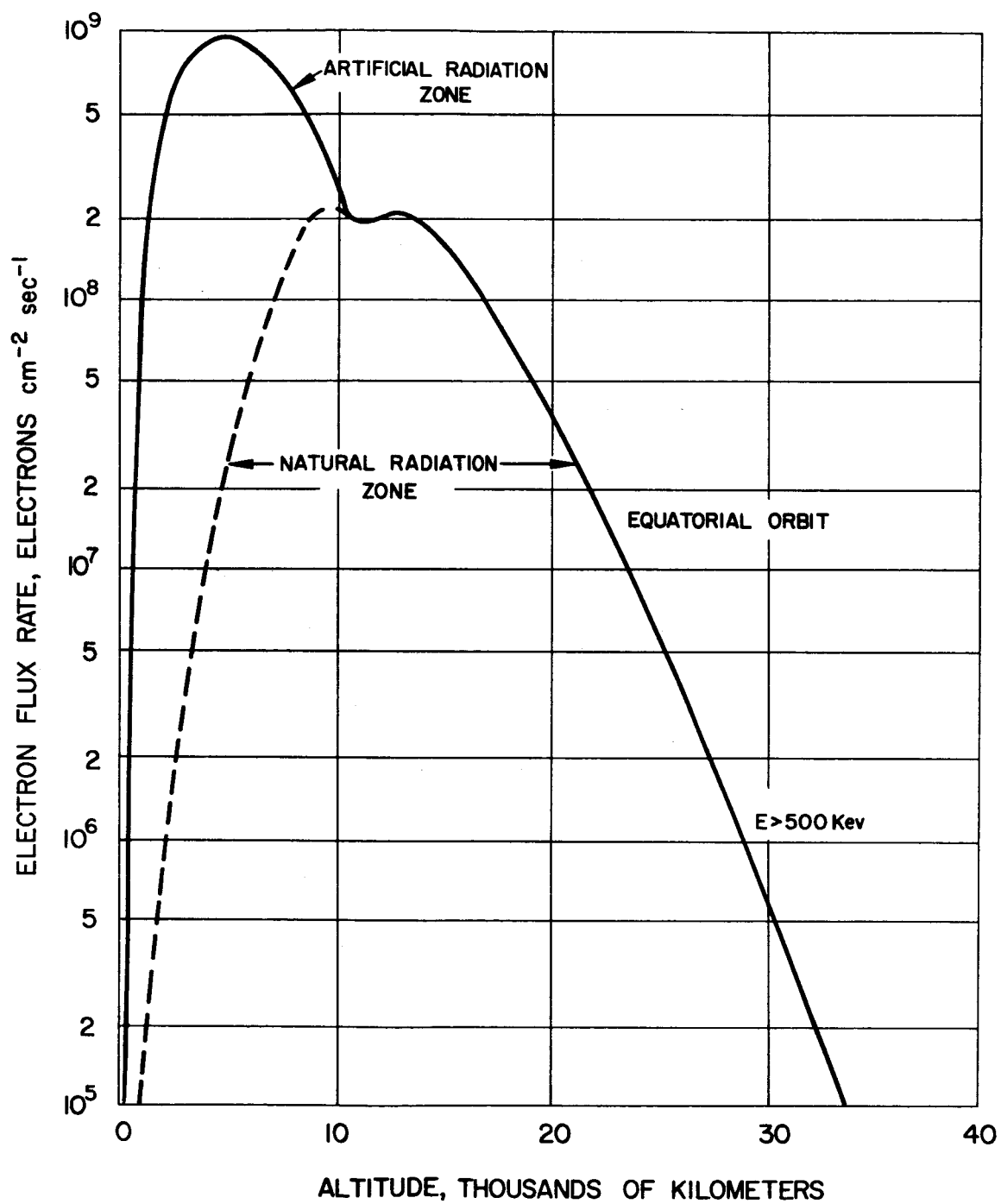


Figure 5-2. Electron Flux Spectrum of Radiation Belt

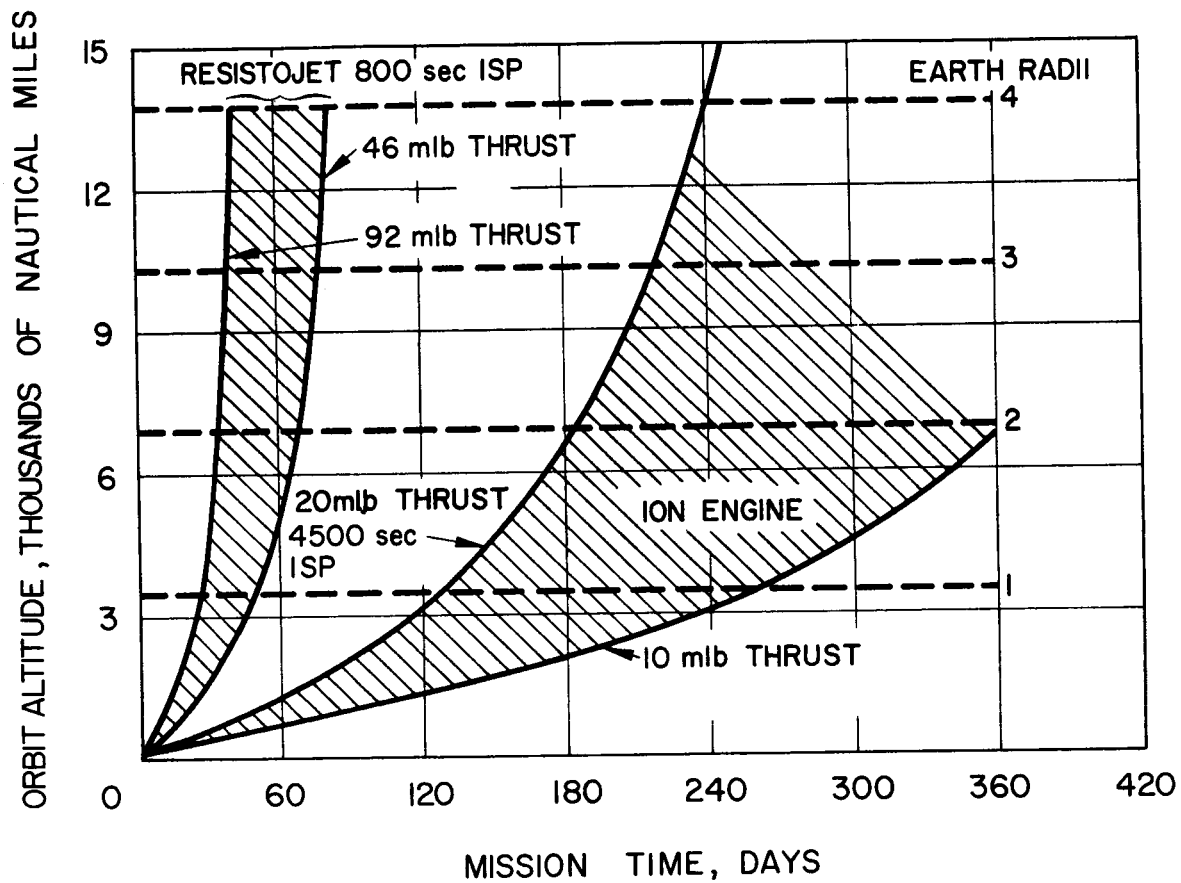


Figure 5-3. Typical Solar-Electric Propelled Spacecraft Mission Time Histories

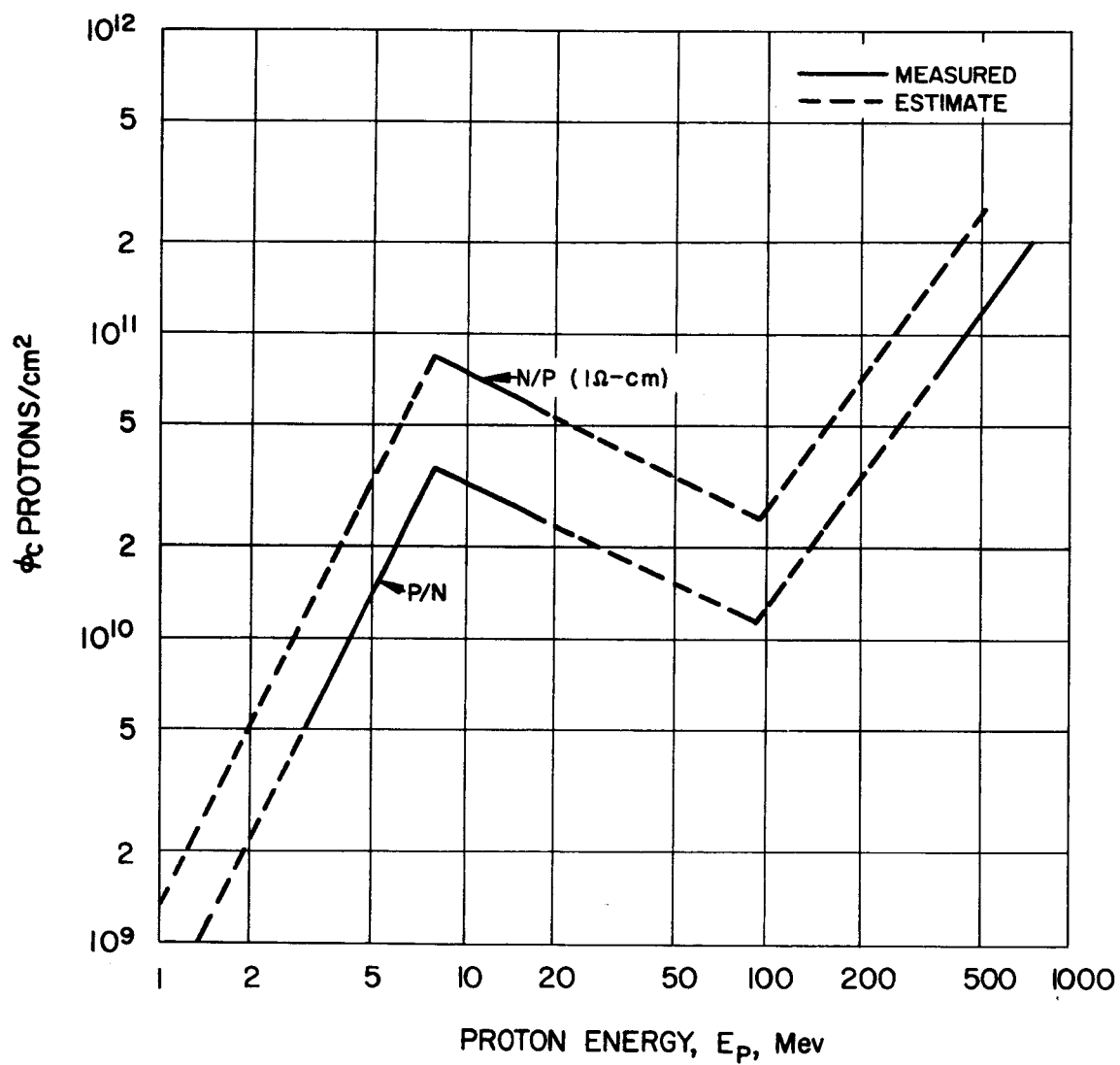


Figure 5-4. Variation of  $\theta_c$  with Proton Monoenergetic Particle Fluxes

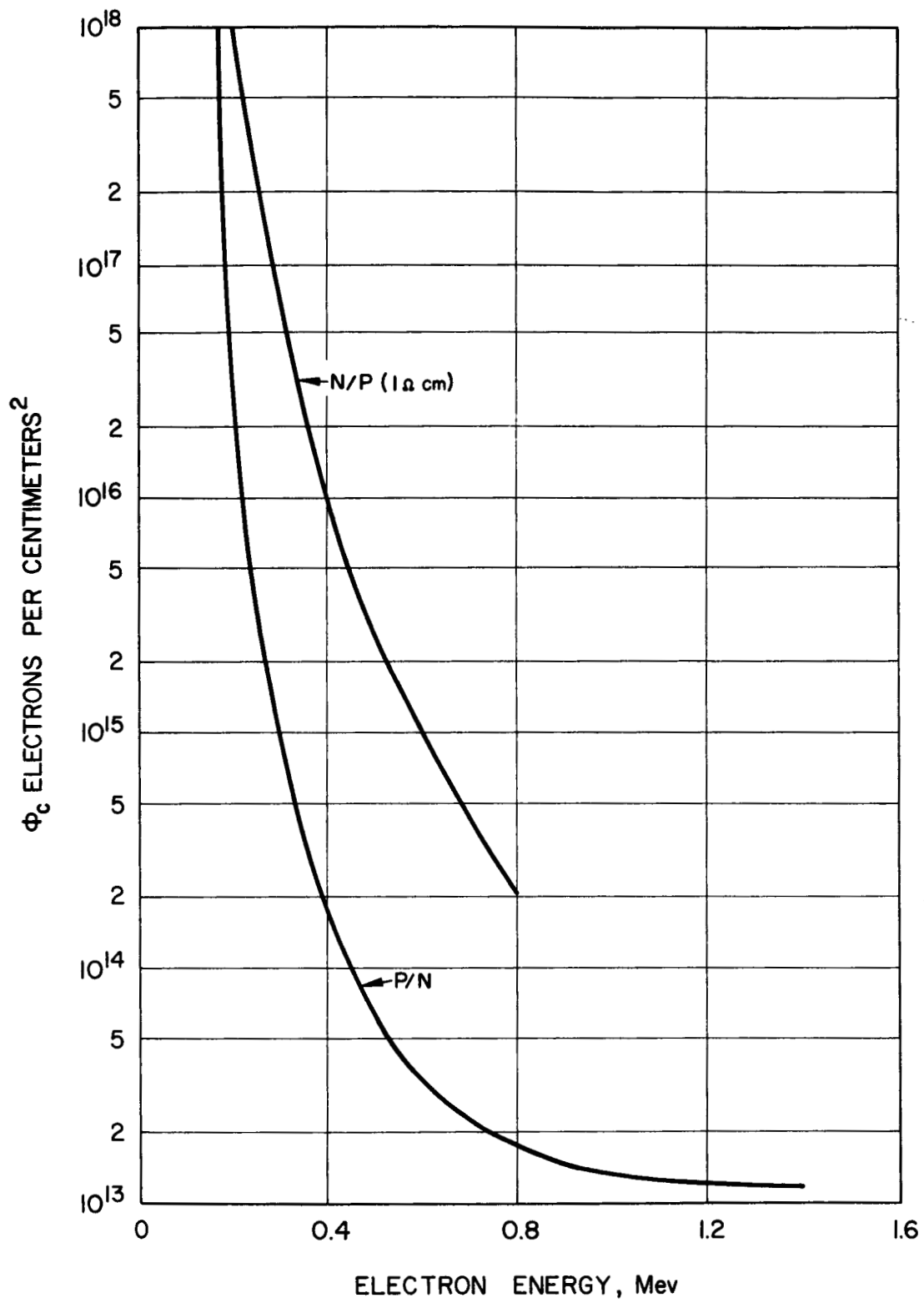


Figure 5-5. Variation of  $\theta_c$  with Electron Monoenergetic Particle Fluxes

degradation of the solar cells at the end of the mission is about 5 percent. It is possible that the secondary radiation effects not considered could make up this difference. Experimental measurements would be required to determine the accuracy of the degradation results.

The uncertainty in  $\phi_c$  can contribute as much as  $\pm 10$  percent degradation increment at the end of the mission depending on the type of solar cell selected.

Using the expression for decrease in solar cell output, the nomograph shown in Figure 5-6 was obtained. The nomograph covers the ranges of  $\phi_c$  for electrons, protons, and, if needed, neutrons and gamma rays. It also covers the expected total dose that impinges on the solar cells. By selecting the proper value of  $\phi_c$  and the estimated total dose and connecting with a straight line, the reduction in solar cell output can be read directly from the middle line.

Total particle radiation doses are shown in Figure 5-7 for the protons and in Figure 5-8 for the electrons corresponding to the four basic missions selected and as a function of altitude. Figure 5-8 includes the total electron dose for the contribution of the artificial radiation zone created 4 July 1962 by a high-altitude nuclear explosion. The determinations of the solar cell damage and subsequent necessary solar panel area are based on the following additional assumptions:

- 1) Range of resistivity is a factor determining the  $\phi_c$ .
- 2) Range of initial efficiency is 6 to 9.6 percent.
- 3) Proton and electron flux is as shown in Figures 5-1 and 5-2.

Putting all the assumptions together along with the uncertainties, considering the fluxes shown in Figures 5-1 and 5-2, and considering the total doses shown in Figures 5-7 and 5-8, the solar cell degradation for each of the selected missions is shown in Figure 5-9. These results include the percentage degradation due to protons and electrons by combining as an rms value. This, then, is converted back into the percentage of the initial output by subtracting from 100.

Recent data and calculations on the lifetime of the radiation zone created by the 9 July 1962 high-altitude nuclear blast show that the zone, or a portion of it, will remain for as long as 10 years. The amount of added electron flux is shown in Figure 5-2. As time increases, the electron flux decreases and moves to higher altitudes.

Results of considering the added electron flux are shown in Figure 5-10. A comparison is made between the degradation curves for the natural

radiation zone (seen in Figures 5-6 and 5-7) and the artificial radiation zone. The additional degradation is about 5 to 10 percent. This has about the same effect as increasing the proton dose by a factor of 2.

### Solar Flare Damage

At the present time solar flare activity is at a minimum, at least observably. Continual activity exists in the sun and its atmosphere, most of which adds to the noisy background of solar emission. From this quiet period to about 1967 or 1968, there will be a gradual increase in solar flare activity (associated with the sunspot cycle). The previous maximum was in 1957, during which several hundred flares of greater magnitude than importance "1" and several decades of importance "2" flares were observed. As a rule, flares of importance "2" or greater provide the greatest influx of solar protons. Importance "1" flares cannot be overlooked as a proton source since some of the largest surges have been associated with importance "1" flares.\*

Experimental data from INJUN I (Reference 17) and the Explorer - series probes indicate an increase of at least 100 times in the proton flux ( $4.8 < L < 6.1$ ) for most kinetic energy levels from importance "2" flares. Assuming that this is a valid number, the increment of dose over an average of 3 days during the passing of the plasma cloud or tongue is about 10 percent of the total dose shown in Figure 5-7. If at least 50 importance "2" flares occur over a period of 1 year, the accumulated dose would be increased by a factor of 5. This increases the solar cell degradation by less than 10 percent.

Some flares produce less proton flux while others produce greater proton flux. Relativistic flares produce large fluxes (up to  $10^{13}$  particles  $\text{cm}^{-2} \text{sec}^{-1}$ ) of high energy ( $E > 600 \text{ mev}$ ) particles that could conceivably cause complete destruction. Fortunately their occurrence is rare; the frequency has been predicted at one every 4 years.

### Micrometeorite Damage

If glass coverslides of approximately 0.10-cm thickness are added to the solar cells, damage to the silicon solar cells by micrometeorite penetration would be insignificant in a 1-year period, using most of the penetration equations presently in use (References 18 and 19). The one major problem here, aside from lack of information concerning hypervelocity particle bombardment on glass, is optical erosion. Whipple's technique and his estimate of 1000 tons per day of erosive meteorite material reaching the earth

---

\*Private communications with Lockheed Solar Observatory staff.

indicate the optical erosion will not be appreciable in less than a year's time.

At the present time, there is little justification for any of the estimates given on micrometeorite damage to solar cells. The need for more space experiments or laboratory equipment to better simulate the space environment is apparent. However, no evidence at this time indicates the need for precautionary measures to prevent micrometeorite damage to solar cells for a 1-year period in space.

### Solar Panel Design

Development and test of solar cell power systems for space application has been under way at Hughes for a number of years on such as the Hughes NASA Surveyor and Syncom. Solar power instrument calibration has been verified at the Table Mountain, California, test facility in cooperation with Jet Propulsion Laboratory, Applied Physics Laboratory (Johns-Hopkins University), Space Technology Laboratories, and others. The validity of the design concepts established at Hughes was demonstrated in the recent NASA-Hughes Syncom flight test as shown in Figure 5-11. This figure shows solar panel design performance along with data points taken at Table Mountain and in space. The Y-1 tests were made before and after the spacecraft qualification test program. The F-1 test data were taken during a 6-hour period in orbit.

Assuming a solar panel area utilization of 90 percent and employing 9.6 percent space efficiency solar cells, it is reasonable to expect as initial solar panel power capability  $10.4 \text{ w/ft}^2$  of panel area. It is estimated the solar panel will weigh  $1.2 \text{ lb/ft}^2$ . This is a 20 percent increase in weight over the Surveyor solar panel; the increase is due primarily to the heavier solar cell coverglass used. An increase in panel substrate weight per unit area is also anticipated in order to provide additional structural integrity to the folding panel. At  $1.2 \text{ lb/ft}^2$ , the panel will provide  $8.7 \text{ w/lb}$  initially.

Figures 5-12 and 5-13 illustrate the change in power per unit weight and per unit area as a function of the mission for the four engines shown. Figures 5-12 and 5-13 are based on the data shown in Figure 5-9 for the  $\phi_c$  values of  $5.8 \times 10^{10} \text{ particles cm}^{-2} \text{ sec}^{-1}$  (protons).

Using more optimistic critical flux values, conceivably a factor of 10 or higher, would greatly improve the output of the degraded solar cells and reduce the required solar panel area. A factor of 10 in the value of  $\phi_c$  would reduce the final degradation by a decrement of 20 percent.

## Battery Power Systems

The most familiar and readily available energy storage device is the battery, which converts chemical to electrical energy directly. Batteries have been developed over many years to offer:

- 1) High-power delivery for short periods of time.
- 2) Operation at varying rates of power output.
- 3) High reliability.
- 4) Low cost.
- 5) Minimum maintenance.
- 6) Operation under adverse conditions of vibration, temperature, etc.

As a power source, some of the disadvantages are:

- 1) High weight if long-term operation is required.
- 2) Short operating life if an external power source (solar converter) is not used.
- 3) Relatively short shelf life for secondary-type batteries.

Batteries have found extensive use in missile, satellite, and space systems. For example, silver-oxide-zinc primary batteries are used extensively in ballistic missiles. Primary batteries of this type have a short life but are useful because of their long storage capability prior to activation. Secondary silver-oxide-zinc batteries offer the highest energy per unit weight but are cycle-life-limited. Sealed nickel-cadmium batteries are used extensively in satellites because of their long lifetime and ability to take many discharge-recharge cycles. Sealed silver-cadmium batteries fall in the range between silver-cadmium and silver-zinc in terms of both specific energy and cycle life and have recently been used in satellite missions.

Figure 5-14 shows the estimated cycle life of nickel-cadmium, silver-cadmium, and silver-zinc secondary batteries as a function of depth of discharge. Data plotted in the figure are based on tests conducted by the Cook Electric Company and represent some of the most recent achievements in the industry. The trend lines drawn in the curves a, b, and c show explicitly the difference in performance of the three types of energy storage systems presently in use.



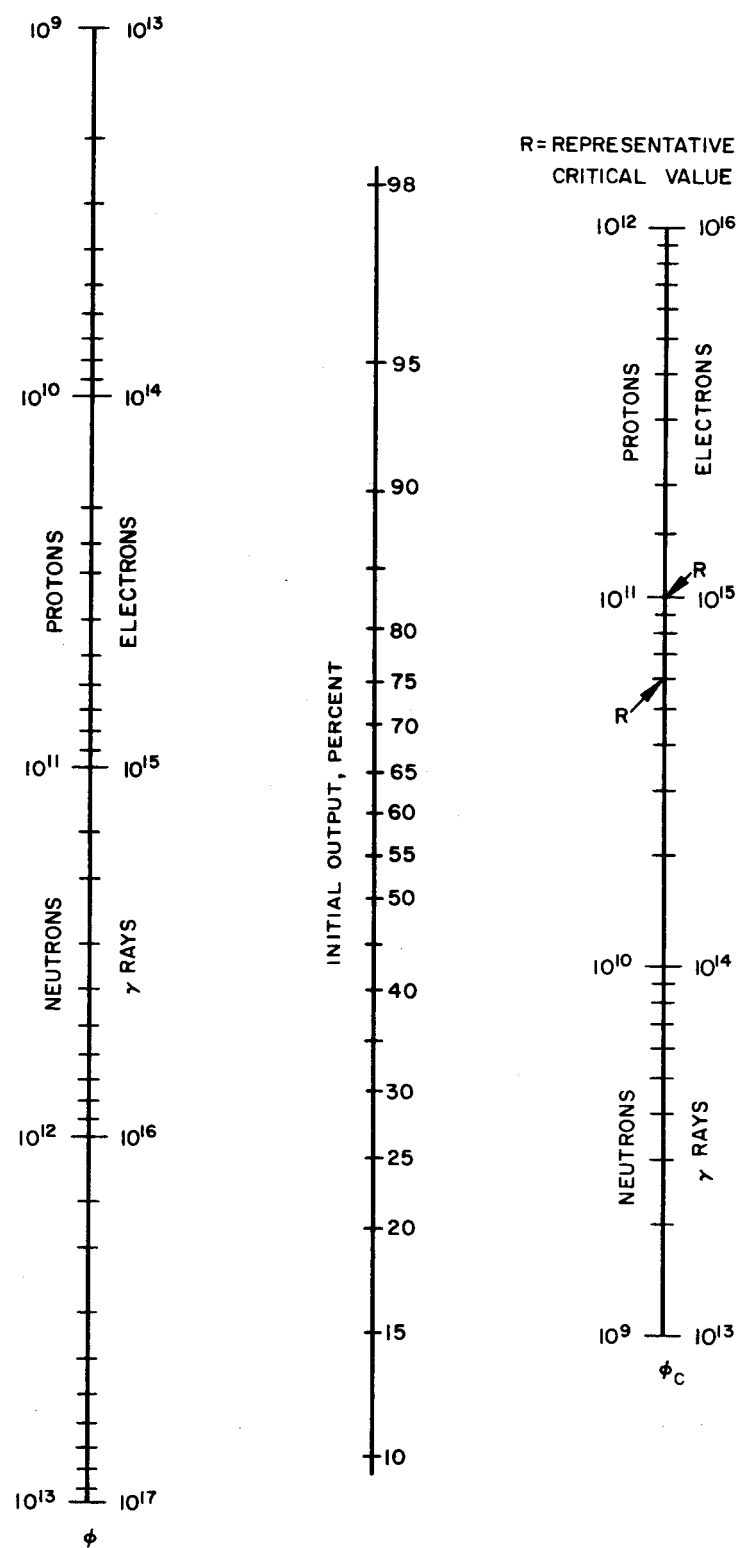


Figure 5-6. Nomograph for Determination of Solar Cell Output Degradation

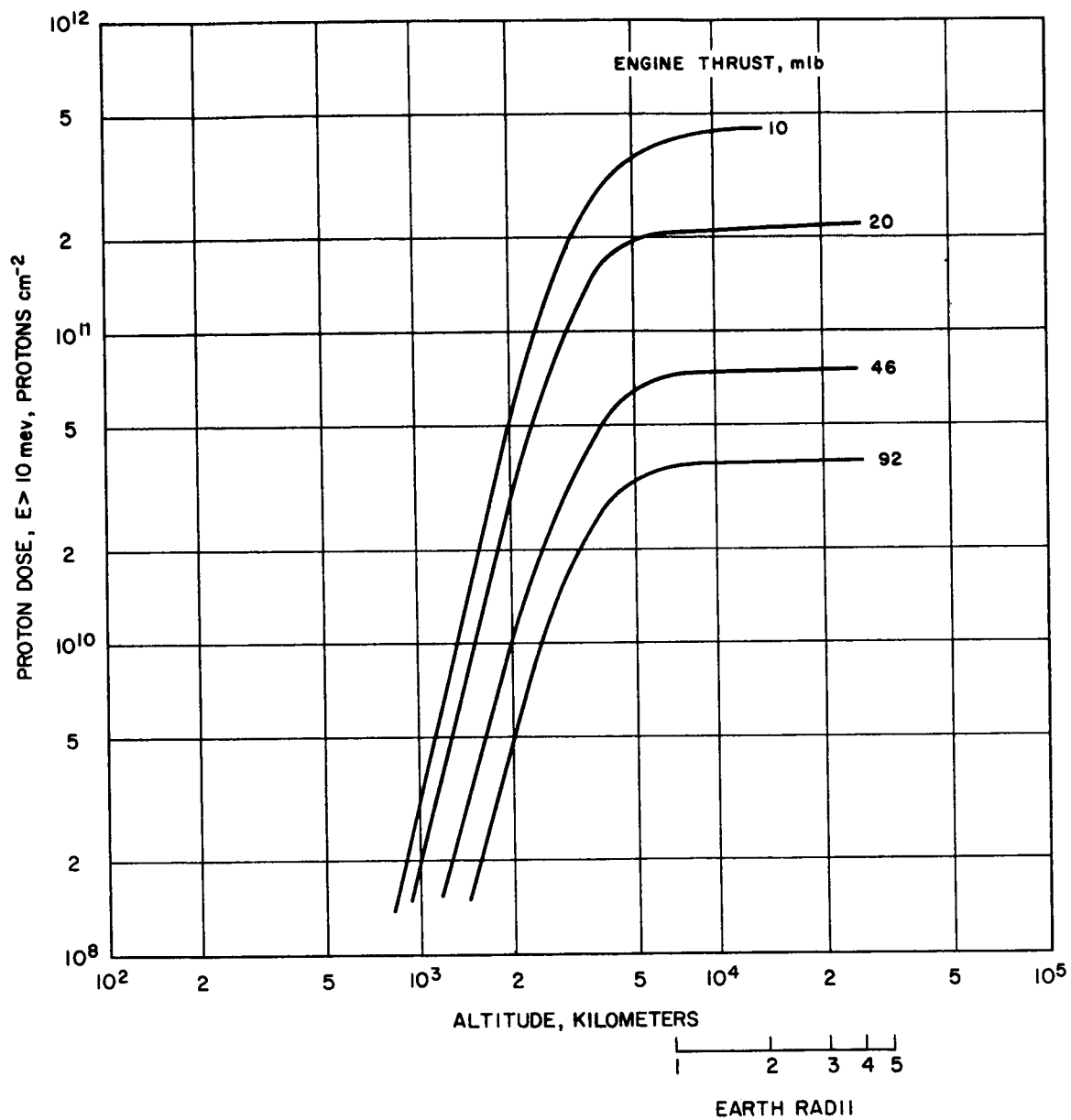


Figure 5-7. Total Proton Dose for Selected Mission  
Natural Particle Energy Spectrum

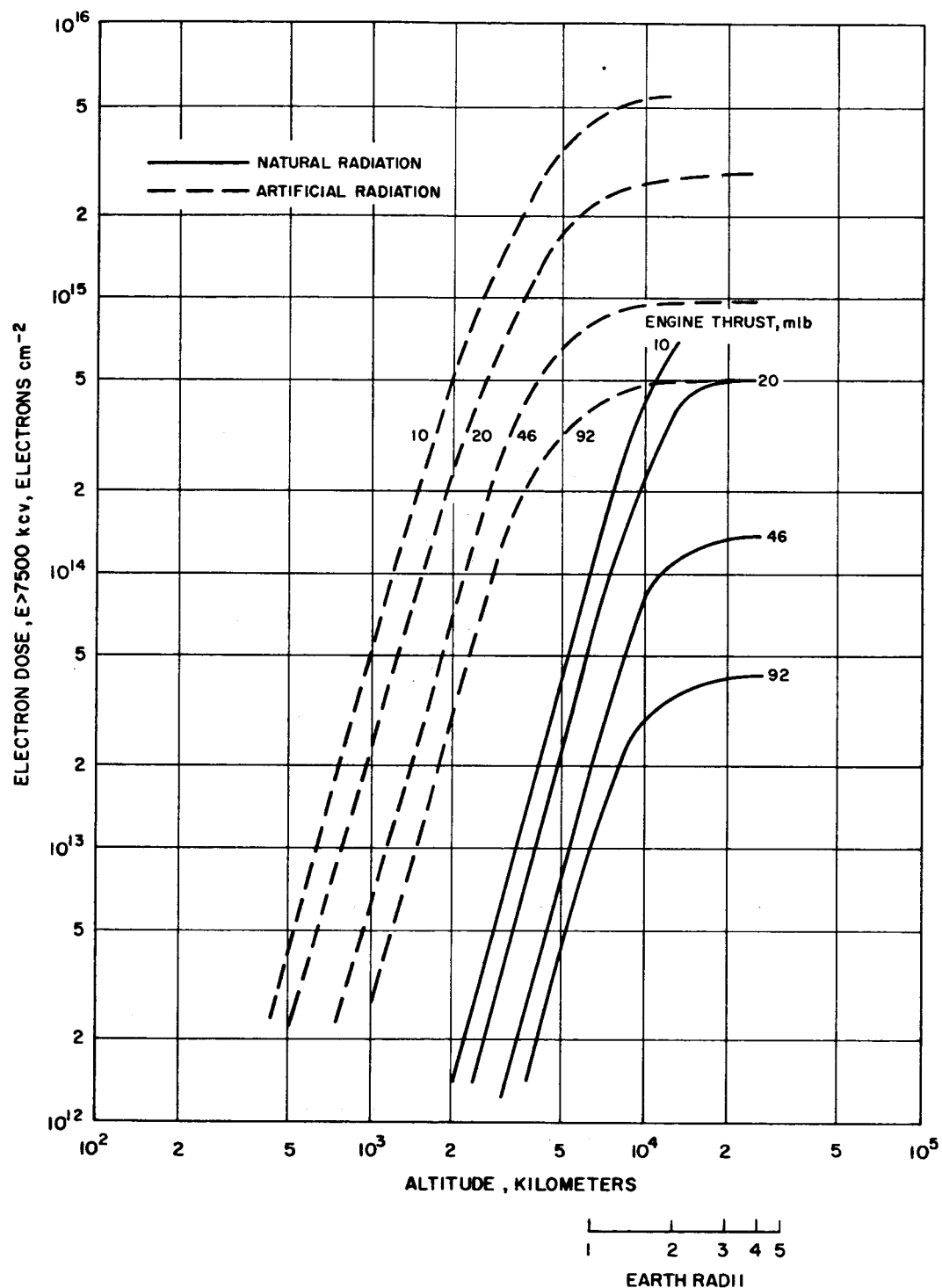


Figure 5-8. Total Electron Dose for Selected Mission  
Both Natural and Artificial Energy Spectrum from  
High Altitude Nuclear Detonation on 4 July 1962

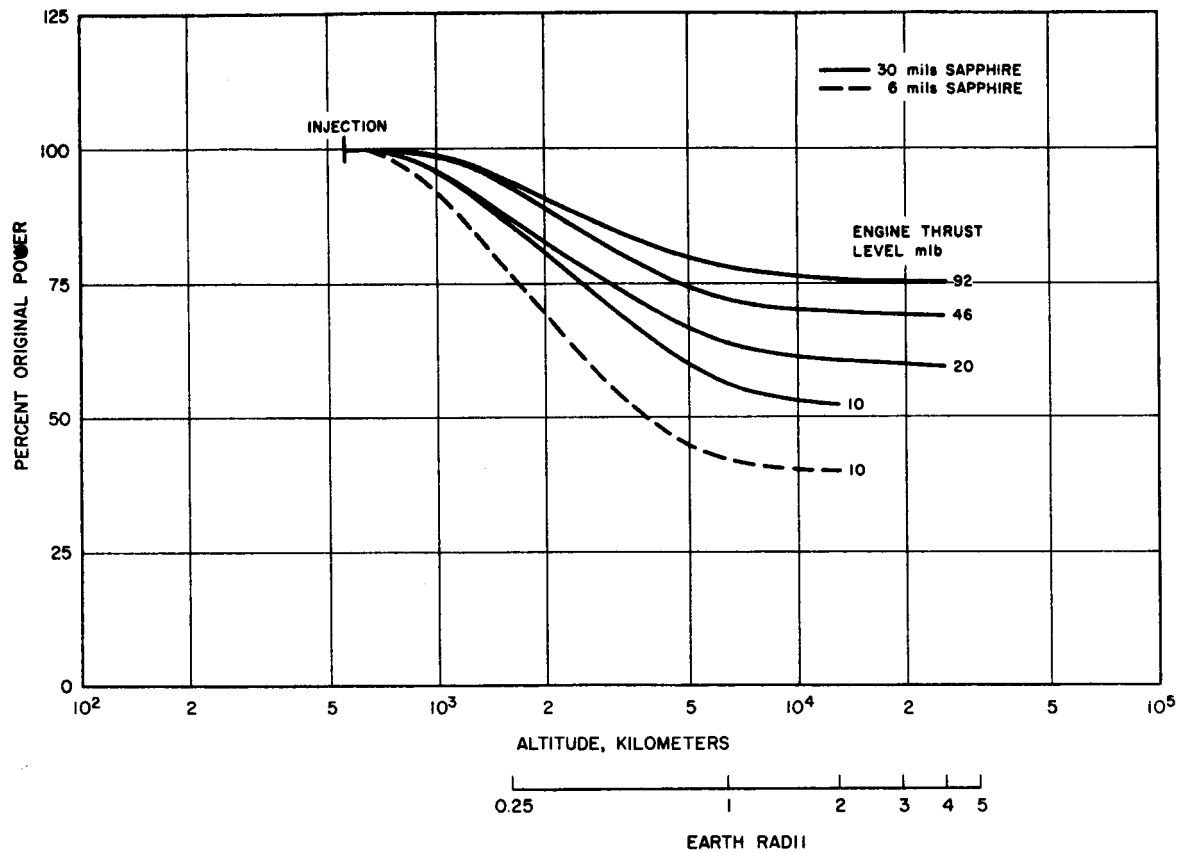


Figure 5-9. Solar Cell Degradation for Electric Engine Spacecraft as a Function of Mission Time

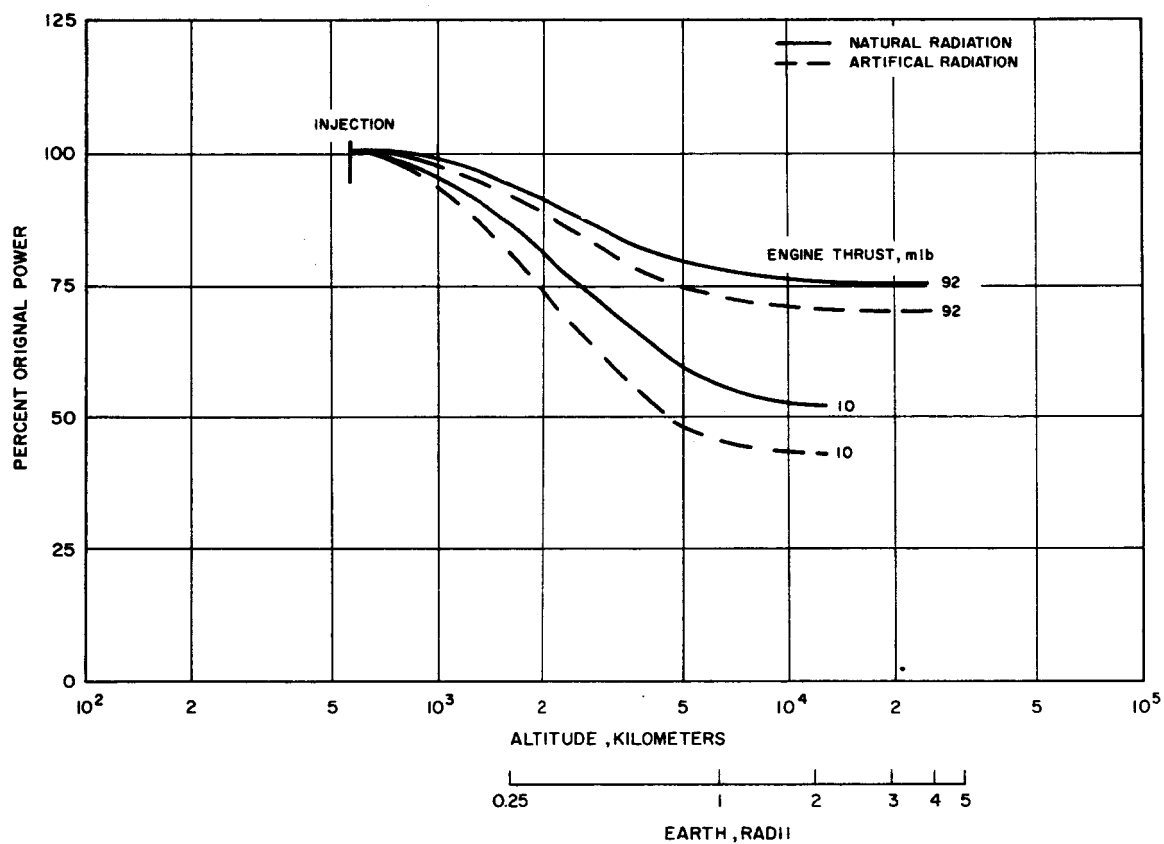


Figure 5-10. Comparison of Solar Cell Degradation from Natural Radiation Belt with That from Natural plus Artificial Radiations

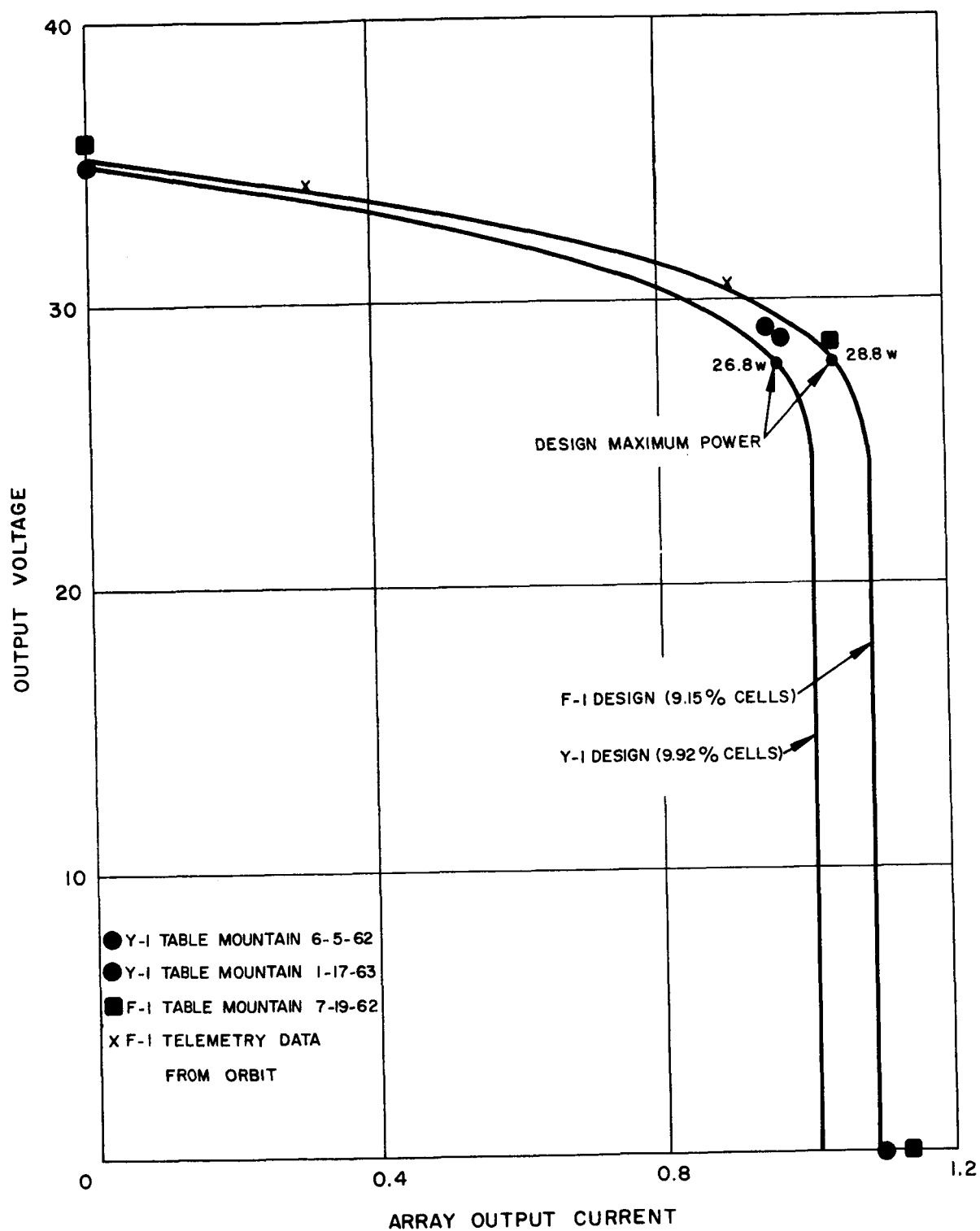


Figure 5-11. Hughes Solar Panel Design Performance

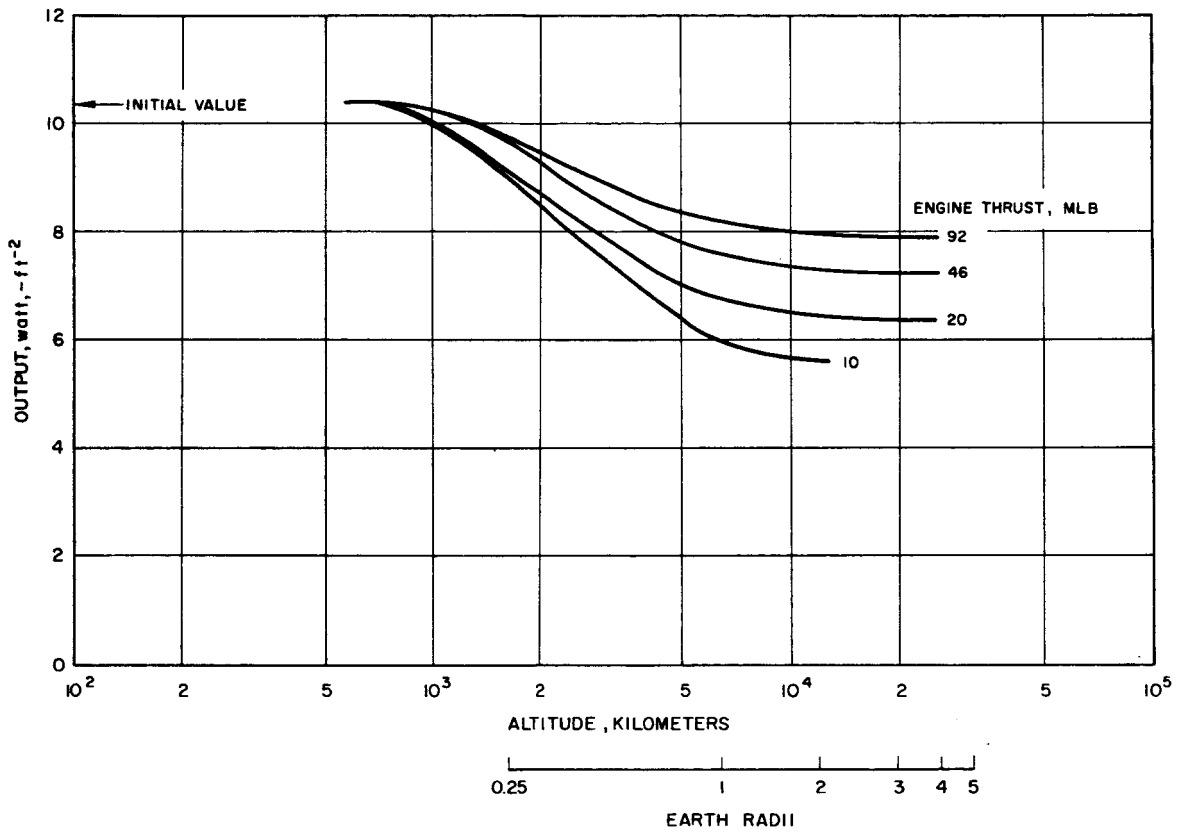


Figure 5-12. Solar Array Output per Unit Area for Polar Orbit Transfer Missions

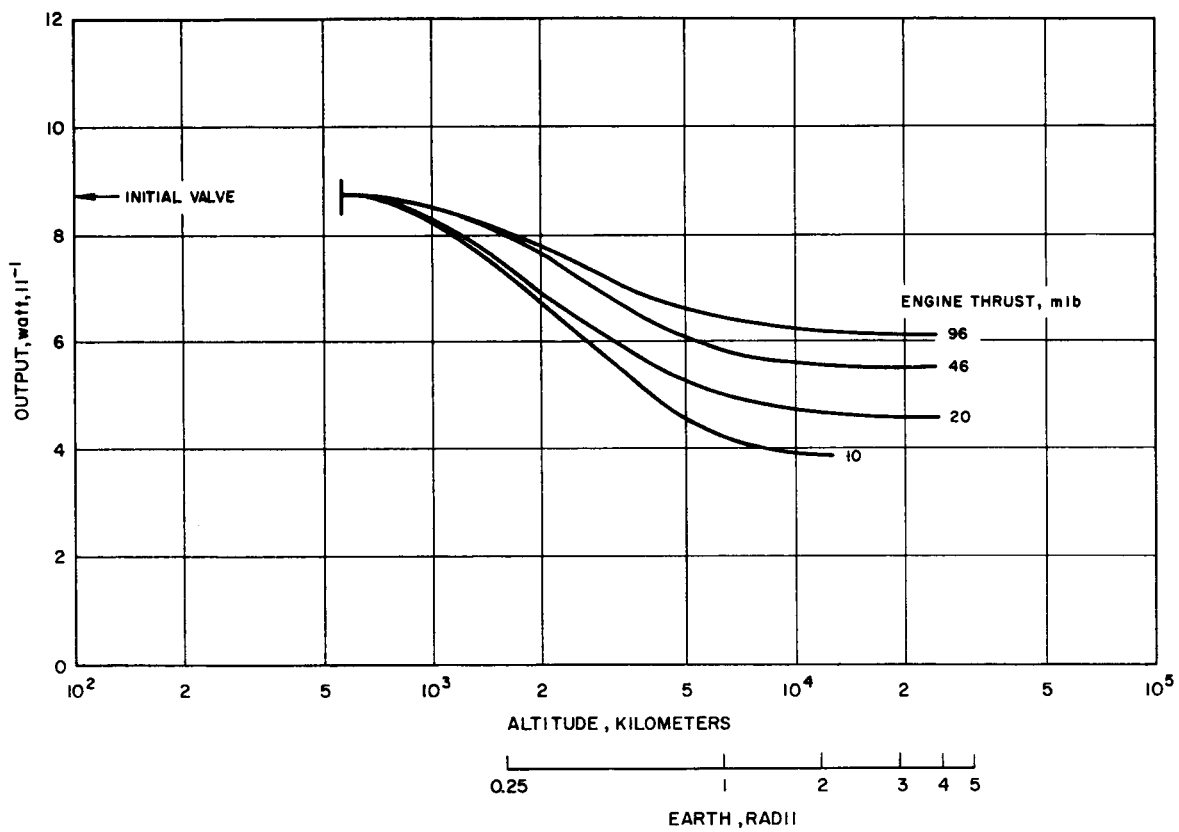


Figure 5-13. Solar Array Output per Unit Weight for Polar Orbit Transfer Missions



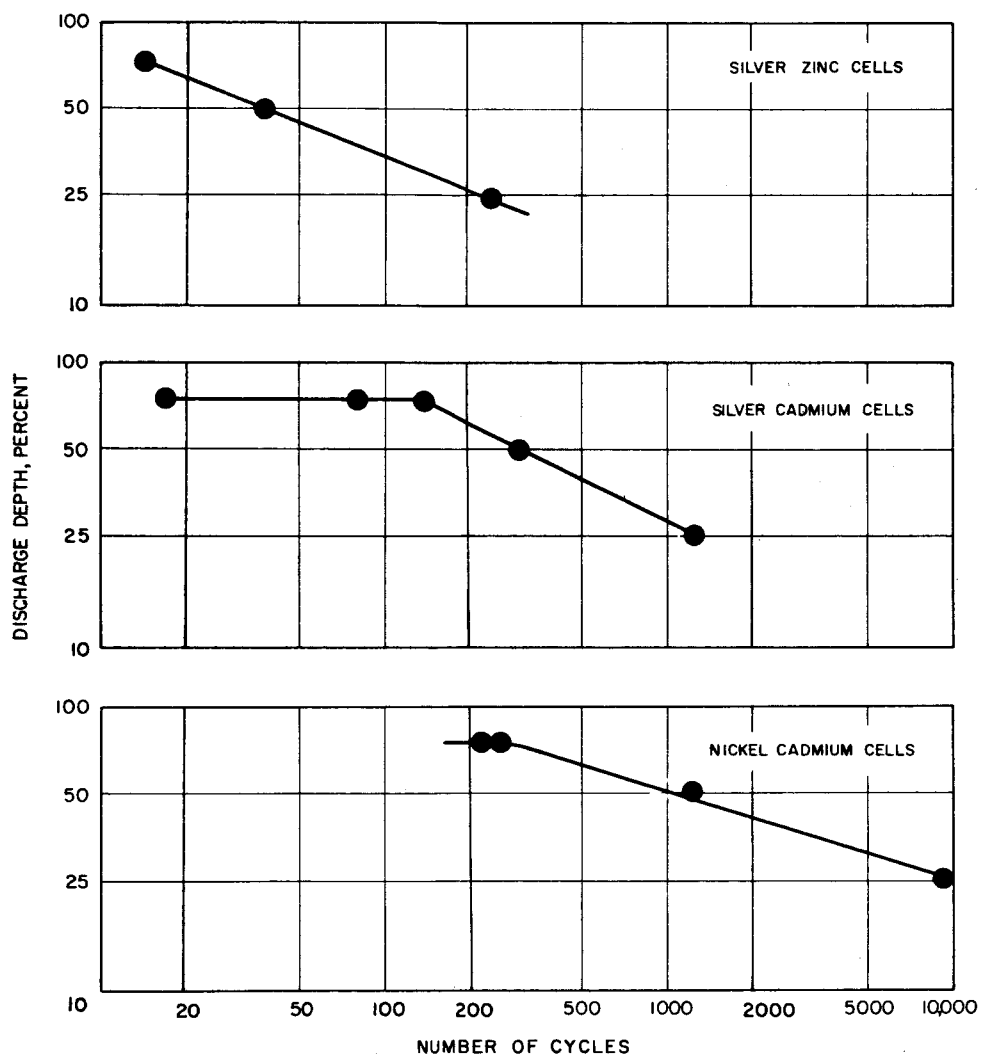


Figure 5-14. Estimated Cycle Life Prior to Failure for Secondary Batteries at 70°F

The nickel-cadmium, and more recently the silver-cadmium, batteries have been used in earth-orbiting space missions requiring a large number of charge-discharge cycles. The silver-zinc battery has been limited to use in lunar and interplanetary missions which require a high energy density (watt-hours per pound) and are subject to only a few charge-discharge cycles.

In Figure 5-15 the specific energy of the three types of batteries is shown as a function of discharge rate. The graph is plotted for the capacities obtained when the batteries are subjected to a 100-percent depth of discharge at a temperature of  $70 \pm 10^\circ \text{ F}$  at rates varying from 0.2 to 100 hours. The trend lines are based on test and manufacturers' data that represent an average of the true test points.

### Power Conditioning

Electronic and propulsion system power demands can rarely be met by simple solar cell/battery combinations. In many cases some form of power conditioning is required to transform the primary power system voltages and currents to voltage levels, currents, impedances, and ripple content suitable for use by the various power consumers. Electronic systems generally require a number of regulated voltage forms both positive and negative with respect to ships ground. Resisto-jet and arc-jet propulsion systems require only some form of current limiting while ion engine propulsion systems require power forms similar to electronic loads. The spacecraft must provide equipment capable of converting battery and solar cell power to forms acceptable to both the electronic and propulsion systems. Figure 5-16 shows block diagrams for two such systems.

The first system is a Hughes missile design. It is especially suited to systems which can tolerate a 2- to 5-percent voltage regulation of the major voltage forms and requires only a small amount of high-quality power. In this system transformer input is controlled to regulate all voltage levels. Fine voltage control can be provided at the output by means of dissipative regulation where required. This is potentially the lightest-weight system which can be built; however, any change in voltage or current level requires complete redesign of the transformer-rectifier package.

The second system shown is the present Sert 1 power system design. In this system, unregulated dc is converted to unregulated ac and then to regulated dc or ac as required by a number of ac-dc power supplies and ac line regulators. A change in voltage and current level of any particular voltage form will cause redesigns of only a small part of the total equipment package provided the total power required is unchanged. A larger number of magnetic components are used in this type of design and each must be capable of operating over a wide range of input voltages. This type of design is potentially heavier than the first system.

The weight and efficiency of either type of converter can be estimated by assigning a nominal efficiency and specific weight to each step in the power conversion. From past experience with Hughes fire control, missile, spacecraft, and the Sert 1 ion engine power supplies, it seems reasonable to assign 90-percent efficiency for switch-type operations such as dc-to-ac transformerless inverters, magnetic amplifiers, and silicon-controlled rectifiers. Transformer rectifier combinations for voltages over 30 volts can be made 95 percent efficient, but series-type dissipative regulator efficiency depends on operating voltage range. With preregulation, this efficiency can be held to about 90 percent. From Figure 5-16 then the use of preregulation will permit overall conversion efficiency of about 77 percent. The Sert 1 scheme will provide somewhat less efficiency for equal fractions of "fine" power.

Figure 5-17 shows the estimated weight of unregulated transformer rectifiers as a function of power output. The upper line is a design rule given in Reference 20. Two experimental points are shown at 1700 and 34,000 watts for Hughes fire control equipment constructed in the 1959-1960 time period. The dashed line shows the effect on component weight of operation at 2-kc frequency. Figure 5-18 shows representative weights for both dissipative and magnetic amplifier type regulated power supplies as a function of power output for a number of Hughes designs. For reference the two solid lines shown two and four times the WADD transformer rectifier weight. The very close agreement between these curves and the design values indicates that the transformer scaling law applies to other electronic components as well. This figure shows that 400-cps magnetic amplifier type power supplies are almost twice as heavy as comparable dissipative types. One reason for this is that not only is a magnetic amplifier often heavier than its associated transformer-rectifier, but the high ripple content of its output greatly increases the size of required filter chokes and capacitors. A complete dc-dc converter contains one transformer rectifier unit (often operating at 2-kc frequency or higher) and two switching units. The weight of a dc-dc converter can be estimated by adding the weight of the required 2-kc transformer rectifier to twice the weight of a single switching unit.

Figure 5-19 shows such a weight estimate for 2-kc dc-dc converters along with design points for Surveyor and Sert 1 equipment. The Sert 1 inverter weight is somewhat less than the estimated curve indicating the conservative nature of these extrapolations. The weight of a complete power system can be estimated by adding the predicted weight for each voltage form. The dashed line shows a weight estimate for an ion engine power system. Engine efficiency was assumed to be 50 percent and power split as follows: 50-percent beam, 30-percent ionizer, 10-percent electrodes, 5-percent feed system, 5-percent rest. This estimate agrees quite well with Sert 1 power system weight. The curved line shows the weight of dc-dc converters estimated by W. A. Manahan in Reference 21. It is also in agreement with other results.

### State of The Art

The introduction of new and better components can result in substantial reduction in the weight and size of power systems. Weight reduction is also possible without the introduction of new components. Figure 5-20 shows a chronological sequence of Hughes dc power supplies constructed during the 1950 to 1962 time period. The first three systems show the effect of a determined effort to reduce weight with no change in the type of available components. The second three systems show the effects of additional effort applied to reduce weight during a period when silicon rectifiers were available. Weight was reduced substantially in this time interval. The last system shows the effect of introducing silicon transistors. This figure indicates the effectiveness of weight reduction programs. The same technique can be used to improve efficiency or any other unit parameter.

### Solar-Electric Power System Design Characteristics

The area of solar panel required to operate the Lewis ion engine and the resisto-jet engine for polar orbit missions is shown in Figure 5-21. The band on each parameter represents the spread on solar panel requirements for missions between 1 and 2 earth radii altitude. In Figure 5-22 the total power system weight associated with these missions is depicted. These weights and areas were computed from data described in the solar cell degradation and power conversion sections of this report and have been used in the conceptual designs presented here.

### Cryogenic Hydrogen Storage

Considerable variations in estimates of cryogenic hydrogen tankage weights are possible, depending on the assumptions used in the calculations. This is illustrated in Figure 5-23 which shows two sets of curves depicting the variation of tank weight with useful hydrogen weight for sub-critical pressure storage and constant use rates of 1, 2, and 5 pounds per day. These curves are based on data supplied by Beech and AiResearch. The lower set represents optimistic minimum weight designs without an outer shell, and requires prelaunch ground cooling operations. The upper set represents a more conservative approach using an outer shell and evacuated insulation space which simplifies the ground operations. Hence, the difference between the two sets of curves is due, in part, to the outer shell weight, and also to differences in the minimum thickness allowed for the inner shell and insulation.

Two design points are shown for tankage sufficient to allow a 1000-pound gross weight resisto-jet-propelled spacecraft to spiral up to an altitude of 1 earth radius. Two half-size tanks were used in the double-shell design because of space limitations. A cylindrical single-shell

design was used. The substantial weight saving which can be achieved by omitting the outer pressure vessel is apparent. A double-shell tank would weigh 180 pounds while a single-shell design would weigh only 43 pounds.

## MISSION SELECTION

A comparison of the payload capabilities of the family of solar-electric-propelled satellites studied with the payloads required for the NASA scientific unmanned satellites is shown in Figure 5-24. The curves shown are for spacecraft using various types of engines and various power levels.

Figure 5-24 reveals several distinctive differences between the mission capabilities of the electrothermal engine spacecraft and the electrostatic engine spacecraft. For comparable power levels, the electrostatic (ion) engine spacecraft have a greater payload capability, but require up to eight times the orbit transfer time. Also, because of the long orbit transfer times for the electrostatic engine spacecraft, and because of the spatial dynamics of the orbit plane, the satellite passes through the earth's shadow before it can reach an altitude sufficient to remain clear of the shadow. As a result, the ion engine systems shown (Configurations III and IV) are altitude limited.

The complete survey of the NASA missions examined for this study is presented in Tables 5-1 through 5-5. Most of the NASA missions are in fixed orbits except for the normal or abnormal perturbation on the satellite orbit. The solar-electric missions (also perturbed) gradually spiral outward to the maximum mission altitude obtaining data in concentric shells, the thickness of which is a function of the time to ascent to the mission altitude.

Selection of the mission or missions is based on the shortest time to mission altitude with the desirable value of payload. Referring to Figure 5-24a and b and considering the amount of payload of POGO and EGO, the most desirable selection for the solar-electric system is the resisto-jet with a 1.5-kilowatt power level. This particular spacecraft will raise the POGO or EGO payloads of 150 pounds to a mission altitude of about 2.0 earth radii in 43 days. Furthermore, this spacecraft has the capability of raising 258 pounds of payload to a mission altitude of 1 earth radius. The POGO and solar-electric satellites utilize the Thor-Agena B launch vehicle while the EGO spacecraft uses an Atlas-Agena B.

Of particular significance is the fact that all of the solar-electric satellite configurations considered are capable of carrying a POGO-class scientific payload up to at least 1 earth radius.

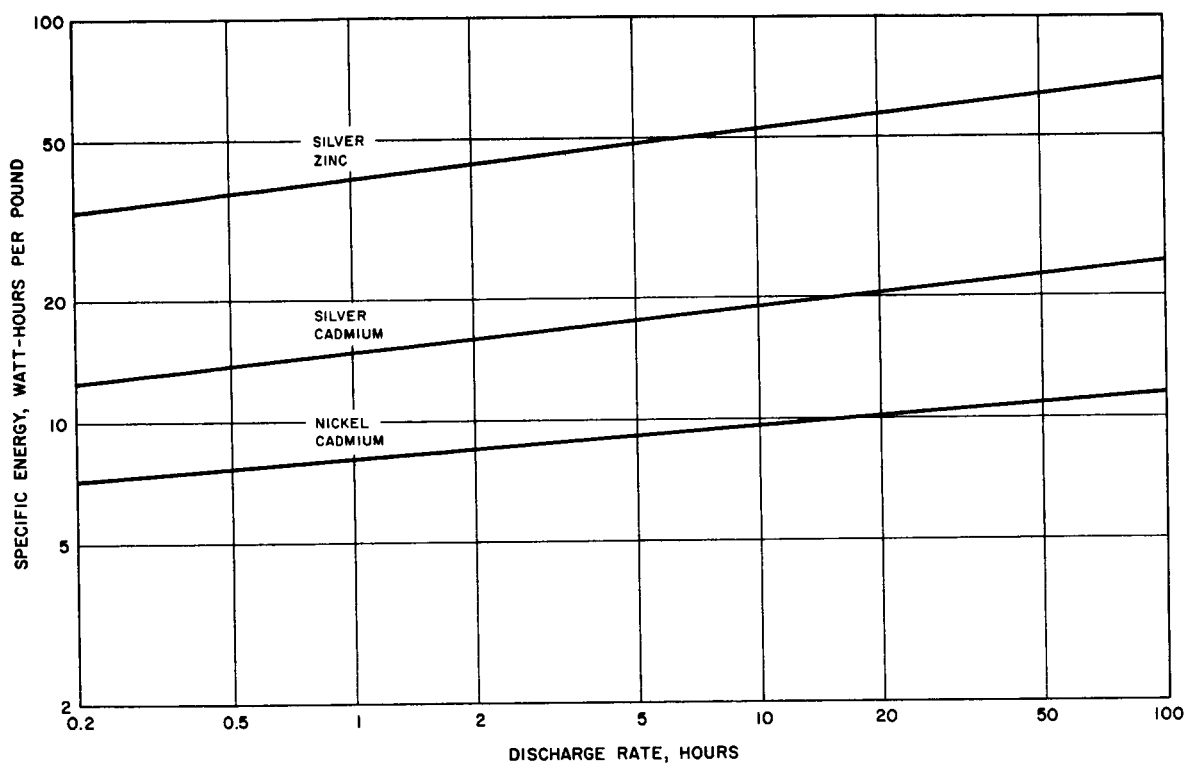
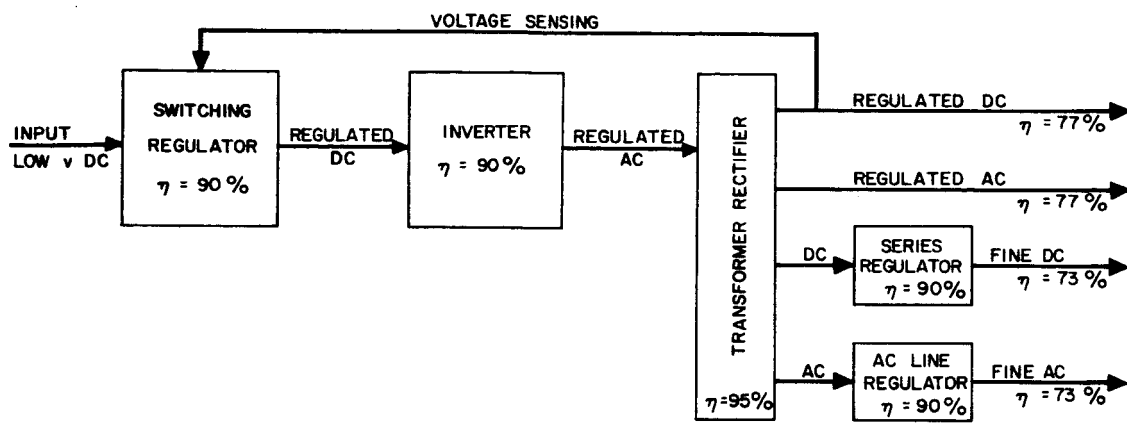
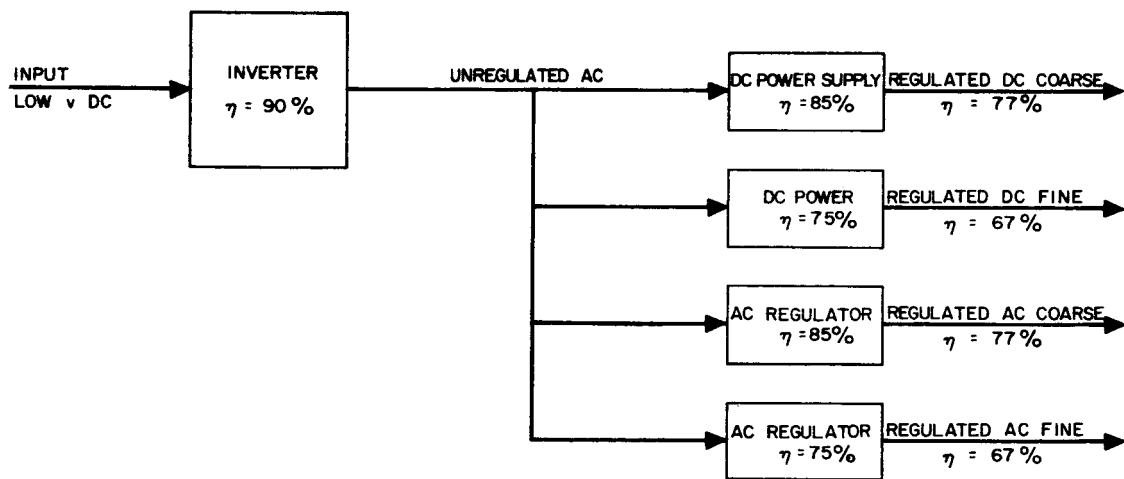


Figure 5-15. Specific Energy of Secondary Batteries



A) PRE REGULATION



B) POST REGULATION

Figure 5-16. Block Diagram of Power Conversion Systems for Ion Rocket Engine Systems

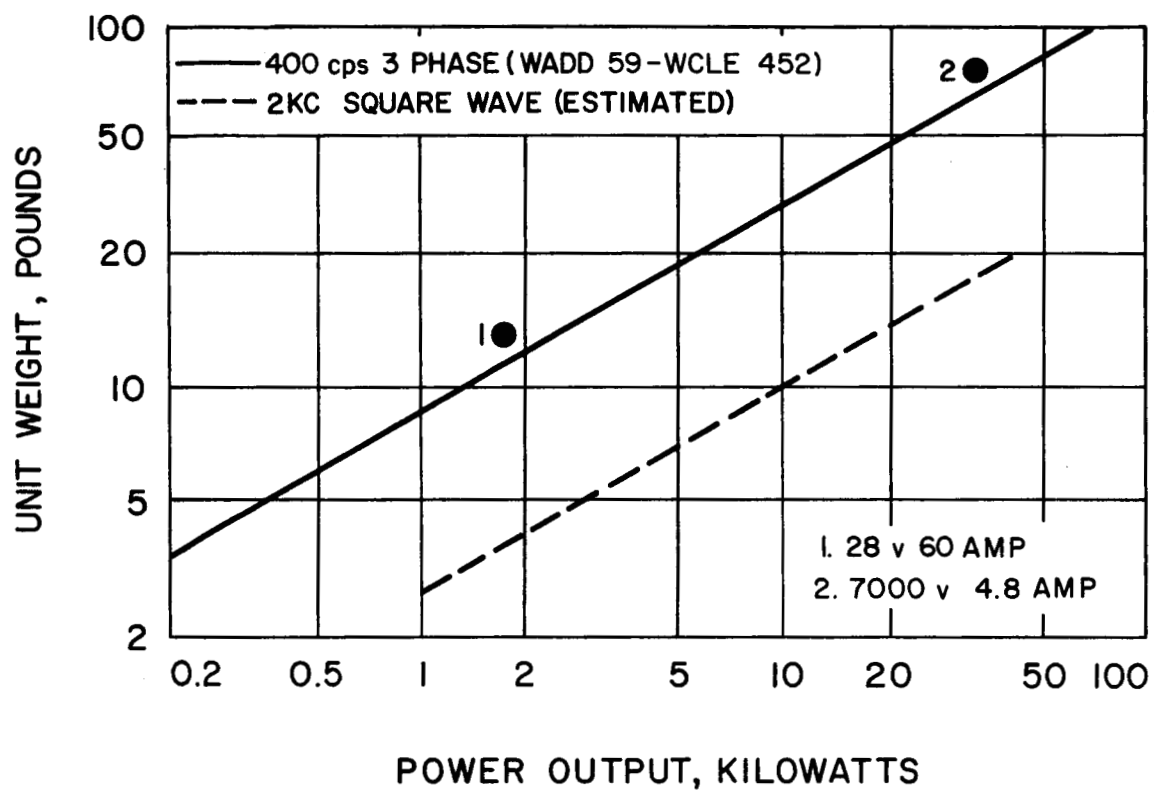


Figure 5-17. Estimated Weight of Unregulated Transformer Rectifiers as Function of Power Output



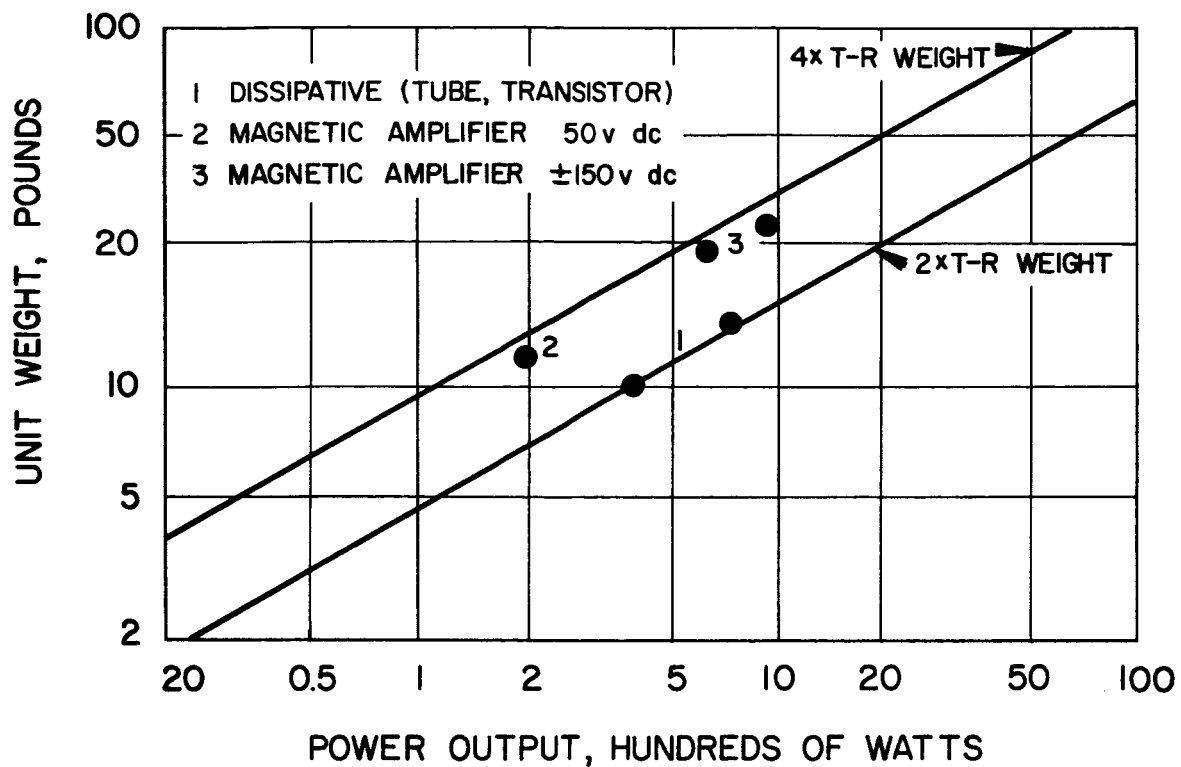


Figure 5-18. Representative Weights of Dissipative and Magnetic Type Regulated Power Supplies as Function of Power Output and Specific Hughes Designs

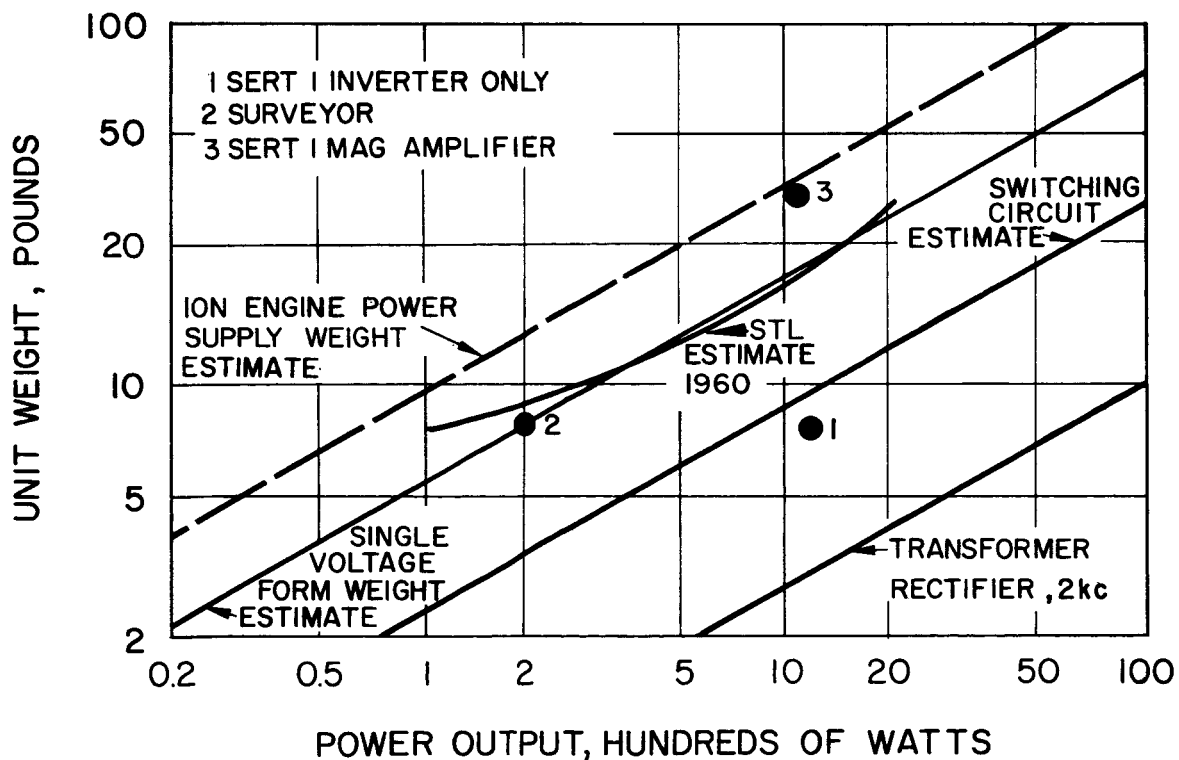


Figure 5-19. Weight Estimate for 2-kc dc-dc Converters as Function of Power Output

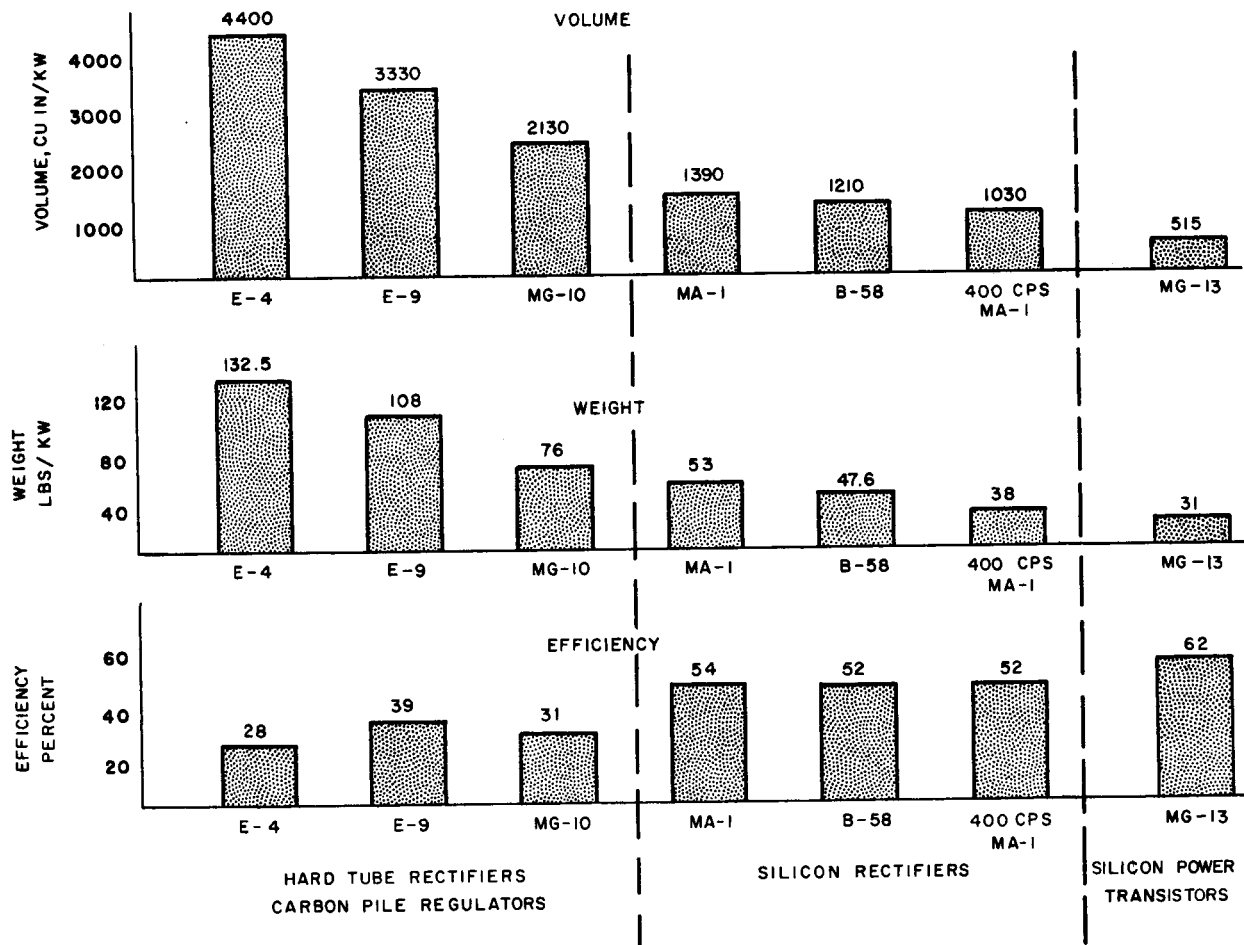


Figure 5-20. Chronological Sequence of Hughes dc Power Supplies Characteristics from 1950 to 1962

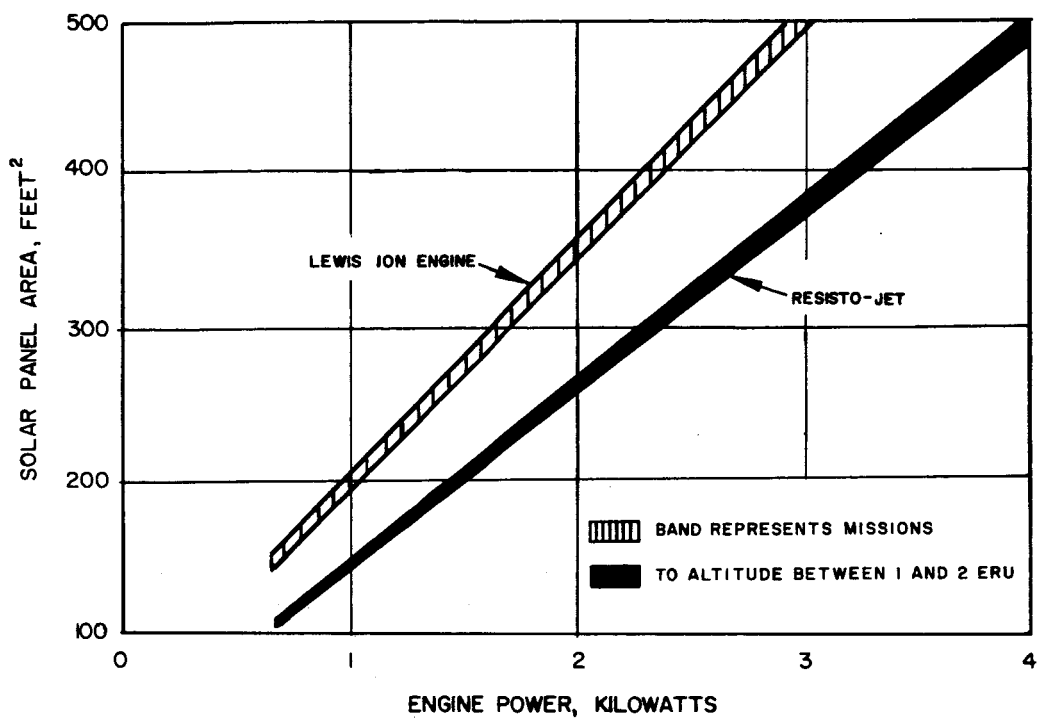


Figure 5-21. Variation of Solar Panel Area Required for Electric Engine Operation with Engine Power Requirements

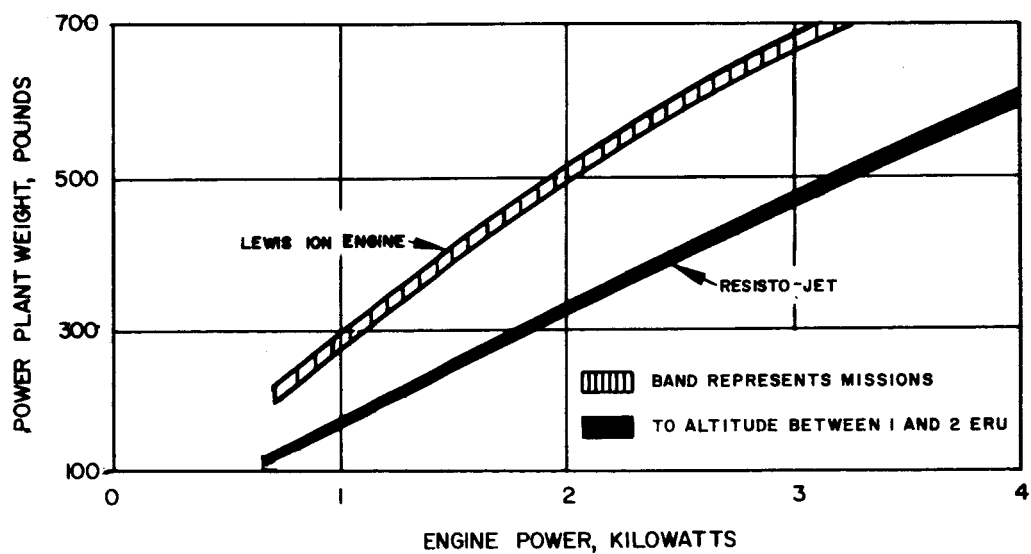


Figure 5-22. Variation of Total Power System Weight with Electric Engine Power Requirements

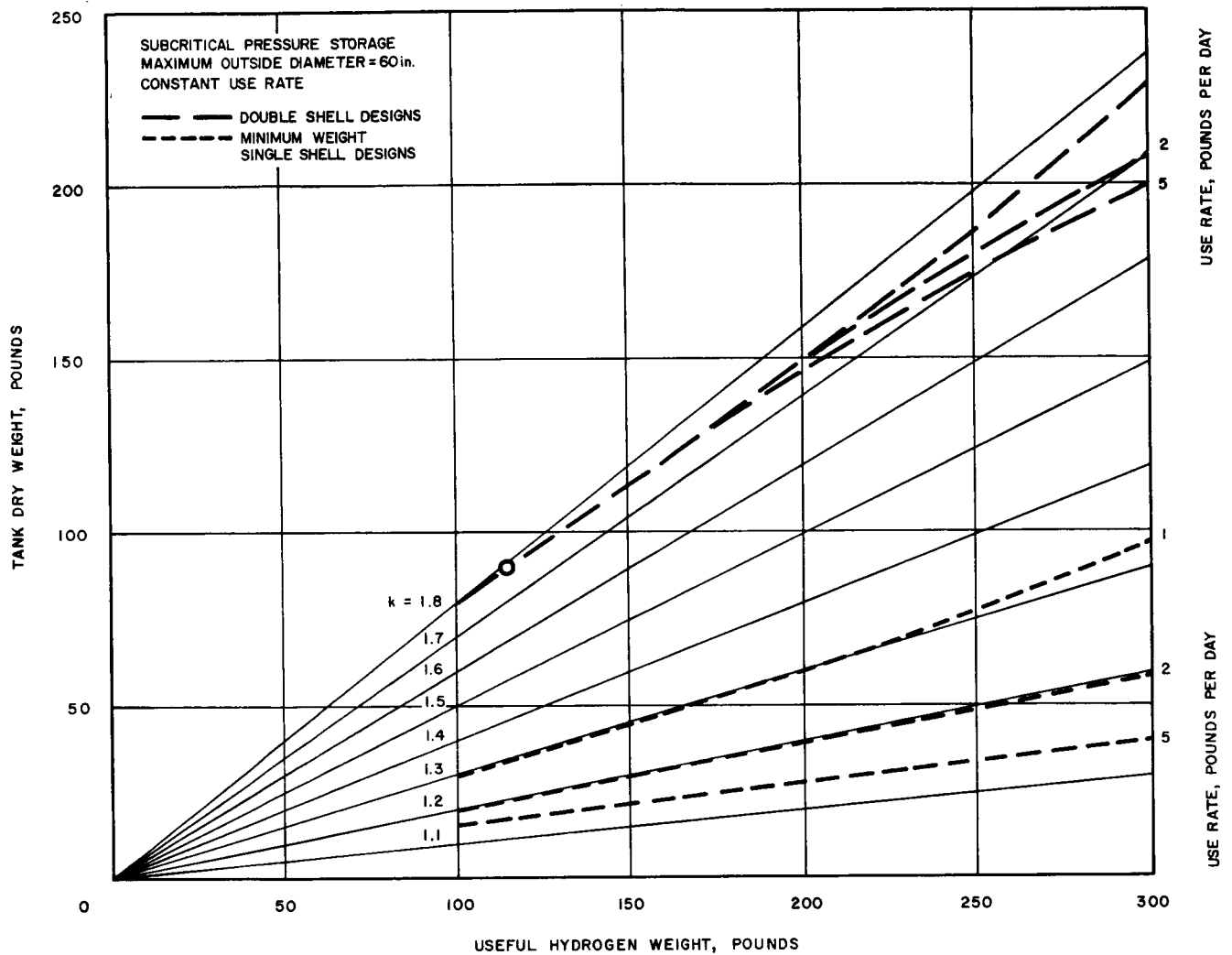


Figure 5-23. Hydrogen Storage Tank Weight Variation with Propellant Weight and Use Rate

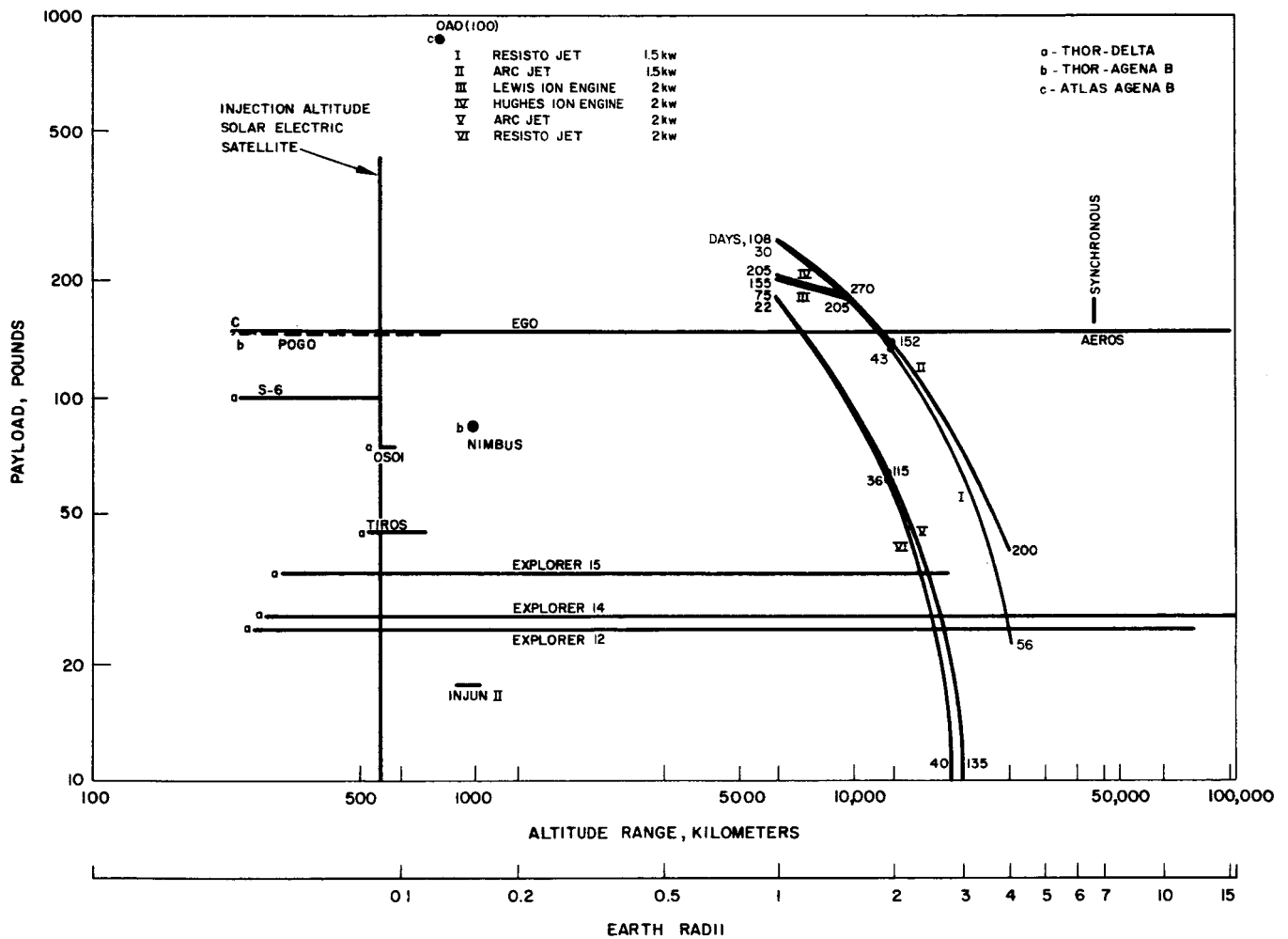


Figure 5-24. Solar Electric Spacecraft Mission Performance  
a) Payload Variation with Orbital Altitude

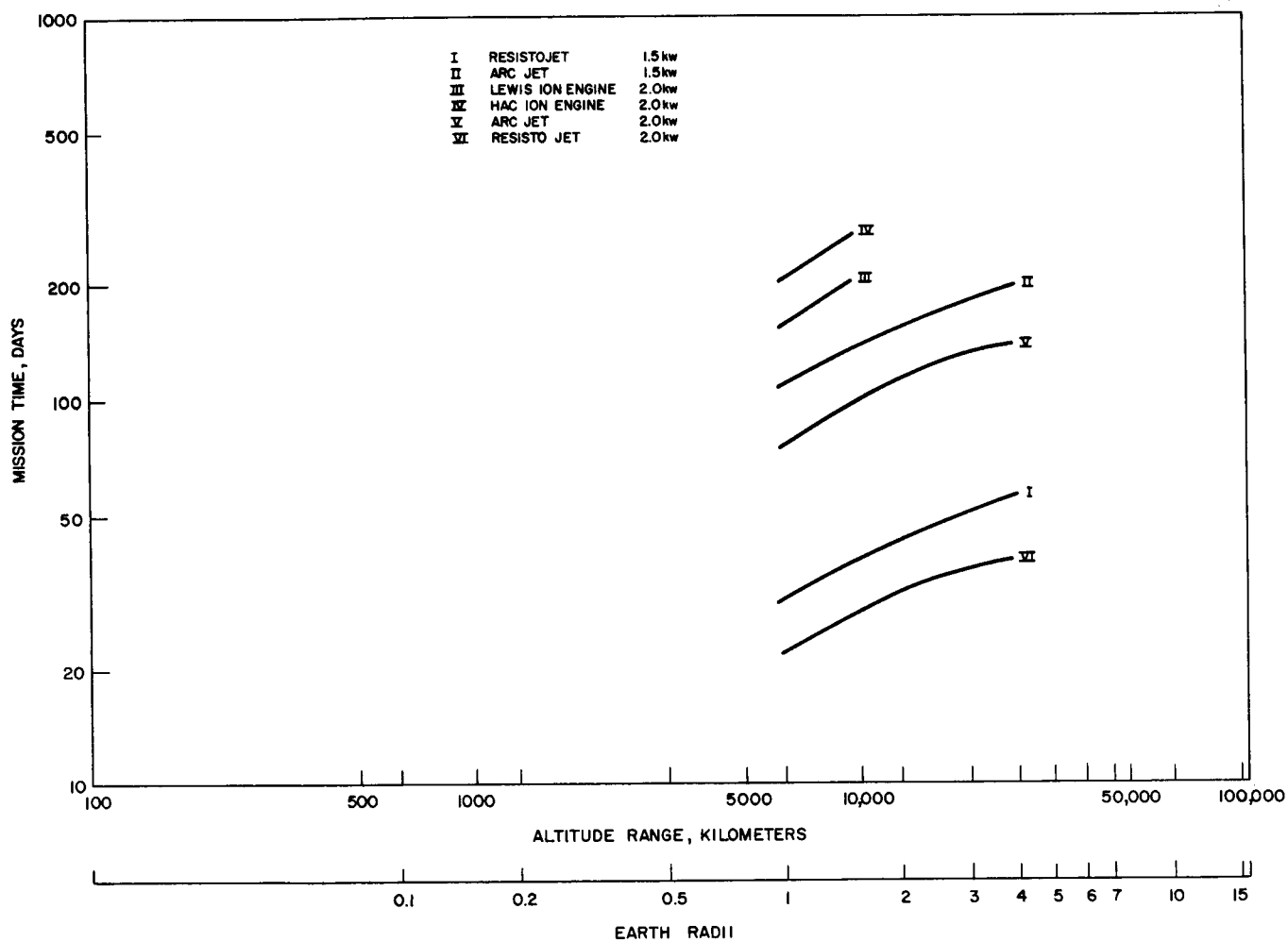


Figure 5-24 (continued).  
b) Mission Time Variation with Orbital Altitude

TABLE 5-1. NASA GEOCENTRIC SATELLITE MISSION CHARACTERISTICS

NASA Mission	Mission Objectives	Code Name	Launch Vehicle	Orbit, km		Orbit Inclination, degrees
				Perigee	Apogee	
Orbiting Geophysical Observatory	Areas of scientific investigation will include terrestrial phenomena; physics of electric, magnetic, gravitation fields and energetic particles in space, solar properties, micrometeorites and electromagnetic radiation.	Injun II (b) EGO POGO Goddard S-6 Explorer 12 Explorer 14 Explorer 15 TRS-1	Thor-Ablestar Atlas-Agena B Thor-Agena B Thor-Delta Thor-Delta Thor-Delta Thor-Delta Thor-Agena (Rand D)	890 280 250 240 266 280 310 ~1000	1,020 110,000 920 563 77,000 98,000 17,300	67 33 90 30 33 33 33 83
Orbiting Solar Observatory	Measure electromagnetic radiation from sun in ultraviolet, X-ray and $\gamma$ -ray regions of spectrum and study time variations of emissions.	OSO Mod A Mod B	Thor-Delta Atlas-Agena	553 Circular	595 600	33
Orbiting Meteorological Observatory	Obtain data on heat budget, cloud cover for operational use in weather forecasting.	TIROS NIMBUS AEROS	Thor-Delta Thor-Agena B Centaur	511 Circular Circular	735 965 36,100	58 90 0
Orbiting Astronomical Observatory	Studies of cosmic phenomena--X-rays, ultraviolet, and infrared rays--observed to ground observatories by earth's atmosphere.	OA I II III	Atlas-Agena B	Circular	805	50
Communication Satellite	Provide intercontinental communication 24 hours a day.	RELAY SYNCOM I SYNCOM II TELSTAR	Thor-Delta Thor-Delta Atlas-Agena Thor-Delta	1450 Circular Circular 950	4,830 36,100 36,100 5,650	50 33 0 44.8
Geodetic Satellite	Study of earth's shape; provide a triangulation point in space for precise distances and positions on earth	ANNA IA ANNA IB	Thor-Ablestar Thor-Ablestar	Failed to orbit 1080	1,170	~50 50

TABLE 5-1. (Continued)

NASA Mission	Code Name	Orbiting Gross Weight, pounds	Scientific Payload, pounds	Payload Operating Power, watts	Life Time, years	Period, minutes	Data Storage, bits/sec -1	Data Transmission, bits/second
Orbiting Geophysical Observatory	Injun II (b)	55	18	4	>1	104	{ 500 for 3 hours to Telstar I 1000 for 8 hours to Telstar II	2 x 10 <sup>5</sup> 50
	EGO	900 - 1500	150 - 500	50 - 250	>0.5	1800		
	POGO	950	150	50	>0.5	100		
	Goddard S-6	375	100	40	1	93		
	Explorer 12	83	25	16	1	1585		
Orbiting Solar Observatory	Explorer 14	89	27	20	2	2184		256
	Explorer 15	98	35	22	2	312		
	TRS-1	1.4	<0.1	0.6	>0.5	106		
	OSO Mod A	458	75	25	1	96		
	Mod B				1			
Orbiting Meteorological Observatory	Tiros	280 - 286	45	25	0.5	100		1000 1000
	Nimbus	650	85	375	1	108		
	Aeros	900 - 1500	150 - 500	100 - 500	1	1440		
Orbiting Astronomical Observatory	OAO I II III	3300	850	350	1	100		
Communication Satellite	Relay	115	7	80	0.5	160		
	Syncom I	140	10	25	1	1440		
	Syncom II	1000	10	150	1	1440		
	Telstar	170	5	80	0.5	158		
Geodetic Satellite	Anna IA	355	6		1	108		
	Anna IB	350	6		1			



TABLE 5-2. ORIENTATION REQUIREMENTS FOR NASA GEOCENTRIC SATELLITES

NASA Mission	Payload Code Name	Launch Vehicle	Spacecraft Gross Weight, lb	Orbit		Payload Operating Power, w	Launch Date	Mission Objectives	Attitude Control		Duration	Life Time	24-Hour Satellite Stationkeeping
				Perigee	Apogee				θ	φ			
Orbiting Geophysical Observatory	Explorer XII Injun II (b) POGO Coddard S-6	Thor-Delta Thor-Ablestar Atlas-Agena B Thor-Agena B Thor-Delta	83 92 900-1300 950 375	165 Circular 178 155 150	47,858 621 68,500 570 350	16 4 50 50	August 1961 1962 1963 1963	Areas of scientific investigation will include the terrestrial plasma, physics of fields and energetic particles in space, solar properties, gravitation, and micrometeorites.	± 2 deg		Continuous attitude control (earth-sun)	6 mo to 1 yr	
Orbiting Solar Observatory	OSO	Thor-Delta	458	344	370		March 1962	Measure electromagnetic radiation from the sun in the ultraviolet, X-ray, and gamma ray regions of the spectrum and study the variations of the emissions.	± 0.5 deg	$\pm 1.2 \times 10^{-4}$ deg sec <sup>-1</sup>	Continuous attitude control (earth-sun)	1 yr	
Meteorological Satellite	Tiros IV Nimbus Aeros	Thor-Delta Thor-Agena B Centaur	285 650 1,000	457 Circular 24-hr	511 600	25 375	February 1965 1962 1966	Obtain data for operational use in weather forecasting.	± 1 deg Nimbus ± 0.1 deg Aeros	$\pm 0.05$ deg sec <sup>-1</sup> $\pm 0.01$ deg sec <sup>-1</sup>	Continuous attitude control for life time	6 mo	20 fps yr <sup>-1</sup> E-W 170 fps yr <sup>-1</sup> N-S ± 0.1" longitude and latitude (Aeros)
Communication Satellite	Relay Syncom I Syncom II	Thor-Delta Thor-Delta Atlas-Agena	115 140 1,000	900 24-hr 24-hr	3,000 (22,240 mi) 600	80 25 150	1962 1963	Provide Intercontinental communications 24 hrs. a day.	± 0.5 deg spin stab. ± 0.1 deg 3 axis		Precession control Continuous (inertial)	1 yr	20 fps yr <sup>-1</sup> E-W 170 fps yr <sup>-1</sup> N-S ± 0.1" longitude and latitude
Geodetic Satellite	ANNA	Thor-Ablestar	355	Circular	600		May 1962	Study of the earth's shape; provide a triangular point in space for determining precise distances and positions on earth.	± 0.1 deg		Continuous attitude control for life time (earth)	1 yr	
Orbiting Astronomical Observatory	OAO	Atlas-Agena B	3,300	Circular	500	350	1963	Studies of cosmic phenomena - X-rays, ultraviolet, and infrared rays - obscured to ground observatories by the earth's atmosphere.	± 1 Min ± 6 sec	$\pm 5 \times 10^{-5}$ deg sec <sup>-1</sup>	Continuous orientation control (stellar) photo exposures at precise altitudes	1 yr	

TABLE 5-3. NASA GEOCENTRIC SATELLITE DISTURBANCE TORQUES

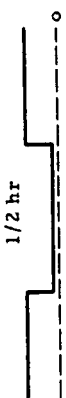
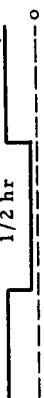

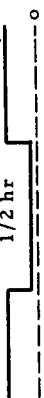







NASA Mission	Payload Code Name	Orbital Altitude		Orbit Inclination	Disturbance Torques, dyne-cm			Variation per Period		
		Perigee, km	Apogee, km		Peak	Earth's				
						Minimum	Torque		Time in Shadow	
Orbiting Geophysical Observatory	Explorer XII	266	77,000	33.3						
	Injun IIb	1,000	1,000		100		70			
	EGO	280	110,000	90	100		70			
	POGO	250	920							
Goddard 5-6	241	563								
Orbiting Solar Observatory	OSO	553	595	33	60	45	30			
	Tiros	735	511	58	50	40	30			
Nimbus Aeros	965	600	90	1,000	800	60	800			
Relay	1,450	4,830	50	20	15	10	10			
Syncom I	36,100	36,100	33	15	-	10	10			
Syncom II	36,100	36,100	0	20	-	10	10			
Anna	965	965	33	50	45	30	30			
Orbiting Astronomical Observatory	OAQ	805	805	(50)?	1,000	750	700			

TABLE 5-4. NASA GEOCENTRIC SATELLITE PAYLOAD DESCRIPTIONS

NASA Mission	Payload Code Name	Type of Injection	Number of Periods of Thrust for Final Orbit (excludes main boost)	H	E	Cosmic Ray	X-Ray	Ultraviolet	γ-ray	Ion Density (protons)	Electron Density
Orbiting Geophysical Observatory	Explorer XII Injun IIb EGO POGO S-6	Direct	1	x		x			x	x	x
			1	x	x	x	x	x	x	x	x
			1	x	x	x	x	x	x	x	x
			1	x	x	x	x	x	x	x	x
Orbiting Solar Observatory	Mod A Mod B	Direct	1			x	x	x	x	x	x
Meteorological Satellite	Tiros Nimbus Aeros	Direct Direct Parking orbit	1				x	x		x	x
			1				x	x		x	x
			3				x	x		x	x
Communication Satellite	Relay Syncom I Syncom II	Direct Direct Parking orbit	1	Strictly Communication						x	x
			1								
			3								
Geodetic Satellite	Anna I Anna II	Direct Direct	1 1	Primarily to study Earth's shape							
Orbiting Astronomical Observatory	OAO	Direct	1								

TABLE 5-4. (Continued)

NASA Mission	Payload Code Name	Meteorite Density	Near Infrared	Far Infrared	Visual (television)	Astrophysics		Geological	Aeronomy			Attitude Control	Station-keeping
						Solar	Astro		Atmosphere Composition	Pressure	Temperature		
Orbiting Geophysical Observatory	Explorer XII	x						x			x		
	Injun IIb	x						x	x	x	x		
	EGO	x						x	x	x	x		
	POGO S-6	x	x	x				x	x	x	x	x	
Orbiting Solar Observatory	Mod A	x		x								x	
	Mod B	x		x		x	x					x	
Meteorological Satellite	Tiros		x		x	x		x			x	x	
	Nimbus		x		x	x		x			x	x	
	Aeros	x	x		x	x		x			x	x	x
Communication Satellite	Relay												
	Syncom I											x	x
Geodetic Satellite	Syncom II											x	x
	Anna I							x					
Orbiting Astronomical Observatory	Anna II							x					
	OAO		x	x	x						x	x	

TABLE 5-5. NASA GEOCENTRIC SATELLITE LAUNCH SCHEDULES

NASA Mission	Payload Code Name	Scheduled Launchings					
		1962	1963	1964	1965	1966	1967
Orbiting Geophysical Observatory	Explorer XII	9	3	5	9		
	Injun I Ib						
	EGO		2	2	2		
	POGO			2	2		
	S-6						
Orbiting Solar Observatory	Mod A	2	2	2	2		
	Mod B			1	2		
Meteorological Satellite	Tiros	2	2				
	Nimbus			3	3	3	
	Aeros			1	2	2	
Communication Satellite	Relay	1	1				
	Syncom I		1		1		
	Syncom II						
Geodetic Satellite	Anna I	1					
	Anna II	1					
Orbiting Astronomical Observatory	OAQ			2	2		

NASA missions like EGO and the Explorer Series 12, 13, and 14 spend more than half of the orbit period outside 5 earth radii altitude and consequently pass through the radiation belt rapidly. In this same region up to 5 earth radii, the solar-electric system spends all of its time.

All the electric engine systems would be satisfactory for mission altitude of 1 earth radius. However, taking into account the time element, the resisto-jet with 2-kilowatt power level would lift 182 pounds to 1 earth radius in 20 days as compared to 55 days for the 1-kilowatt resisto-jet with 336 pounds. Any of the engines would accomplish the mission in less than 205 days.

Another factor influencing the mission selection is the location of the plane of the orbit. The data presented in Figure 5-24 are mostly equatorial ( $i \approx \pm 33$  degrees) for the NASA missions except for POGO, INJUN I and II, TIROS, and NIMBUS. All the solar-electric data are for polar orbits ( $i \approx 97$  degrees). The solar-electric satellite in an equatorial orbit would have a greater payload capability than indicated here for polar orbits.

## MISSION PAYLOAD

### Scientific Instrumentation

In the selection of a typical scientific payload that would adequately demonstrate the potentialities of solar-electric satellites, the most complete NASA payload was considered. From an evaluation of the NASA programs and the proposed payloads in terms of scope and weight, the OGO-series payload and in particular the POGO payload was selected. The 150 pounds of scientific experiments fit within the performance specification of the solar-electric satellites (See Section 5).

The OGO-series payload package is unique in that the use of a standardized door concept on which some of the experiments are mounted, provides access to experiments on the door and within the compartment.

In lieu of repositioning all the scientific instruments typical for the OGO-series satellites, the mounted main body "refrigerator door" concept was retained. In this way a better comparison of mission capability could be made between the conventional fixed orbit concept like OGO and the spiraling concept such as that of the solar-electric-propelled satellites.

For all practical purposes the OGO payload can be considered in three sections:

- 1) The refrigerator door compartments.
- 2) The volume between the refrigerator doors.

- 3) Solar and antisolar sensors that are completely separated from the above compartments.

The separation is based on the need for a package containing sensors to be oriented with respect to the local vertical (geophysical and anti-geophysical measurements) and other sensors oriented with respect to earth-sunline (solar and antisolar). This is one of the basic requirements of the OGO-series satellites and can be met with a solar-electric satellite system. Adopting the same payload internal arrangement as proposed for OGO (scientific instrumentation only) the accessibility of checking equipment and interchanging the instruments is retained.

The only major difference between the payload of the solar-electric satellite and the OGO series is in the overall volume of the package. The area requirements and flat surface mounting requirements are met. As previously stated, only the OGO refrigerator doors are kept and the required additional volume is retained between the doors. This gives a volume of 45 by 33 by 28 inches.

Other experiments that are sensitive to the residual magnetic fields of the satellite, the ion sheath, and other stray fields of the satellite are mounted on booms at specified distances from the main body to minimize the effects of the stray fields. The solar and antisolar experiments are mounted on solar panels to maintain orientation in the direction of the sun.

The payload capability provides at least 50 experiments that can be individually changed to facilitate many types of geophysical and astrophysical measurements. These measurements fall into the following categories (not in order of importance):

- 1) Magnetic field — The magnitude, direction, and variation of the geomagnetic field and near-earth interplanetary magnetic field.
- 2) Energetic particles — The flux, composition, and energy spectrum of trapped, solar, and interstellar energetic particles (subatomic).
- 3) Dust — The flux, composition, and energy spectrum of micrometeoritic particles in an interplanetary space near earth.
- 4) Atmospheric structure — The pressure, temperature, composition, and density of the terrestrial and cislunar atmosphere.
- 5) Ionosphere — The electrons and ion densities and temperatures from near earth and interplanetary space near earth.

- 6) Solar physics — Solar monitors in the ultraviolet, X-ray, and gamma-ray regions.
- 7) Astronomy — Survey measurements in the ultraviolet, X-ray, gamma-ray, and very low frequency regions of the spectrum.
- 8) Meteorology — Observations of earth in infrared regions for weather.
- 9) Planetary tests — Test bed for instruments proposed for planetary surface and environment probes.
- 10) Technological — Tests of power supplies, thermal control, structures, and interface problems.
- 11) Biological — Tests to establish the behavior of life forms in the space environment.
- 12) Miscellaneous — Measurements of night airglow radiations, auroral radiations, vehicle charge, electric fields, and other experiments pertinent to studying terrestrial and cislunar space.

#### Telecommunications and Data Storage

The communications and data handling subsystem of the solar-electric spacecraft is provided to process, store, and telemeter the measurements from at least 50 scientific experiments and pertinent spacecraft operational data.

This subsystem includes the spacecraft components and the ground-based components that provide high reliability, accuracy, and command control of readout phase.

The vehicle communication system consists of redundant solid-state Minitrack beacons, command receivers, and telemetry transmitters and tape data storage systems. The individual redundant subsystem may be selected by ground command except those where both units are on at all times. The Minitrack system will be used to determine vehicle position and is capable of measuring altitude to better than 1-mile accuracy. The command system will permit the execution of up to 64 ground commands. The 1- and 10-watt PCM/PM/Pm telemetry transmitters will permit data transmission rates of 1024 and 40,960 bits per second to NASA tracking stations (60-foot dish) with about 10-db overall power margin. The tape storage system is capable of recording over 11,000,000 bits of data over a 12-hour period with playback in 270 seconds. This is twice the storage capacity required by the OGO-series spacecraft.



## GENERAL ARRANGEMENTS

Configuration studies were conducted in which solar panel deployment methods and tankage and propulsion system location were varied to provide maximum payload weight in a simple configuration compatible with the Thor-Agena launch vehicle and POGO experiment package. The large size of the experiment package and its orientation requirements are major design parameters. Solar panel stowage is also critical, especially the large areas required for ion engine operation which severely limits available volume within the Agena shroud. Two types of vehicle configurations have evolved. The first is a cross-type solar panel arrangement in which primary solar panel deployment hinges are located at the vehicle separation plane with solar panels stowed box-like within the Agena shroud and with payload and propulsion systems mounted on supporting structure within the box. The second type of vehicle configuration uses two rectangular solar panels with primary hinge lines parallel to the vehicle centerline with panels stowed by folding into an eight-sided box within the Agena shroud.

The first type of deployment permits  $360 \text{ ft}^2$  of solar panel using eight secondary hinge lines, while the second type of deployment permits only  $160 \text{ ft}^2$  of panel using eight secondary hinge lines. The cross type arrangement is best suited for ion engine propelled vehicles where power levels in excess of 2 kw are required; the second configuration is better suited for resisto-jet propelled vehicles because of the lighter tank structure attainable with the greater design freedom allowed in this configuration.

In flight the solar panels must be oriented normal to the sun to receive maximum illumination, thus placing them approximately parallel to the plane of the polar orbits considered.

Thrust is applied in a direction parallel to the solar panel plane and through the vehicle center of gravity. Both thrust vector and experiment package surface must be maintained normal to local vertical during flight. Thrust vector orientation is accomplished by attitude control of the spacecraft while the experiment package orientation is maintained by gimbal and turntable mounts.

The vehicle communication systems consist of redundant solid-state Minitrack beacons, command receivers, and telemetry transmitters and tape data storage systems.

Attitude control of the vehicle is accomplished by cold gas thrusters located at the periphery of the solar panels. The vehicle pitch axis is aligned to the sun vector by means of a simple shadow graph sun sensor, and the vehicle is pitched to place local vertical midway between the yaw and roll axes by means of a horizon scanner. Sufficient nitrogen cold gas is provided to maintain vehicle orientation against gravity gradient, drag, magnetic, and solar pressure torques throughout the powered flight and for 1 year thereafter.

### Ion Engine Configuration

Figures 5-25 and 5-26 show the "cross" configuration with ion engines. The vehicle consists of a scientific payload package, tubular truss structure, and solar panel packaged to fit inside a 56-inch-diameter envelope. The experiment package is located at the forward end of the spacecraft on long supporting structure with the propulsion system and miscellaneous components grouped around the vehicle center of gravity. The large solar panel required for ion engine operation restricts the orientation of the POGO package in the stowed position. The thrust vector is directed between solar panel arms to minimize possible solar panel damage from engine exhaust plume. To maintain proper experiment orientation, the payload package must be pivoted on an axis parallel to the thrust vector to eliminate misorientation due to vehicle roll. This is accomplished by mounting the payload package on an A-frame gimbal which, in turn, is mounted on a turntable which can be rotated 45 degrees to align gimbal and thrust axes.

Electric gear and thermal radiators are mounted in a bay directly below the turntable. The next bay down contains two electric engine capsules, two attitude control gas tanks, and a 7-inch-diameter mercury fuel tank. The solar panel deployment mechanism is packaged in the next bay down. The square truss structure is attached to the circular separation ring. Use of cross members on the square truss allows tiedown to the separation ring at eight places. The separation ring mates with a ring on top of an adapter cone on the Agena. Two 25-foot extendible boom mechanisms are mounted just above the separation plane. Four packages with sensor and/or attitude control jets are mounted on the solar panel tips. The center solar panel is hinged to the structure and two outboard panels are hinged to the center panel.

### Dual-Tank Resisto-Jet Engine Configuration

Figure 5-27 shows the "cross" configuration with a resisto-jet engine. A turntable is unnecessary on the resisto-jet-powered vehicle because the smaller solar panels required allow the experiment package gimbal to be oriented parallel to the thrust line with the solar panels in the stowed position.

The vehicle consists of three basic structural subassemblies. A magnesium sheet and stringer is provided as an adapter between the Agena forward attachment rings and the separation is effected by release of a Marman-type clamping ring (similar to Syncom II).

The structure forward of the separation plane is a magnesium alloy sheet-stringer fabrication, extending to a channel section ring on the aft LH<sub>2</sub> tank. This section accommodates the data storage system, transmitters, receivers, control electronics, radiators, and thermal switches.

The intertank structure is a magnesium alloy weldment of tubing similar in concept to an aircraft "engine mount" truss. This truss connects to channel section rings on both LH<sub>2</sub> tanks and provides support for the resisto-jet engines and controls and for the N<sub>2</sub> tanks.

The experimental package is supported in trunnions forward of the LH<sub>2</sub> tanks to provide a clear view of earth in all operational attitudes. The battery is also installed in this compartment. The trunnions accommodate the rotary actuators and are mounted to the forward LH<sub>2</sub> tank ring by two tripods of magnesium alloy tubing.

The solar cells are mounted on four hinged panels. Each panel is comprised of three hinged subpanels. The center subpanels are hinged to the main structure forward of the separation ring to permit rotation to the deployed position. Actuators are provided to rotate the panels into the pitch plane, and simple mouse-trap springs with suitable damping are used to align the subpanels.

Solar-oriented experimental packages are attached to the outboard ends of the panels. Boom-mounted experiments are also attached to these panels and extended on tubes of preformed tape, similar to Lofti 1 antennas.

#### Single-tank Resisto-Jet Engine Configuration

Figures 5-28 and 5-29 show the rectangular panel configuration with a resisto-jet engine. In this configuration, solar panels are stowed in an eight-sided box around a cylindrical hydrogen tank. When deployed, they form two rectangular panels in a plane through the vehicle centerline. Resisto-jet engines are mounted aft on the vehicle centerline. The POGO experiment package is mounted forward on a turntable which maintains proper experiment orientation while the vehicle rolls to maintain maximum illumination of the solar panels.

Experiments are mounted on the solar panel tips and on two 25-foot extendible booms mounted in a plane perpendicular to the solar panel plane. Six cold gas jets are used to control roll, yaw, and pitch attitude.

The structure consists of a conical payload attached to a corrugated aluminum cylindrical shell stabilized by rings. This corrugated shell is the primary structure and transmits all loads to an adapter cone on the Agena booster. A circular honeycomb panel at the separation plane is used as the aft closure and supports the electronic equipment, cold gas attitude control tank, and the resisto-jet engines. The LH<sub>2</sub> tank is supported by an inverted truncated cone attached to the top of the corrugated cylinder and to the intersection of the top hemispherical dome and the cylindrical portion of the LH<sub>2</sub> tank. A band of fiberglass in the tank support acts as a thermal

barrier between the outer corrugaed cylindrical shell and the LH<sub>2</sub> tank. Heat conduction through fill and drain and overboard vent lines is minimized by attaching these lines to fiberglass panels on the corrugated shell. On-pad insulation is provided by a helium gas purge. Tensitized dacron bags are used to seal the top and bottom of the LH<sub>2</sub> tank during the helium gas purge. Any cracks through joints on the corrugated shell can be sealed with pressure-sensitive tape. The helium gas is dumped overboard through valves during the boost phase. One inch of perforated aluminized mylar insulates the LH<sub>2</sub> tank during the remainder of the mission. The aluminized mylar is attached to the inside of the corrugated shell. Dacron bag seals, with approximately 1 inch of clearance between the LH<sub>2</sub> tank and the insulation, prevent heat conduction transfer to the tank. This insulation scheme is lightweight, efficient, and relatively simple to install and provides a substantial increase in payload over the dual-tank design.

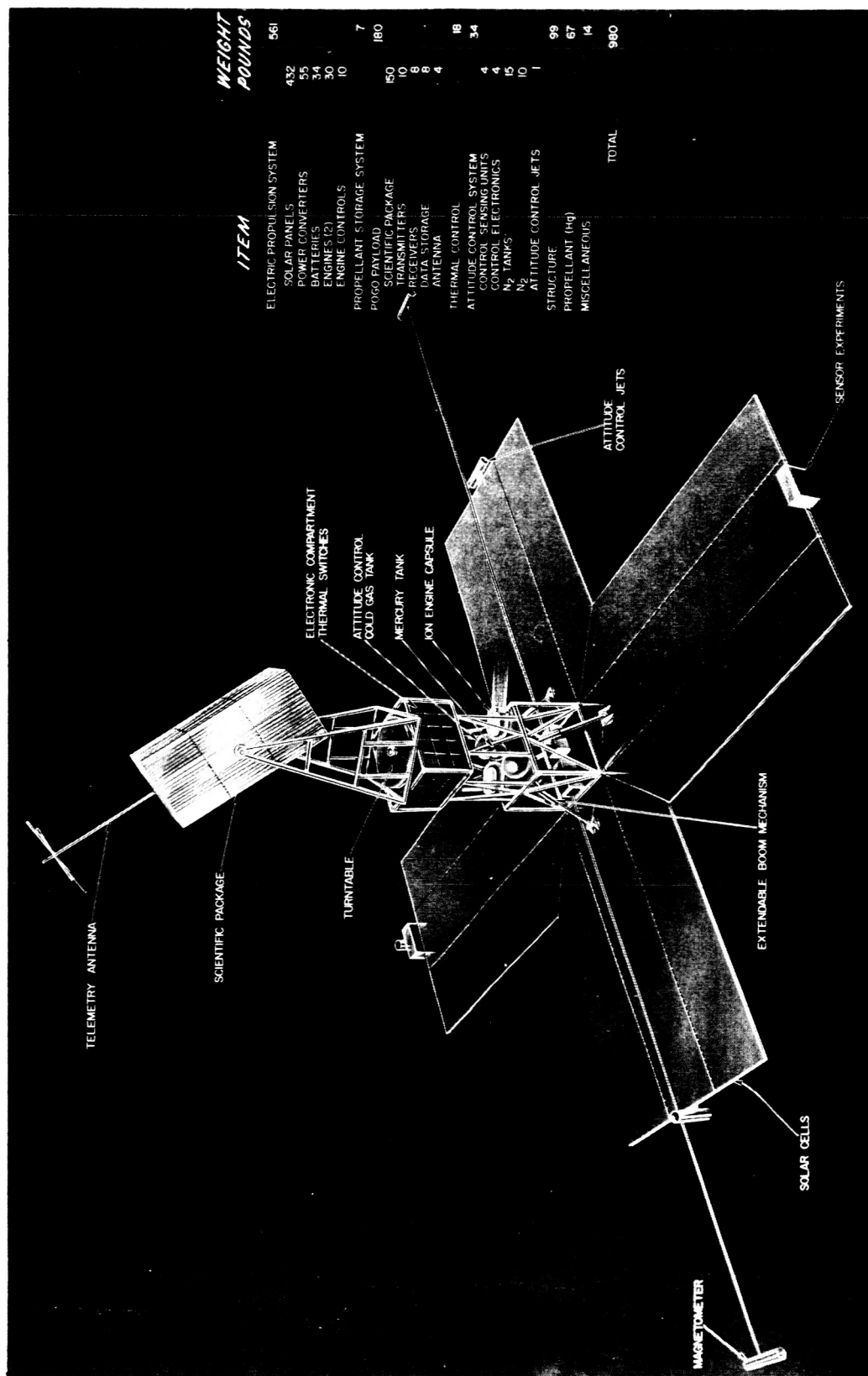


Figure 5-25. Ion Engine Spacecraft Perspective View

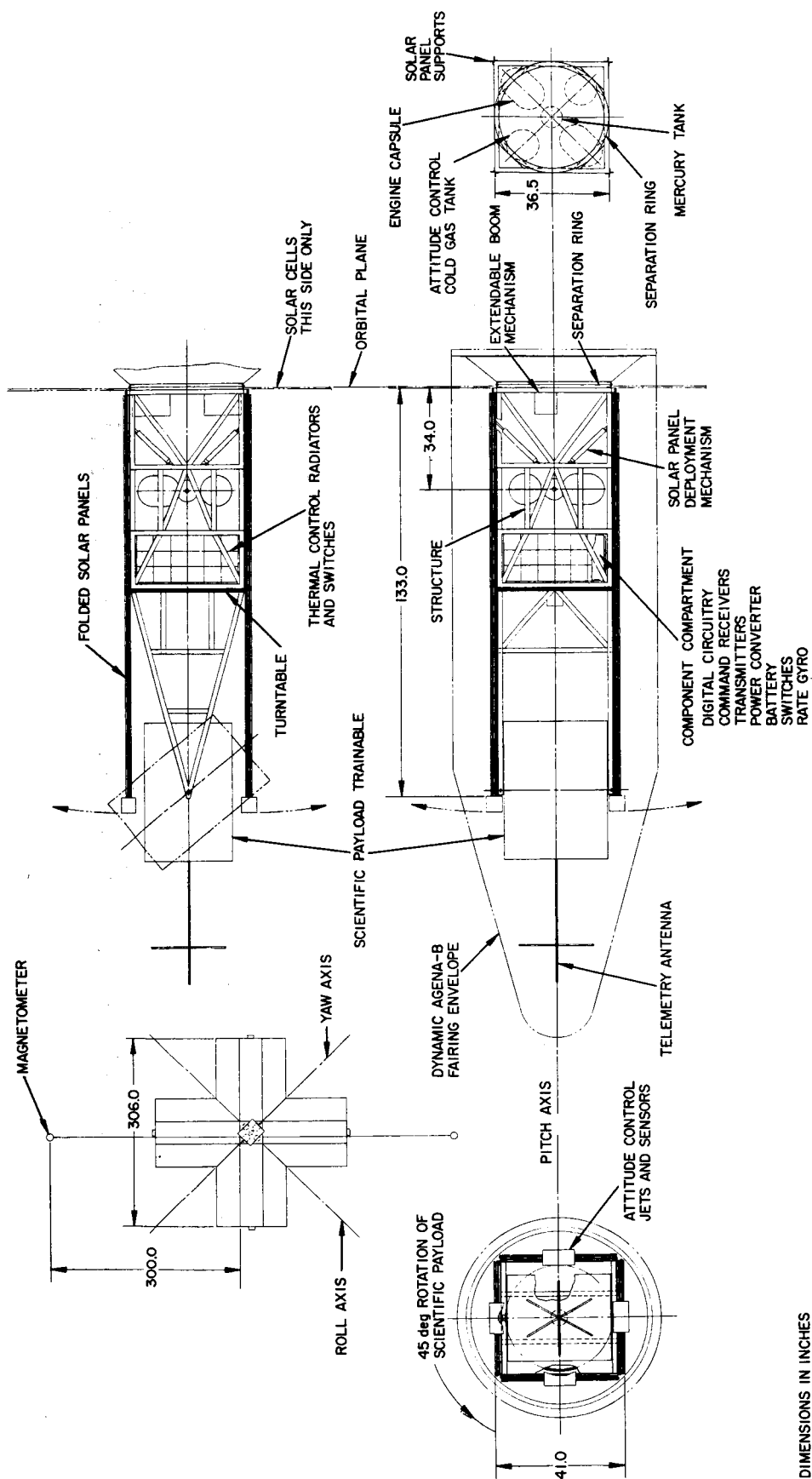
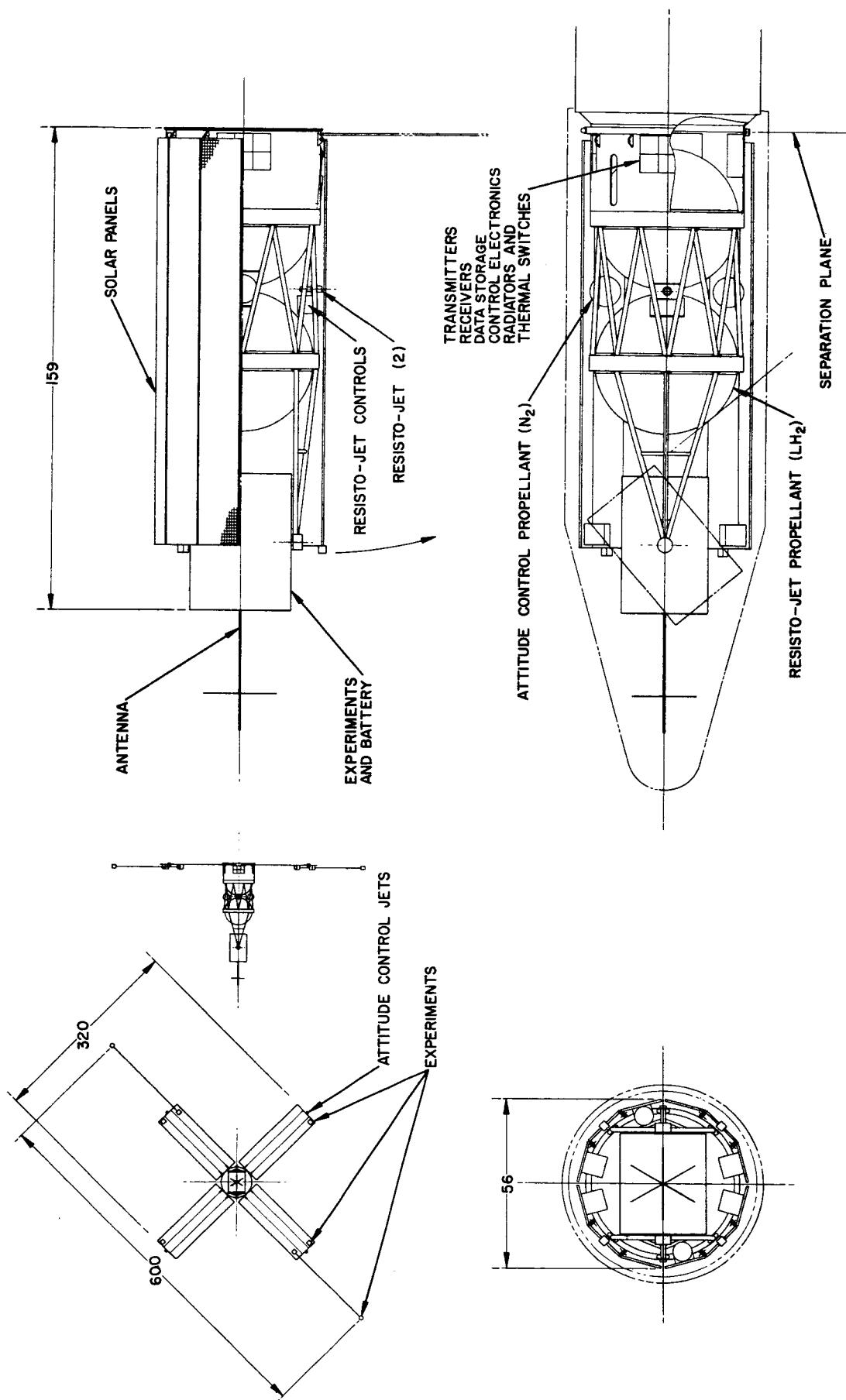


Figure 5-26. Ion Engine Spacecraft General Arrangement



DIMENSIONS IN INCHES

Figure 5-27. Dual-Tank Resisto-Jet Engine Spacecraft General Arrangement

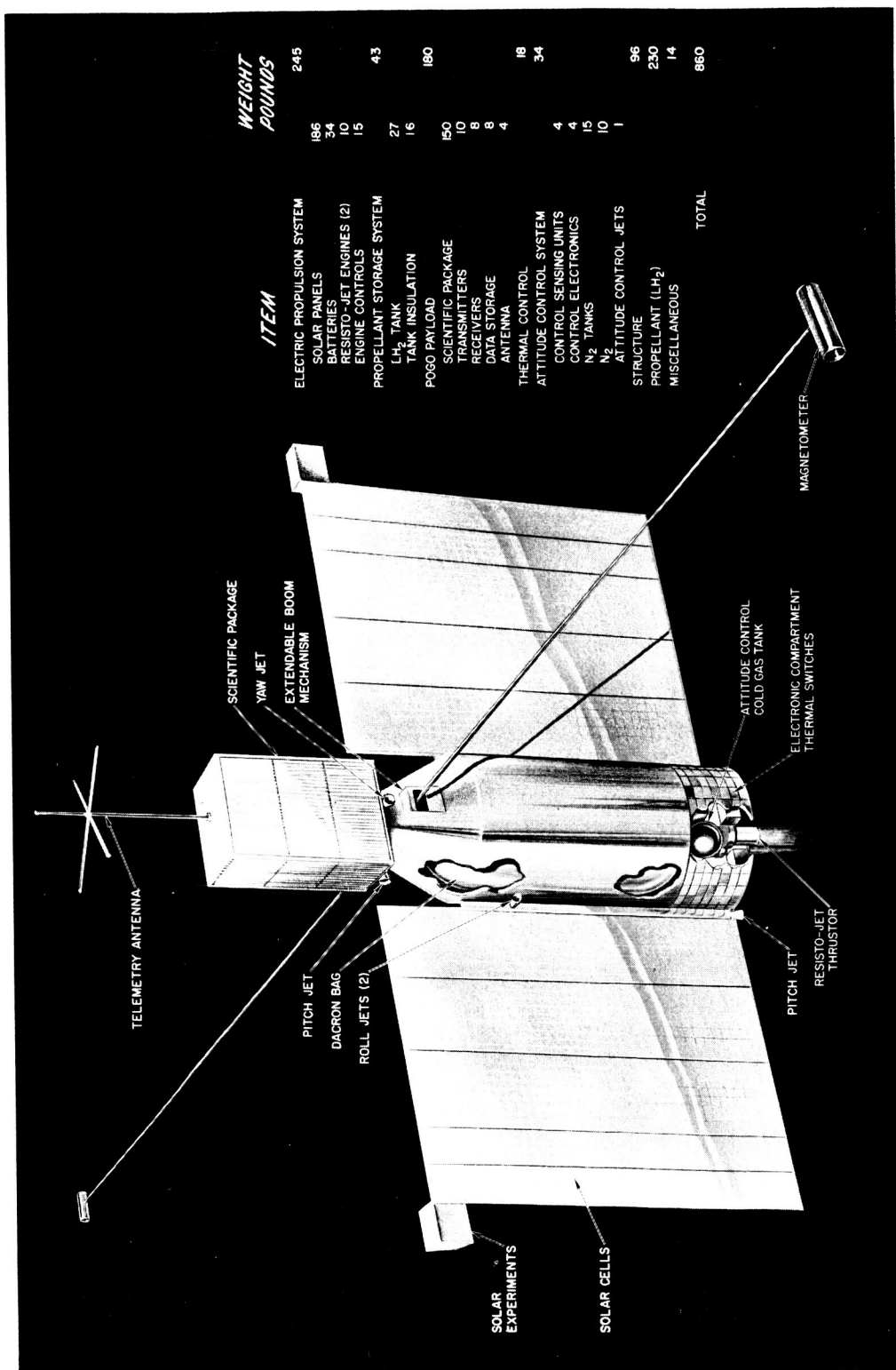
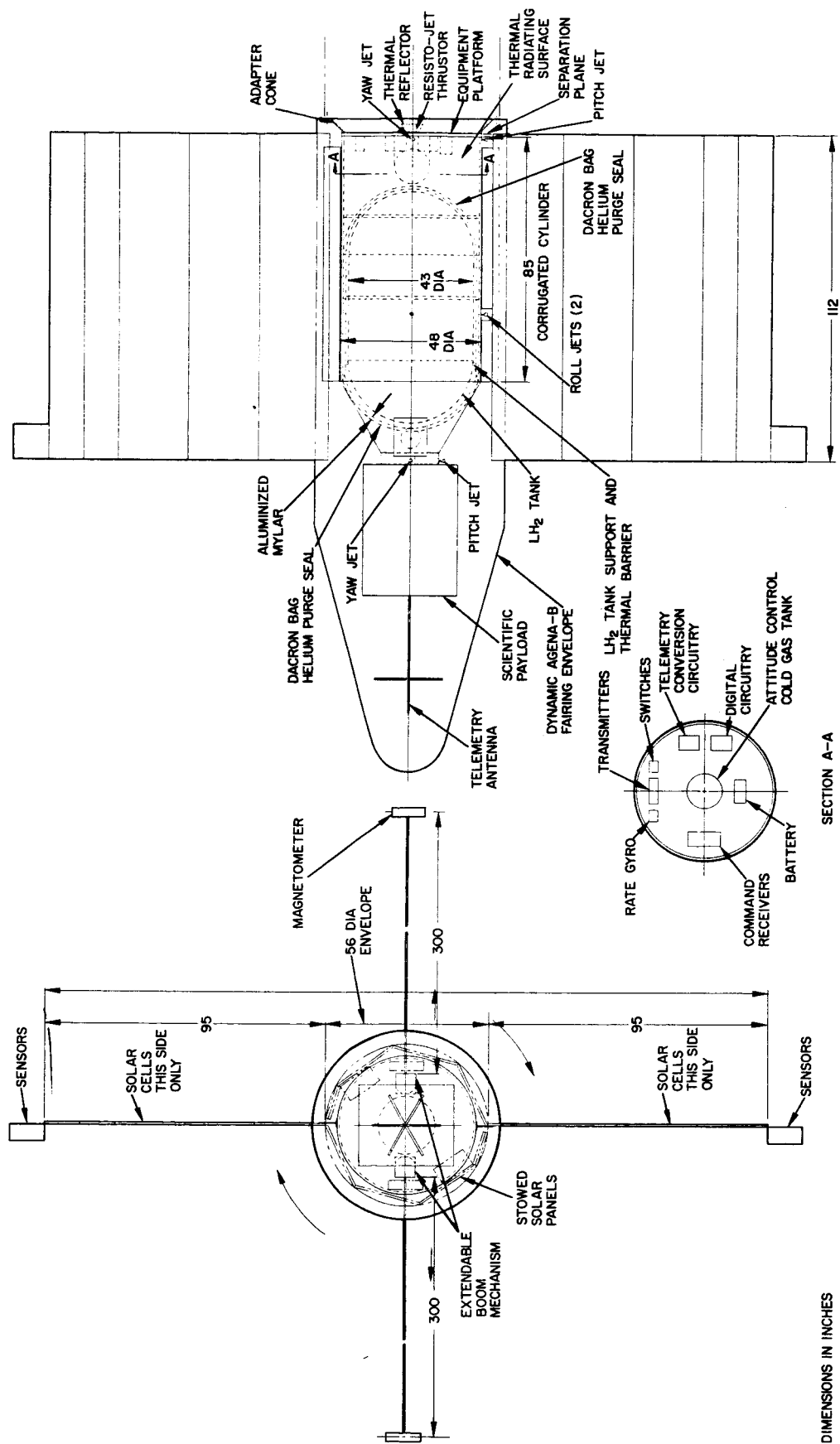


Figure 5-28. Single-Tank Resisto-Jet Engine Spacecraft Perspective View





## 6. REFERENCES

1. STL Report 8616-6012-RU-000 "Radiation Environment, Its Effect on the Solar Cell Array and the RELAY II Radiation Experiment," by A. Rosen, dated 30 March 1962.
2. Davis, L.R., and J. M. Williamson, Oral presentation at the GSFC EXPLORER XII Symposium, 18 January 1962.
3. Krausz, A., "Lifetime of Solar Cell Power Supplies", 27 August, 1962.
4. Freeman, J. W., "Detection of an Intense Flux of Low Energy Protons on Ions Trapped in the Inner Radiation Zone." Journal Geophysical Research, Vol. 67, No. 3, March 1962, pp. 921-928.
5. Heckman, H., "Energy Spectrum of Geomagnetically Trapped Protons." Journal Geophysical Research, Vol. 67, No. 4, April 1962, pp. 1255-1262.
6. STL Report 8644-600 L-RU 000, "A Comprehensive Map of the Space Radiation Environment." A. Rosen, et al., 28 September 1962.
7. "Collected Papers on the Artificial Radiation Belt from the 9 July 1962 Nuclear Detonation." Journal Geophysical Research, Vol. 68, No. 3, 1 February 1963.
8. Smits, F. M., K. O. Smith, and W. L. Brown, "Solar Cells for Communication Satellites in the Van Allen Belt," Nuclear Electronic Effects Program, Eighth Triannual Technical Note, 15 November 1961. BTL.
9. Goddard Scientific Satellite Symposium, 13, 14, and 15 March 1963. Washington, D. C.

10. Baicker, J. A., et al., "Radiation Damage to Silicon." RCA Report Contract No. NASS-457, First Semiannual Report, 1 January 1962.
11. Chow, K. T., "Proton Damage to Solar Cells," LMSD-703735-1, August 1961.
12. Aukerman, L. W., "Proton and Elextronic Damage to Solar Cells," REIC Report No. 23, 1 April 1962.
13. Loferski, J. J., "The Effect of Radiation on Silicon Solar-Energy Converters," RCA Review, Vol. XIX, No. 4, December 1958.
14. Dienes, G. J., "Radiation Effects in Solids, "Vol. 2, New York Interscience, 1957.
15. Brown, W. L., "Semiconductor Radiation Damage in Space," Nuclear Effects Program (NEEP). Seventh Triannual Technical Note, 15 July 1961, BTL.
16. Hughes Report, "Syncom Mark II, Vol. I Technical Discussion," 62H-0416/94419-002, January 1962, SSD220P, pp. 4-29.
17. Pieper, G. F., A. J. Zmuda, and C. O. Bostrom, "Solar Protons and Magnetic Storms in July 1961, "Journal of Geophysical Research, Vol. 67, December 1962.
18. Whipple, F. L., "The Meteorite Risk to Space Vehicles," Vistas in Astronautics, Vol. 1, 1957.
19. Bjork, R. L., "Meteoroids Versus Space Vehicles," presented at ARS Meeting, May 1960.
20. Secondary Power Systems Review, 1959, Wright Air Development Division, WADC TN 59-58, Report No. 59, WCLE 452.
21. STL Report TN 59-0000-00851, "Design Techniques for Regulated Static Converters," W. A. Manahan, January 1960.

## EQUATIONS USED IN TRAJECTORY COMPUTATIONS

### APPENDIX

#### INTRODUCTION

The reference system is a set of nonrotating Cartesian coordinates with the xy plane coinciding with the earth's equator and the x-axis pointing toward vernal equinox as shown in Figure A-1. The vehicle undergoes perturbations due to thrust, drag, earth oblateness, luni-solar attraction, and solar radiation. The atmosphere is assumed to be nonrotating. The sun and moon are assumed to travel in circular paths in fixed orbit planes. Angle of incidence is not considered in the calculation of radiation pressure.

On the basis of runs made with Program I, it was decided that luni-solar attraction and solar radiation may be ignored for performance studies. These forces are not considered in Programs II and III. A definition of terms and list of equations for Programs I, II, and III are presented in this appendix.

#### DEFINITION OF TERMS

$t$	- Time
$\psi$	- Argument of latitude
$r$	- Radial distance
$h$	- Angular momentum per unit mass
$i$	- Orbit inclination
$R$	- Component of perturbing acceleration along radius vector
$S$	- Component of perturbing acceleration normal to radius vector in orbit plane
$W$	- Component of perturbing acceleration normal to orbit plane

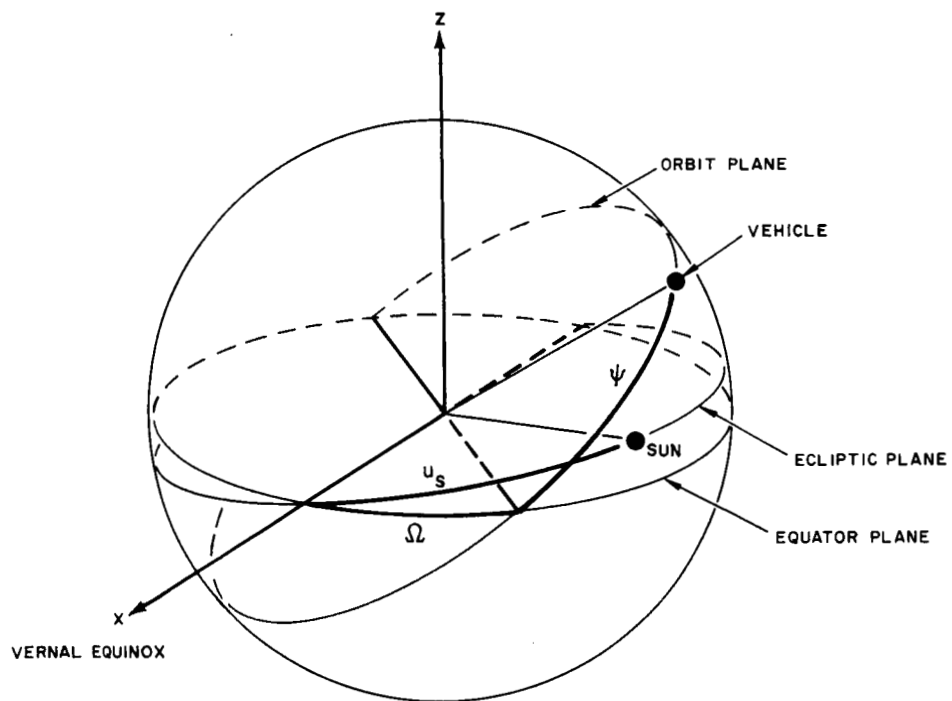


Figure A-1. Reference Coordinates

$\Omega$	- Right ascension of ascending node
$j$	- $e \sin \omega$
$k$	- $e \cos \omega$
	} $e = \text{eccentricity}$ $\omega = \text{argument of perigee}$
$\mu_x$	- Gravitational parameter of body x
$f$	- Magnitude of acceleration due to solar radiation pressure
$K_{SR}$	- Solar radiation pressure constant
$m$	- Vehicle mass
$A_s$	- Vehicle side area
$u_s$	- Argument of latitude of sun
$u_m$	- Argument of latitude of moon
$\bar{F}_s$	- Acceleration due to sun
$\bar{r}_{xy}$	- Vector from center of body x to center of body y. E, M, S, P denote earth, moon, sun, probe, respectively.
$r_{xy}$	- Magnitude of $\bar{r}_{xy}$
$\bar{F}_{OB}$	- Acceleration due to earth's oblateness
$J_2, J_3, J_4$	- Coefficients for first, third, and fourth harmonics in earth's potential
$\bar{F}_D$	- Acceleration due to drag
$\dot{\bar{r}}_{xy}$	- Time derivative of $\bar{r}_{xy}$
$P$	- Density
$A_F$	- Front area of vehicle
$\bar{F}_T$	- Acceleration due to thrust
$M$	- Matrix for transforming to orbit plane coordinates
$\phi_s$	- Declination of sun with respect to orbit plane
$\theta_s$	- Longitudinal angle of sun measured in orbit plane from line of node

- $\phi_T$  - Declination of thrust acceleration vector with respect to orbit plane
- $\theta_T$  - Longitudinal angle of thrust acceleration vector measured in orbit plane from perigee
- $E_2, E_1$  - Upper and lower limits of eccentric anomaly which define the interval of thrusting in Program III
- $n$  - Mean motion

# PROGRAM I

## Differential Equations

$$\frac{dt}{d\psi} = \frac{l}{\left(\frac{h}{r^2} - \frac{\cot i}{h} r \sin \psi W\right)} = F \quad (A-1)$$

$$\frac{dh}{dt} = F r S \quad (A-2)$$

$$\frac{d\Omega}{d\psi} = \frac{F r \sin \psi W}{h \sin i} \quad (A-3)$$

$$\frac{di}{d\psi} = \frac{F r \cos \psi W}{h} \quad (A-4)$$

$$\begin{aligned} \frac{dj}{d\psi} = F \left\{ -\frac{h}{\mu_E} \cos \psi R - \frac{k r \cot i \sin \psi W}{h} \right. \\ \left. + \frac{r}{h} \left[ \sin \psi (2 + k \cos \psi) + j (1 + \sin^2 \psi) \right] S \right\} \end{aligned} \quad (A-5)$$

$$\begin{aligned} \frac{dk}{d\psi} = F \left\{ \frac{h}{\mu_E} \sin \psi R - \frac{j r \cot i \sin \psi W}{h} \right. \\ \left. + \frac{r}{h} \left[ \cos \psi (2 + j \sin \psi) + k (1 + \cos^2 \psi) \right] S \right\} \end{aligned} \quad (A-6)$$

# Computation of R, S, W

Solar radiation acceleration

$$f = K_{SR} \frac{A_S}{m} \quad (A-7)$$

Sun-moon perturbations

$$u_s = u_{s0} + 0.11946129 t^4$$

$$u_m = u_{m0} + 0.15970197 t^3$$

$$\bar{F}_s = \frac{\mu_s}{r_{ES}^3} \left[ \frac{3}{2} \delta \bar{r}_{SP} - \bar{r}_{EP} \right] \quad (A-8)*$$

where

$$\delta = \frac{(\bar{r}_{EP} - 2 \bar{r}_{ES}) \cdot \bar{r}_{EP}}{2 r_{ES}}$$

$$\bar{F}_M = -\mu_M \left[ \frac{\bar{r}_{EM}}{r_{EM}^3} + \frac{\bar{r}_{MP}}{r_{MP}^3} \right]$$

Earth oblateness perturbation

$$\bar{F}_{OB} = -\frac{\mu_E}{r_{EP}^3} \begin{pmatrix} xP \\ yP \\ Q \end{pmatrix} \quad (A-9)$$

---

\*The computation is performed in earth radius units, minutes, and radians.



where

$$\begin{aligned}
 P = & \left\{ J_2 \left( \frac{1}{r} \right)^2 \frac{3}{2} \left[ 1 - 5 \left( \frac{z}{r} \right)^2 \right] + J_3 \left( \frac{1}{r} \right)^3 \frac{5}{2} \frac{z}{r} \left[ 3 - 7 \left( \frac{z}{r} \right)^2 \right] \right. \\
 & \left. + J_4 \left( \frac{1}{r} \right)^4 \frac{5}{8} \left[ -3 + 42 \left( \frac{z}{r} \right)^2 - 63 \left( \frac{z}{r} \right)^4 \right] \right\} \\
 Q = & z \left[ J_2 \left( \frac{1}{r} \right)^2 \frac{3}{2} \left( 3 - 5 \left( \frac{z}{r} \right)^2 \right) \right] + J_3 \left( \frac{1}{r} \right)^2 \frac{3}{2} \left[ -1 + 10 \left( \frac{z}{r} \right)^2 - \frac{35}{3} \left( \frac{z}{r} \right)^4 \right] \\
 & + z J_4 \left( \frac{1}{r} \right)^4 \frac{5}{8} \left[ -15 + 70 \left( \frac{z}{r} \right)^2 - 63 \left( \frac{z}{r} \right)^4 \right]
 \end{aligned}$$

Drag acceleration

$$\bar{F}_D = - \frac{D}{|\dot{\bar{r}}_{EP}|} \quad (0.17203694)^{-3} \quad (\dot{\bar{r}}_{EP} \text{ is given in RSW coordinates})$$

where

$$D = 0.12163514^{12} \rho |\dot{\bar{r}}_{EP}|^2 A_F \quad (A-10)$$

Thrust acceleration

$$\bar{F}_T = \frac{T (0.17203694)^{-3}}{m} \frac{\bar{r}_{PE} \times \bar{r}_{PS}}{|\bar{r}_{PE} \times \bar{r}_{PS}|} \quad (A-11)$$

$$\begin{pmatrix} R \\ S \\ W \end{pmatrix} = \bar{F}_D + \begin{pmatrix} \cos \psi \cos \Omega - \sin \psi \cos i \sin \Omega, & \cos \psi \sin \Omega + \sin \psi \cos i \cos \Omega, & \sin \psi \sin i \\ -\sin \psi \cos \Omega - \cos \psi \cos i \sin \Omega, & -\sin \psi \sin \Omega + \cos \psi \cos i \cos \Omega, & \cos \psi \sin i \\ \sin i \sin \Omega, & -\sin i \cos \Omega, & \cos i \end{pmatrix} \begin{pmatrix} \bar{F}_S + \bar{F}_M + \bar{F}_{SR} + \bar{F}_T \end{pmatrix} \quad (A-12)$$

## PROGRAM II

The incremental changes in the orbital elements over one revolution that are required in the dicyclic method are presented here in closed forms. By expressing the sun's direction (assumed to be constant over one revolution) in terms of  $\theta_s$  and  $\phi_s$  (see Figure A-2), and holding the elements constant for the integration, the differential equations are found to be integrable in terms of complete elliptic integrals of the first and second kinds.

$$M = \begin{pmatrix} \cos \Omega & \sin \Omega & 0 \\ -\cos i \sin \Omega & \cos i \cos \Omega & \sin i \\ \sin i \sin \Omega & -\sin i \cos \Omega & \cos i \end{pmatrix}$$

$$\bar{r}'_{ES} = M \bar{r}_{ES}$$

$$\sin \phi_s = \frac{z'_{ES}}{r'_{ES}}$$

$$\cos \phi_s = \frac{\sqrt{x'^2_{ES} + y'^2_{ES}}}{r'_{ES}}$$

$$\sin \theta_s = \frac{y'_{ES}}{\sqrt{x'^2_{ES} + y'^2_{ES}}}$$

$$\cos \theta_s = \frac{x'_{ES}}{\sqrt{x'^2_{ES} + y'^2_{ES}}}$$

$$F_T = |\bar{F}_T| \quad (A-13)$$

$$\Delta t = a \sqrt{\frac{a}{\mu_E}} \left[ 2\pi + \frac{F_T a^2}{\mu_E} \cot i \cos \phi_s \cos \theta_s I_2(\phi_s) \right] \quad (A-14)$$

$$\Delta h = a^2 \sqrt{\frac{a}{\mu_E}} \left[ F_T \sin \phi_s I_1(\phi_s) - \frac{D}{M} \right] \quad (A-15)*$$

$$\Delta \Omega = \frac{F_T a^2 \cos \phi_s \cos \theta_s I_2(\phi_s)}{\mu_E \sin i} - \frac{3\pi J_2 \cos i}{a^2} \quad (A-16)$$

$$\Delta i = \frac{-F_T a^2}{\mu_E} \cos \phi_s \sin \theta_s I_2(\phi_s) \quad (A-17)$$

$$\Delta j = \Delta k = 0 \quad (A-18)$$

where

$$I_1(\phi_s) = 4 K(\theta) \quad (A-19)**$$

$$I_2(\phi_s) = \frac{4}{\cos^2 \phi_s} \left[ E(\theta) - \sin^2 \phi_s K(\theta) \right] \quad \phi_s \leq 88 \text{ degrees}$$

$$= \pi \left( 1 + \frac{1}{8} \cos^2 \phi_s \right) \quad \phi_s > 88 \text{ degrees}$$

$$\theta = 90 - |\phi_s| \quad (A-20)$$

$K(\theta)$  and  $E(\theta)$  are the complete elliptic integrals of the first and second kind respectively.

### PROGRAM III

Thrust is directed along the vehicle sun line (again assumed to be constant over one revolution). The differential equations are integrable when the independent variable is taken to be the eccentric anomaly. The integration limits are determined by the condition that thrusting occurs only when the angle between the velocity and thrust acceleration vectors is

---

\*Orbit eccentricity is assumed to be low throughout trajectory.

\*\*Singularity at  $\theta = 90$  degrees is of no concern since this corresponds to the sun's crossing the orbit plane.

less than a prescribed value, provided that the vehicle is in the unshadowed portion of its trajectory. The steps of this calculation will not be presented here. However, given the thrust angle  $\theta T$  and  $\phi T$  and the limits of integration  $E_1$  and  $E_2$  (see Figure A-3) the changes in the orbital elements are calculated as follows:

Let

$$f_{\Omega}(\phi, \theta, E) = \frac{F_T \sin \phi}{na\sqrt{1-e^2} \sin i} \left[ (1+e^2) \sin \omega \sin E - \frac{3}{2} eE \sin \omega \right. \\ \left. - \sqrt{1-e^2} \cos \omega \cos E + \frac{e\sqrt{1-e^2}}{2} \cos \omega \cos^2 E \right. \\ \left. - \frac{e}{2} \sin \omega \sin E \cos E \right] \quad (A-21)$$

$$f_{i_1}(\phi, \theta, E) = \frac{F_T \sin \phi}{n^2 a \sqrt{1-e^2}} \left[ (1+e^2) \cos \omega \sin E - \frac{3}{2} e E \cos \omega \right. \\ \left. + \sqrt{1-e^2} \sin \omega \cos E - \frac{e}{2} \cos \omega \sin E \cos E \right. \\ \left. + \frac{e\sqrt{1-e^2}}{2} \sin \omega \sin^2 E \right] \quad (A-22)$$

$$f_h(\phi, \theta, E) = \frac{a F_T \cos \phi}{n} \left[ (1+e^2) \sin \theta \sin E - \frac{3}{2} eE \sin \theta \right. \\ \left. + \sqrt{1-e^2} \cos \theta \cos E - \frac{e}{2} \sin \theta \sin E \cos E \right. \\ \left. + \frac{e\sqrt{1-e^2}}{2} \cos \theta \sin^2 E \right] \quad (A-23)$$

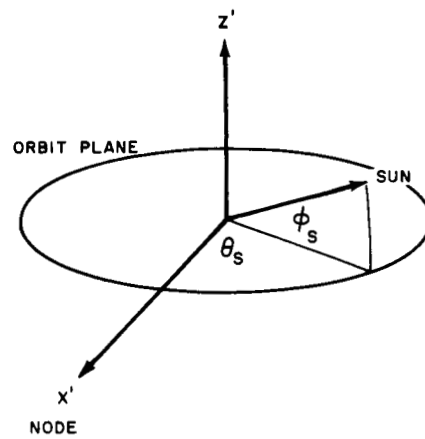


Figure A-2. Sun Direction Referred to Orbit Plane Coordinates

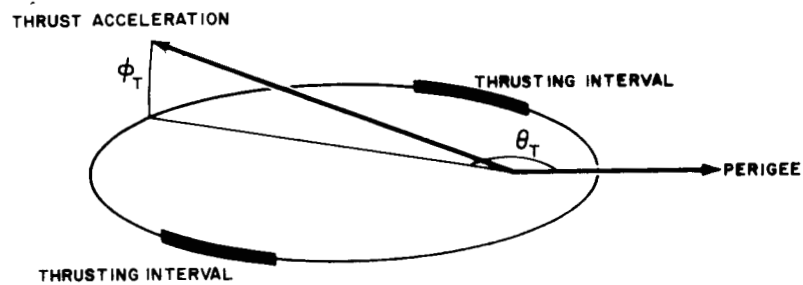


Figure A-3. Thrust Intervals for Equatorial Orbits

$$\begin{aligned}
f_{\omega}(\phi, \theta, E) = & \frac{F_T}{n} \left\{ \frac{\sqrt{1-e^2}}{nae} \cos \phi \left[ -\cos \theta \left( \frac{3}{2} E \right. \right. \right. \\
& - \left. \frac{\sin E \cos E}{2} - e \sin E \right) + \frac{\sin \theta}{\sqrt{1-e^2}} \left( \frac{\sin^2 E}{2} + e \cos E \right) \Big] \\
& - \frac{\cot i \sin \phi}{na\sqrt{1-e^2}} \left[ \sin \omega \left( (1+e^2) \sin E - e \left( \frac{3}{2} E + \frac{\sin E \cos E}{2} \right) \right) \right. \\
& \left. \left. + \sqrt{1-e^2} \cos \omega \left( -\cos E + \frac{e \cos^2 E}{2} \right) \right] \right\} \quad (A-24)
\end{aligned}$$

$$\begin{aligned}
f_e(\phi, \theta, E) = & \frac{F_T \sqrt{1-e^2} \cos \phi}{n^2 a} \left\{ \sin \theta \left[ \frac{3}{2} E - 2e \sin E \right. \right. \\
& \left. \left. + \frac{\sin E \cos E}{2} \right] + \frac{\sqrt{1-e^2}}{2} \cos \theta \cos^2 E \right\} \quad (A-25)
\end{aligned}$$

$$\begin{aligned}
f_t(\phi, \theta, E) = & \frac{-F_T \cos \phi}{n^3 ae} \left\{ -\cos \theta \left[ \left( \frac{3}{2} + \frac{5}{8} e^2 \right) E - 2e \sin E \right. \right. \\
& - \frac{(1-e^2)}{2} \sin E \cos E - \frac{2}{3} e \sin^3 E - \frac{e^2}{32} \sin 4E \Big] \\
& + \frac{\sin \theta}{\sqrt{1-e^2}} \left[ \left( \frac{1}{2} + e^2 \right) \sin^2 E + e \cos E \right. \\
& \left. \left. + \frac{e(2+e^2)}{3} \cos^3 E - \frac{e^2}{4} \cos^4 E \right] \right\} \quad (A-26)
\end{aligned}$$

Then, if

$$\bar{f}(\phi, \theta, E) = \begin{pmatrix} f_{\Omega}(\phi, \theta, E) \\ f_i(\phi, \theta, E) \\ f_h(\phi, \theta, E) \\ f_{\omega}(\phi, \theta, E) \\ f_e(\phi, \theta, E) \\ f_t(\phi, \theta, E) \end{pmatrix} \quad \text{and } \bar{p} = \begin{pmatrix} \Omega \\ i \\ h \\ \omega \\ e \\ t \end{pmatrix}$$

the incremental change due to thrusting is

$$\bar{\Delta p} = \bar{f}(\phi_T, \theta_T, E_2) - \bar{f}(\phi_T, \theta_T, E_1) \quad (\text{A-27})$$

To this must be added the usual corrections due to oblateness. Perigee is assumed to be sufficiently high so that drag can be neglected.